SISSA
Scuola
Internazionale
Superiore di
Studi Avanzati

Neuroscience Area
PhD course in Neurobiology

Optogenetic study of cell excitability over long timescales

Candidate:
Elena Gjorgievska

Advisor:
Michele Giugliano

Academic Year 2022/23

Declaration of Originality

I certify that this thesis, and the research to which it refers, are the product of my own work, and that any ideas or quotations from the work of other people, published or otherwise, are fully acknowledged in accordance with the standard referencing practices of the discipline.

May 9, 2023

Copyright Declaration

Acknowledgements

I express my gratitude and appreciation to my advisor, Prof. Michele Giugliano, for his guidance, support and patience in both my academic and daily pursuits. His expertise and knowledge have enabled me to excel in my research endeavours. I extend my sincere appreciation to my collaborators, Cesar Adolfo Sánchez Triviño and Giulia Franco, for their dedication and invaluable contributions to my work. My gratitude goes to Gerda Van de Vijver, Mike Wijnants from Antwerp University, and all staff members of SISSA for their exceptional technical support throughout my research. Furthermore, I express my sincerest thanks to the renowned SISSA community for their selfless assistance and generosity, which have made my time in Trieste unforgettable. My friends and colleagues have been a great source of strength and inspiration during my PhD. Lastly, I extend my gratitude to my family, and to my husband, for their understanding, encouragement, and unconditional love. Without them, my achievements would be impossible.

Abstract

The research carried out in this thesis builds on the pioneering discoveries by Larry Abbott, Shimon Marom, Eve Marder, and others, who's research provided key insights on the dynamics of neuronal excitability over long timescales. By combining Optogenetics with substrate-integrated microelectrode arrays, I developed a novel approach to observe and characterise single-neuron activity, in response to repetitive light stimulation and upon pharmacological isolation of neurons from synaptic interactions. This offers a detailed and systematic observation window of neuronal excitability over very long periods of time, which I inferred by probing the input-output properties of individual cells. A distinctive feature of our approach is the methodological advantage offered by Optogenetics, as we can restrict my investigation to genetically-identified cell types e.g., putative glutamatergic cells. My method also allows for stable recordings of a large number of simultaneous neurons, undergoing repeated wide-field photo-activation and retaining long experimental stability of the spike waveform at very low and comparatively high stimulation rates. I also develop an algorithm to resolve and separate individual neuronal units at each microelectrode. Through the analysis of my experimental results, I characterise rich dynamical processes underlying neuronal excitability, reflected in power-law relations across various stimulation frequencies and various degrees of cross-correlations along multiple timescales. As an important consequence, besides further clarifying the physiological processes of biological excitability, my results also provide the community with insights and quantitative experimental data, very much needed for designing novel mathematical models of cells and circuits, capable to capture neuronal dynamics to a full extent and paving the way for more realistic *in silico exploration of the adaptive responses of the nervous system.*

Contents

List of Figures

List of Tables

List of Abbreviations

AAV Adeno-Associated Virus

AIS Axon Initial Segment

AMPA Alpha-Amino-3-Hydroxy-5-Methyl-4-Isoxazolepropionic Acid

aoLED LED Electronic Driver

BNC Bayonet Neill-Concelman

CaMKII Calmodulin-dependent protein kinase II

ChR1 Channelrhodopsin-1

ChR2 Channelrhodopsin-2

CMV Human cytomegalovirus

CV Coefficient of Variation

div Day in Vitro

fBm Fractional Brownian Motion

GABA Gamma-Aminobutyric Acid

HEK293T Hella Kidney Epithelial-Like Cells

HOC High Order Calculator

IFB Interface Board

ISI Inter-Spike Intervals

KA2 Kainate receptor subunit

LED Light-Emitting Diode

LVC Leuven Vector Core Company

MEA Microelectrode Arrays

NCCP Non-trivial Cross-correlation Persistence

NMDA N-Methyl-D-Aspartate

NMODL NEURON MODeling Language

PEI Polyethyleneimine

SB Synaptic Blockers

SCU Signal Collector Unit of the MEA120 System

SDE Stochastic Differential Equations

ShChR Stigeoclonium Helveticum Channelrhodopsin - Chronos

SPC Superparamagnetic Clustering

TTL Transistor-Transistor Logic

1. Introduction

1.1. Overview

This interdisciplinary exploration of neuronal excitability over long timescales unfolds along my own personal academic journey. In my PhD project, I experimentally probed and analysed the dynamics of excitability at the single-cell level in putative glutamatergic cortical neurons. Throughout this work, I have closely realised the importance of taking great care of an experimental design, with respect to its timescales as well as in terms of of the nature of the external stimuli used. I am convinced that by widening our current perspectives on the cell's intrinsic adaptation mechanisms and memory processes, we can bolster the creation of more accurate analytical computational models in Neurobiology.

To illustrate the motivation of my research, in Sec. 1.2 I review different definitions of excitability and their impact on experimental and modelling approaches. I then extend this preamble to a series of research questions addressed in Chp. 2, where I examine the current literature and present relevant experimental and theoretical arguments. My first step is to review established capabilities of a single neuron based on both *in vivo* and *in vitro* studies, as well as explore how neuron models have evolved to keep up with these tasks. Then, I explore the intricate timescales related to intrinsic cellular phenomena, ranging from gene expression to morphological changes, and how these

mechanisms relate to changes in excitability at the organisation level of the neuronal membrane. Beyond this level, I also examine state-of-the-art stimulation paradigms, which are important to probe and characterise the dynamical properties of excitability. In terms of methodology, I adopt an established characterisation and quantification of neuronal excitability, over extended timescale, as first proposed by Gal and coworkers (Gal et al., 2010).

My PhD project is then divided into separate goals, each corresponding to a specific work package presented in Chp. 3. These include the use of microelectrode arrays (MEA) as substrates for growing rat cortical neurons *ex vivo* in combination with optogenetic tools (Sec. 3.2.1) to selectively target the expression of a fast-kinetic channelrhodopsin (ChR) in the cell membrane (Sec. 3.1). These led to an extended campaign of experiments involving extracellular electrophysiology (Sec. 3.3) as well as to a short series of supporting intracellular recordings (Sec. 3.4.2), and finally to the side exploration of computational models of neuronal excitability (Sec. 4.3) to replicate to some extent the experimental findings. Chp. 4 presents the implementation of the methodology (Sec. 4.1) and describes the findings related to long experiments on genetically-identified cortical neuronal type (Sec. 4.2). Results also include the numerical simulations of established as well as improved mathematical models of neuronal excitability (Sec. 4.3), and finally a direct characterisation of channelrhodopsins kinetics (Sec. 4.3), besides the central part of my work that revealed and confirmed a very rich dynamical behaviours of neuronal excitability over extended timescales (Sec. 4.2). After a brief discussion of the outcomes, I summarise my observations and propose potential future research directions in Chp. 5.

I am overall convinced that a multifaceted and interdisciplinary approach - in both the definition of the research questions and methods - offers the greatest prospects for significant impact, and I am excited to be able to share my contributions to the field along this direction and philosophy.

1.2. Motivations

Defining the question is part of the answer.

Excitability is a fundamental property of neurons and it is essential for information processing in the nervous system, together with learning[1] and memory[2]. Excitability can be defined in several ways, depending on the experimental paradigm of choice and, importantly, the related timescales of observations.

One commonly used definition revolves around the cell's ability to produce an action potential in response to an external stimulus. At the dawn of the twentieth century, as the neuron gained recognition for being a distinct unit within the neuronal system, significant discoveries were made regarding action potentials. Early studies on isolated sensory axons by (Adrian and Zotterman, 1926) showed that excitability changes both over short and relatively long periods of time. Regarding the former case, it was observed that each action potential leads to a brief *refractory* phase, where neuron can hardly be excited again. This state is then followed by gradual recovery of excitability, through spike frequency *adaptation*. In 1952, Hodgkin and Huxley (Hodgkin and Huxley, 1952) were the first to confirm these observations and precisely dissect their underlying subcellular mechanisms, at the level of transmembrane conductances of voltage-dependent ion channels. In addition, they provided a mathematical model capable of accurately describing the dynamics of membrane excitability and the generation and propagation of action potentials. On the observational timescales chosen by Hodgkin and Huxley, successive discharges can be accounted for by the recent changes of the membrane voltage. Changes in excitability can, therefore, be described by a process on a timescale of two to three orders of magnitude longer than the action potential itself. In other words,

[1] Learning refers to a process of alterations in the state of a system over time.
[2] In its simplest form, memory refers to a process of information retention in a system over time, which can be accessed, and erased from the past states of the system.

the neuronal membrane learns locally and the neuron retains a short memory relayed on a specific timescale. The model proposed by Hodgkin and Huxley thus marked a significant advancement in Neuroscience, and subsequently became the most used and most useful framework for describing cellular electrophysiology. This success can be primarily attributed to the model's ability to provide a comprehensive representation of a complex mechanism using only a limited number of measurable biophysical parameters. In this context, any effects exceeding a few hundred milliseconds, such as those that occur during long-term memory formation, must be explained by the persistent modifications e.g., at the level of synaptic interactions between neurons, where excitability can be assessed on a larger context of time and space. After all, the brain is a multifaceted system comprising units that operate across several levels of organisation, from simple microcircuits (Abeles, 1991) to large-scale brain structures (Buzsáki, 2010).

Consequently, over the past six decades, *top-down paradigms* have evolved towards simultaneously recording single-unit activity (Buzsáki, 2004) from an exponentially growing number of neurons (Stevenson and Kording, 2011) with the aim to infer their connectivity and capture their interactions. Extracellular techniques such as tetrodes, substrate-integrated microelectrodes arrays (MEA), and CMOS-based probes (e.g. Neuropixels) combined with various spike sorting methods (see Harris et al., 2000; Wang et al., 2019) have allowed for the isolation of 20–200 neurons per brain structure and a maximal count of more than 700 neurons (Atlas, 2021). The experimental paradigms gradually broadened at the level of the neuronal populations, regarded as the primary information processing unit capable of executing the intricate "neuronal code" [3].

Indeed, when examined at the level of the activity emerging from interconnected neurons, *dynamical* properties of populations display a repertoire of behaviours that go

[3] For a distributed dynamical systems like the brain, "coding" may be an inadequate analogy (Brette, 2019/ed).

beyond those observed in individual neurons. Extensive research has corroborated the existence of short and long-term plasticity in groups of neurons that co-activate. Short-term synaptic plasticity changes are often due to the presynaptic neuron's recent history of firing, and as such, are reflective of the memory capacity already described as characteristic of a single neuron; in contrast, long-term synaptic plasticity involves more permanent changes in synaptic strength that occur over extended periods of time, ranging from minutes to hours or even days: a biophysical process that appears adequate to account for high-level learning and memory processes in the brain. Furthermore, the interactions between short-term and long-term synaptic plasticities might play a role in shaping the pairwise connectivity motifs observed in experiments and models. Specifically, short-term plasticity could modulate the timing and frequency of pre- and post-synaptic activity, while long-term plasticity could induce more permanent changes in the strength of synaptic connections. These processes could work together to create connectivity patterns that are optimised for specific neuronal computations (Vasilaki and Giugliano, 2014).

Populations of neurons can perform dense-coding through the propagation of unique activity patterns initiated by different neurons, as evidenced by studies on neuronal populations (Alejandre-García et al., 2022; Carrillo-Reid et al., 2016). Additionally, another theory suggests that synchronously firing neurons are not necessarily synaptically connected. For instance, interneurons with broad axon arbours that signal to multiple cells may not be linked together, resulting in sparse pyramidal neuron groups encoding memories (sparse-coding) (Beyeler et al., 2019; Dahmen et al., 2022; Gastaldi et al., 2021; Krupic, 2017; Yap et al., 2021). The discovery of "concept cells" (Quiroga, 2012) presented an intermediate scenario, where the latter singularly encode local concepts and concurrently participate in sparse-coding for encoding associations between concepts (Dahmen et al., 2022; Gastaldi et al., 2021).

All proposed and assessed hypotheses possess both weaknesses as well as unique strengths that have been proven beneficial. Nonetheless, single-neuron alterations and adaptation over extended timescale has been mainly overlooked. Related studies typically devise experimental protocols to unearth correlations among spike activity from distinct cells. These trials prioritise replication and consist of trials of relatively short duration, spanning many hundreds of repetitions. While months-long recordings from the same neurons in awake behaving mice (Fu et al., 2016) and over the animal's entire adult life (Zhao et al., 2023) reveal slow changes in excitability, captured at the single-cell level.

To sum up, we can state that behaviours resulting from high-level neuronal dynamics in proposed experimental paradigms differ from those exhibited by single neurons (Krakauer et al., 2017). Population-level activity gives rise to emergent dynamical features over extended time periods. But in order for this to hold, is the fact that a neuron operates solely within a particular timescale a necessary prerequisite?

All models are wrong, some models are useful.

A model aims, in principle, to simplify and explain. In 1954, a neuron was first abstracted in a (artificial) binary unit, with interesting properties when operating in concert with other units, as a simple feed-forward network (McCulloch and Pitts, 1943). Today the complexity of a neuron can be better approximated by a deep neural network with 5–8 layers, the depth arising from the interaction between NMDA receptors, and dendrite branches, conceptualised as a set of spatiotemporal pattern detectors (Beniaguev et al., 2021). Before the establishment of the Hodgkin-Huxley model, spiking neuron models were pragmatic integrate-and-fire descriptions, such that the membrane voltage is a function of the input current, and predicts the spike times without any variables of biophysical processes that shape the time course of a spike. Models have been

developed to also combine features of standard leaky integrate-and-fire models with a second variable reflecting adaptation, refractory period, or a dynamic threshold (Badel et al., 2008; Teka et al., 2014). The Hodgkin-Huxley biophysical model evolved to include other kinetic equations accounting for different ion channels, which inevitably led to the same tendency for detailed modelling compared to the *top-down* approach, and the development of *in silico* neurons. The latter is based on a full reconstruction of the different morpho-electrophysiological cell types (noa), their expression profiles, as well as Connectomics (part of neocortex simulation in Markram et al., 2015; model of the hippocampus in Romani et al., 2022).

The Hodgkin-Huxley model can also be reduced to lower dimensional models (Gerstner, 2002), which are obtained applying approximation techniques aimed at grouping together the ionic variables of gating which have the same characteristic times or by considering quasi-stationary variables that reach a constant value very quickly (Soudry and Meir, 2012; Wang and Buzsáki, 1996). In the framework of conductance-based neuron models, ion channels are modelled by their voltage-dependent conductances, and the excitable membrane is represented by a capacitor. This approach provides robust means of investigating the complex interplay of ions and voltage dynamics within neurons.

Both in experiments and theory, two paradigms exists: top-down and bottom-up. The *top-down paradigm* treats complexity as an enigmatic "black box" and concentrates on input-output dynamics to draw statistical conclusions about its underlying processes. Meanwhile, the *bottom-up paradigm* aims to deconstruct complexity into comprehensible, manageable elements through simplification and abstraction.

Recent developments in both paradigms usually result in more elaborate ans less interpretable descriptions (Bzdok et al., 2019). The inclusion of a larger set of neurons in recordings (top-down approach) and incorporating extensive biophysical intricacies

(bottom-up approach) results in an increased model complexity. Most of contemporary modelling efforts are computationally intensive, and driven by the expectation that a larger number of degrees of freedom will increase the accuracy in predicting neuronal activity. Overall, besides being demanding, in terms of "big data" availability, analysis, and modelling, both approaches are importantly at risk of missing or neglecting the role of the single neuron.

To conclude, if we are to understand how learning and memory emerge from a collection of neurons, both artificial and biologically-accurate neuronal models need to first accurately describe intrinsic input-output dynamical properties over extended timescales.

2. Background

This chapter delves into research that emphasises the potential of a single neuron for learning, memory, and computational capabilities.

2.1. Inside-out perspective: the intrinsic excitability

The origin of intrinsic excitability lies in cellular processes below the membrane level, such as the behaviour of ion channels, the changes in ion conductances, the proteins turnover, and gene expression. We examine instances that exemplify each of these mechanisms.

2.1.1. Learning and memory in single neurons

Intrinsic plasticity

In the preceding section, we explored research that substantiates the concept of synaptic plasticity. However, the formation of primary memory is likely to involve the interplay of intrinsic neuron excitability plasticity and synaptic plasticity (Papoutsi et al., 2011). When there is an increase in excitation at the cellular level, neurons can trigger synaptic

changes that are homeostatic in nature, as demonstrated in the study by Goold and Nicoll (2010). Specifically, to maintain the stability of a neuronal ensemble, cell-autonomous intrinsic mechanisms that affect long-term dynamics of excitability are hypothesised to be involved (Daoudal and Debanne, 2003; Debanne and Poo, 2010; Gallistel and Balsam, 2014). One mechanism underlying the increased excitability during ensemble formation is a combined increase in membrane resistance and reduction of firing threshold (Alejandre-García et al., 2022). To stabilise neuronal activity, homeostatic excitability plasticity, which is a slow process, can complement Hebbian synaptic plasticity as a compensatory mechanism (Gasselin et al., 2017). The neuron's long memory capacity is upheld by intricate learning that takes place through non-synaptic means, which showcases input and cell specificity and operates on various timescales. As recurrent interactions take place, the slower timescales become more effective (Zeraati et al., 2021).

Neurons can potentially perform different types of computations, depending on the levels of background noise and the expression of ionic channels. The operation they perform can vary from leaky integration (without strong negative feedback) to differentiation (e.g. firing rate adaptation), or fractional differentiation in the presence of multiple timescales of adaptation (Lundstrom et al., 2008).

Ionic currents and ion channels

Ori et al. demonstrate that macroscopic cellular invariant, given microscopic variation and robustness of excitability, benefits from the variability of history-dependent timescales that ion channels display. Specific ionic currents in well-defined neuronal systems undergo transformations lasting days after associative learning with physiological stimuli. During acquisition the intracellular calcium increases; the increase in calcium is accompanied by specific potassium current reduction that lasts for days after conditioning. Calcium is known to mediate many activity-dependent processes,

including the magnitude of ionic currents (Alkon, 1984). Additionally, the increase of calcium enhances Calmodulin-dependent phosphorylation of proteins that either regulate or are part of ion channels.

Prolonged spiking activity in a neuron results in modifications of the intracellular and extracellular concentrations of Na^+ and K^+, respectively, and triggers homeostatic mechanisms that regulate ionic gradients at timescales much slower than action potential genesis (Contreras et al., 2021). These non-stationarities bear consequences for neuronal computation.

Protein turnover and gene expression

Learning induced long-term modulation of intrinsic excitability in pyramidal neurons is protein synthesis dependent, and is capable of bi-directional altering of temporal processing (Chandra and Barkai, 2018; Debanne et al., 2019). Mechanisms at the level of genes and transcription factors are activated within minutes after a neuron receives a particular stimulus. Neurotransmitters may rapidly activate specific gene transcription in differentiated neuronal cells (Greenberg et al., 1986) inducing a bidirectional perisomatic[1] inhibitory plasticity in a sparse network of *Fos*-activated neurons (Yap et al., 2021).

The role of intrinsic neuronal excitability during disease is still young when compared with the work focused on synaptic mechanisms, but it can be useful to uncover the fundamental mechanisms of excitability. For example, dramatic up-regulation of intrinsic bursting in CA1 pyramidal cells toward a phasic phenotype, particularly the appearance of Ca^{2+}-dependent bursting have been reported in models of chronic epilepsy (Sanabria et al., 2001). Several lines of evidence indicate that high-threshold bursting is driven by

[1] The perisomatic region is defined as the domain of the plasma membrane which includes the proximal dendrites, the cell body and the axon initial segment (AIS; Freund & Buzsaki, 1996).

persistent Na^+ current at or near the soma (Chen et al., 2011). This may be connected to up-regulation in expression of ion channels and various receptors. A healthy neuron, in turn, moves smoothly between low and high firing rates in broad range. These are mediated by specific ionic currents, e.g., A-type potassium currents, as well as by the interactions between multiple currents, implying a need for ion channel degeneracy in the tuning of neuronal properties (Drion et al., 2015).

2.1.2. Morphology of the excitable membrane

Morphological polarisation of the neuron can have a significant effect on intrinsic excitability dynamics. The changes in homeostatic mechanisms that regulate ionic gradients at slow timescales are bidirectional, affecting the signal propagation in the axon, the dendrites, and the soma, and appear to be cell specific (Hansel and Disterhoft, 2020; Lisman et al., 2018; Titley et al., 2017).

At the beginning of the previous section, I introduced a definition of excitability in regards to membrane organisation and the duration of a single spike. Hodgkin and Huxley have measured the dynamics of short-span excitability using the K^+ and Na^+ channel conductances in the squid giant axon[2] in space-clamp. However, a neuron has diverse functional compartments and as a result, there are notable differences between the spike waveform in the *axon* and *dendrite* membranes compared to that in the *soma* of the same neuron. In voltage clamp, the soma membrane voltage is the same at different places and undergoes simultaneous change upon spike generation, but there may be current flow between the soma, dendrites and axon that alters the shape of the spike to some extent. For most pyramidal neurons in the mammalian brain, the spike initiated in the axon initial segment (AIS) is far enough (30–50 μm) from the soma, so the spike

[2] The squid ganglion is composed of the three largest neurons on the planet.

waveform recorded in the soma can show clear effects arising from non-uniformity of voltage. For example, the way a spike is shaped is substantially affected at presynaptic terminals, where shape is important for the timing of presynaptic calcium entry, leading to dramatic changes in postsynaptic currents. According to the *resistive coupling theory*, an interplay between the axon initial segment and the electrotonic perisomatic load determines the spike waveform. This phenomenon not only alters the shape of spikes recorded at the soma, but also determines the dynamics of excitability across a variety of timescales shown in different classes of multi-compartmental mathematical models of rodent and human cortical tissue (Verbist et al., 2020). The AIS is clustering high densities of voltage-gated sodium (Nav) channels and defines the location from where all action potentials are initiated and propagate bidirectionally, towards the presynaptic terminals, then back into the soma and dendrites. It is noteworthy that ion channel density is a determinant factor in the transition from regular to fast spiking in the soma, but not in axons (Zeberg et al., 2010). Conversely, unlike axons, the soma have the ability to fire across a broader range of frequencies and display considerable changes in firing frequency in response to slight variations in input currents.

The large number of *dendritic branches* in cortical pyramidal neurons contain voltage-dependent ion channels, the activation of which produce local membrane potential nonlinearities[3] (Na^+, Ca^{2+} or NMDA spikes). These markedly shape both incoming synaptic input and action potential output. Independently of circuit connectivity and synaptic machinery, a variety of activity-dependent changes which affect the intrinsic firing properties of the neuron, can also promote computationally relevant structural rearrangements of its axon and dendrite trees (Remme and Wadman, 2012).

[3] The change of the output is not proportional to the change of the input in a system.

2.1.3. Phenotypes of excitability

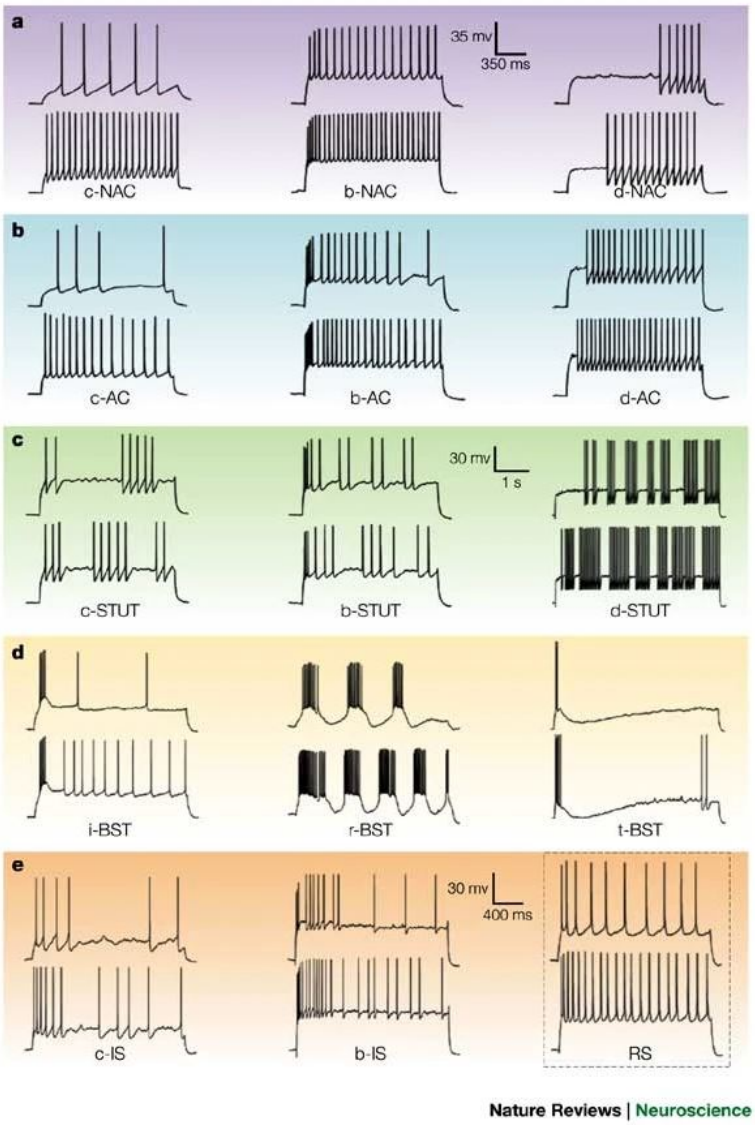

Figure 2.1. "Classes" of neuronal electrical responses. The figure shows prototypical steady-state responses to a sustained (step) current injection in the soma: non-accommodating (NAC); accommodating (AC); stuttering (STUT); bursting (BST); and irregular spiking (IS). Most classes contain three subclasses: delay (d); classic (c) and burst (b). For bursting interneurons, the three types are repetitive (r), initial (i) and transient (t). RS (regular spiking) is an example of a classic discharge of a pyramidal cell. *Reproduced with permission from Springer Nature* (Markram et al., 2004)

Cells that are easily stimulated possess the capability to generate and spread spikes, which are distributed in a wide range of electrical phenotypes (e-types) that can either be discreet or appear as continuous, as summarised by Huang and Paul. In fact, novel morpho-functional and electrophysiological cell types are frequently being introduced (Hunt et al., 2018).

Considering short-term excitability, the complexity of firing behaviour depends on the expression of more types of voltage-dependent ion channels and the role of specific types of ion channels in generating these differences in excitability. A staggering number of ion channel types and distinct voltage-dependent conductances have been discovered to shape excitability in the cell bodies among various types of neurons in the mammalian brain (review in Bean, 2007).

Neurons can be classified based on both the onset and the steady-state response to a step current injection into the soma (Markram et al., 2004). In neuron spiking behaviour, there are five most fundamental classes of neurons in response to current input that affect firing, shown in Fig. 2.1. There classes include regular spiking, fast spiking, intrinsic bursting, chattering, and low-threshold spiking. Regular spiking neurons are usually excitatory and have pyramidal cell morphology. They respond to depolarisation with a burst sequence with adaptation. Regular spiking cells have transient potassium currents that slow down the onset of the first spike and increase refractory periods resulting in frequency adaptation. Only some of the various voltage-dependent potassium currents present in a neuron are activated during regular spiking. Fast-spiking neurons are associated with the Kv3 family of voltage-gated potassium channels, which have fast kinetics that are appropriate for narrow spikes and short refractory periods.

Different combinations of conductance densities can regulate electrical activity on various time scales in homeostatic self-tuning models, even if similar activity patterns are

present in the context of slow modulations on intrinsic excitability. It is intriguing that there is no specific set of conductance parameters that elicits a particular behaviour; instead, there is significant flexibility in the expression of diverse conductances to maintain a cell-intrinsic readout of activity among different neuron types. The onset response patterns of electrically stimulated single cells illustrated in Fig 2.2 resemble the different types of steady-state responses to stimuli identified as "classes" in Fig 2.1 (Markram et al., 2004).

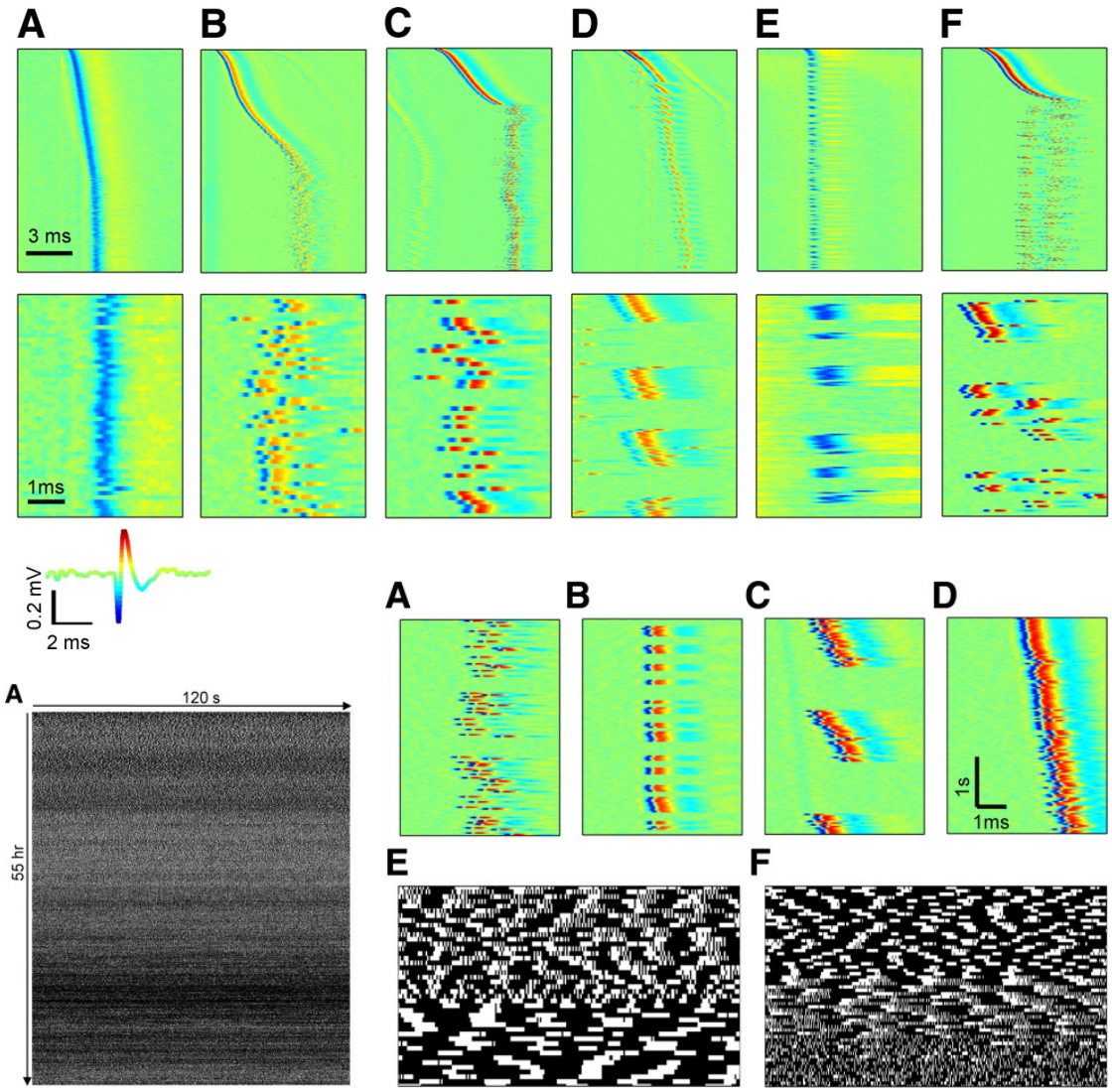

Figure 2.2. Long-term response "classes" and pattern modes from Gal et al. (2010). The top part of the composite figure shows panels A-F from Fig.8. Long-term response "classes" *i.e.*, prototypical onset response patterns of different neurons to stimulation rate of 20 Hz; the first row panels show the entire response, bottom row panels show an enlargement of a segment within the intermittent phase. The bottom part of the composite figure shows panels A-D from Fig.10. Quasi-stable pattern modes in the intermittent phase in one given neuron recorded over 55 h under 25 Hz stimulation; transition between modes in panels E-F. *Adapted from* Fig.8 *and* Fig.10 *of* Gal et al. (2010); *reprinted under the Creative Commons licence.*

2.1.4. Background noise and temporal variability

Subthreshold voltage oscillations as a whole mainly arise from the membrane excitability of single neurons. Information in neurons is encoded through action potential patterns, which are influenced by both large ionic currents and smaller threshold currents. These currents affect the timing, pattern, and frequency of spikes, all of which are crucial for understanding how neurons encode information.

At the single neuron level, temporal *variability* is observed in evoked activity over long timescales (Faisal et al., 2008; Reinartz, 2019; Yarom and Hounsgaard, 2011, review), leading to wide temporal range dynamics that have functional and theoretical implications. This cell-to-cell variability and cell-intrinsic variability is potentially connected to a relationship between the number of events measured on short and longer timescales, indicating a dependencies on past values. In general, by comparing different realisations of a process functioning as an input as well as a cell response output, we can better understand the underlying dynamics, make predictions, and estimate parameters. For example, fluctuating input currents can determine the statistics of a neuron's output spike train, while cell membrane *resonance* can cause different spiking patterns.

The phenomenon of resonance is commonly observed in neurons and is known as subthreshold membrane potential oscillations. When a neuron is at rest, its membrane potential is maintained at a relatively stable value. However, when a depolarising current is injected into the neuron, the membrane potential begins to oscillate at a certain frequency. This oscillation is caused by the interplay between the cell membrane capacitance and the potassium current inductance. The electrical properties of a neuron, including its cell membranes, intracellular plasma, and channel proteins, can be compared to those of electronic circuit components. In an "electrical circuit", the cell membrane capacitance represents the ability of the membrane to store electrical charge,

while the potassium current inductance represents the tendency of the potassium ions to resist changes in their flow. When a depolarising current is injected, the membrane potential rises, causing the potassium channels to open and allowing the ions to flow out of the cell. This leads to a decrease in the membrane potential, causing the potassium channels to close and allowing the membrane potential to rise again. This process repeats, leading to the generation of subthreshold membrane potential oscillations (Ge and Liu, 2016, review). Regular spiking and intrinsic bursting neurons typically exhibit *resonance* at resting potentials, while fast spiking neurons do not. Additionally, subthreshold oscillations, or *inductance*, contribute to both the circuit and single-cell properties that affect network rhythms. These low-frequency electrical activities are primarily caused by intrinsic subthreshold voltage oscillations, which are unique to neurons. Despite varied stimuli, cortical neurons exhibit consistently similar frequency selectivity, which is based on intrinsic neuronal principles.

In conclusion, all of the above described processes which are intrinsic to the single cell practically cover any observable physiology timescale.

2.2. Outside-in perspective: the stimulus

Cell excitability can change over time, both in response to individual stimuli and through long-term changes in the intrinsic properties of the neuron itself.

With this section we highlight the importance of understanding the temporal and spatial input[4] patterns to neurons in order to understand the long-term change of the neuron's intrinsic properties. Hodgkin and Huxley described how action potentials are gener-

[4] Adrian and Zotterman hinted at the significance of stimulus design for excitability: persistent stimulus is accompanied by a slow decline in its exciting value.

ated in response to axial current injection, but physiological input currents are often unpredictable and noisy. Temporal variability is inherent to the cell over long timescales (review by Reinartz, 2019), and it is observed in practically all of evoked activity (Faisal et al., 2008; Yarom and Hounsgaard, 2011). Mainen and Sejnowski demonstrated that neurons respond to specific temporal input features rather than solely to current amplitude, resulting in high response reliability to the repeated injection of the same noisy input and significantly variable responses to identical direct current injections across trials. Besides net membrane currents, modulation of the total membrane conductance is stimulus-dependent, which is not reproduced by standard current-clamp protocols.

Understanding how neurons transform inputs is crucial for comprehending both their input and output. Quantitative differences are expected to occur in neuronal responses when comparing different stimulation paradigms, effectively determining the neuron's input-output (I/O) dynamical transfer properties. Differences in ionic conductances which produce differences in firing patterns will in principal also produce differences in spike shape. These are more evident on a short timescale, hence, experimental paradigms are gradually changing to alter current mathematical models of action potential initiation, particularly for human cortical neurons, as observed over a single action potential timescale.

By using statistical analysis of the properties of synaptic background activity, such as the temporal correlations and fluctuations in conductance, it is possible to generate synthetic input that closely resembles the natural input to cortical neurons. This can be done by creating models based on the statistical properties of real neural networks, and using these models to generate synthetic input that can be injected into the cells during experiments. One example of this is the use of the maximum entropy principle to generate synthetic conductance waveforms that reproduce the statistical properties of synaptic background activity observed *in vivo* (Destexhe et al., 2001). This approach

allows for the creation of input that closely mimics the natural input to cortical neurons, improving the physiological relevance of the experiments. Furthermore, statistical physics can be used to analyse the response of neurons to different types of input, providing insights into the mechanisms underlying cortical information processing. For example, by studying the response of neurons to different input statistics, it is possible to identify the features of synaptic input that are important for information processing in cortical networks (Destexhe et al., 2003).

Over longer timescales, changes in external inputs can adjust the neurons' intrinsic properties. In particular, the study by Reinartz et al. suggests that slow changes in excitability may be influenced by the specific patterns of synaptic activity experienced by neurons. Consistent activation of a neuron's synapses in a specific sequence can change the properties of its ion channels and receptors, causing long-lasting alterations in excitability. Hence, neuronal firing sequences triggered by synapses play a role in the gradual changes in excitability over time.

2.2.1. Optogenetics and ChannelRhodopsin ShChR

While Optogenetics had been already proposed in *in vitro* MEA studies before (Lignani et al., 2013; Pulizzi et al., 2016), its full potential as a minimally invasive probing-approach has not yet been fully exploited when studying long adaptive cell responses in the presence of external stimuli.

In 2005, it was reported that introducing a single-component microbial opsin gene into mammalian neurons resulted in precise control of action potentials. This discovery was soon followed by additional studies that confirmed the feasibility of using microbial opsins as optogenetic control tools. Additionally, it was found that mature mammalian

brains and all vertebrate tissues examined contained sufficient amounts of all-trans retinal, making it possible to define a single-component strategy. By 2010, the primary types of ion-conducting microbial opsins, including bacteriorhodopsin, channelrhodopsin, and halorhodopsin, were all demonstrated to function as optogenetic control tools in mammalian neurons (**?**).

Channelrhodopsins are a subfamily of Rhodopsins that are light-gated ion channels. They serve as photo-receptors in unicellular green algae, controlling movement in response to light. Expressed in cells of other organisms, they enable light to control electrical excitability, intracellular acidity, calcium influx, and other cellular processes. Variants that are sensitive to different colours of light or selective for specific ions have been engineered. Closely related to the archaeal sensory Rhodopsins, the light-gated proton channel ChannelRhodopsin-1 ChR1 and light-gated cation channel ChannelRhodopsin-2 ChR2 from the green alga *Chlamydomonas reinhardtii* are the first discovered ChannelRhodopsins (Nagel et al., 2003). The essential features of these microbial optogenetic tools stem from the behaviour of their native host organisms, which rely on seven-transmembrane proteins encoded by type I opsin genes to sense and react to their surroundings. When bound to retinal, these opsin gene products are known as rhodopsins. However, in experiments where they are expressed in a different system, the precise form of the retinoid-bound state is typically unknown. For the purposes of neuroscience research, these tools are simply referred to as opsins (a more convenient and accurate shorthand term since "opsin" applies to both the genes and the protein products). Unlike mammalian type II opsins, microbial opsins are single-component systems that carry out both light sensing and ion conductance functions with the same protein (**?**). When exposed to blue light, the protein undergoes structural changes that allow positively-charged ions such as protons or sodium ions to flow across the cell membrane. This results in a depolarisation of the membrane, which can trigger action potentials in ex-

citable cells. The *S. helveticum* ChannelRhodopsin (ShChR) has very fast kinetics, with a turn-on time of 2.3 ± 0.3 ms and a turn-off time of 3.6 ± 0.2 ms. These are fast on, off, and recovery kinetics for precise and accurate control of the spike timing (Klapoetke et al., 2014).

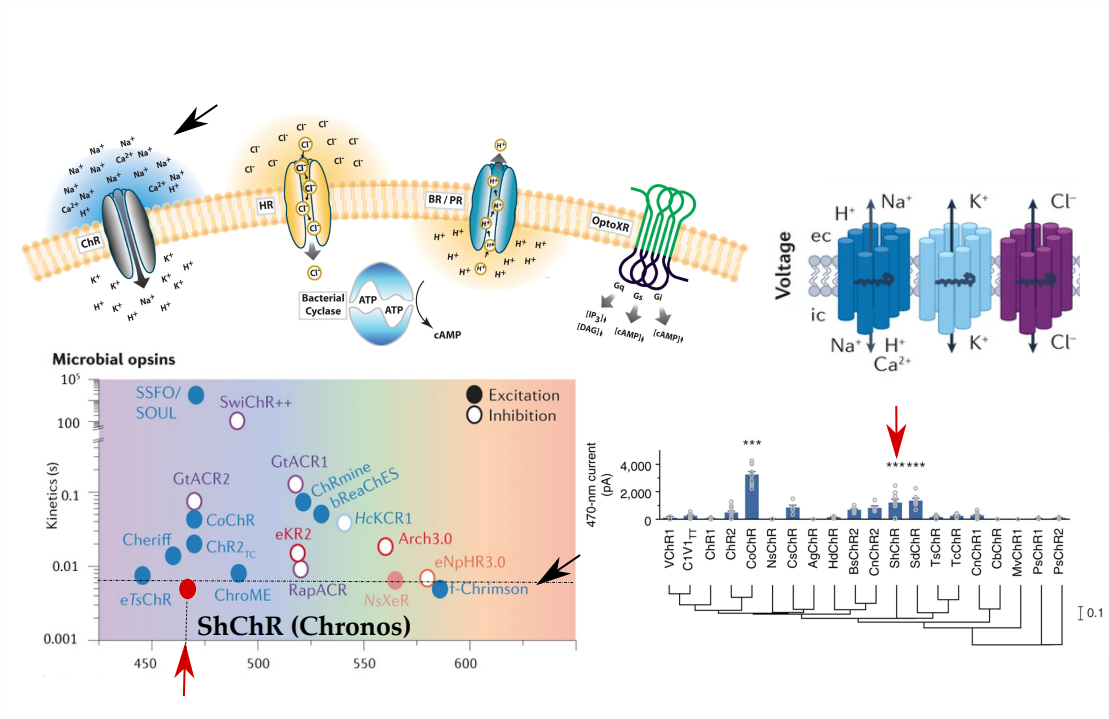

Figure 2.3. Tools for optogenetic manipulation of membrane voltage and local ion concentrations. The top panel (left) shows single-component optogenetic tool families; transported ions and signalling pathways are indicated; the top panel (right) shows channelrhodopsins for optogenetic manipulation of membrane voltage - *adapted from* Fig.1 *of* **?**. Bottom panel (left) shows commonly used optogenetic tools for excitation or inhibition of neuronal activity include cation-conducting ChRs eTsChR254, Cheriff203, CoChR30, CrChR2TC, ChroME77 and derivatives, SSFO/Soul120, ChRmine, bReaChES and f-Chrimson (black arrow), chloride and potassium-conducting ChRs (for example, GtACR1, GtACR2 and HcKCR1, inward directed proton pumps (for example, NsXeR and outward-directed proton, sodium and chloride pumps (for example, Arch3.0, eKR2, eNpHR3.0), all plotted according to their peak excitation wavelength and temporal kinetics - *adapted from* Fig.2 *of* Emiliani et al. (2022); Bottom panel (right) shows maximal current values of some channelrhodopsins - *adapted from* Fig.1 *of* (Klapoetke et al., 2014). Red arrows are noting ShChR (Chronos) kinetics and maximal currents. All figures are adapted with modifications *under the Creative Commons licence.*

2.3. Related Work

This section provides a summary of previous sections through pertinent studies that explored and examined the relevant facets concerning long-term intrinsic excitability in single neurons.

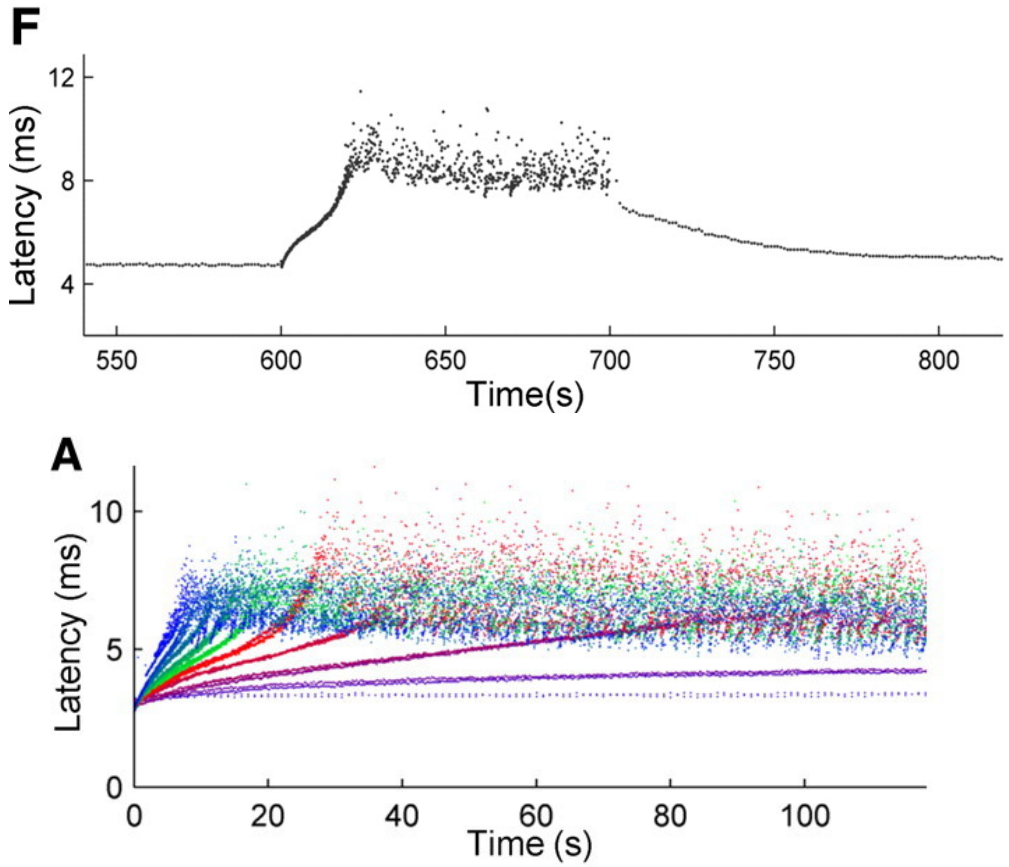

Figure 2.4. Neuronal response to ongoing stimulation is characterised by distinct phases. The top panel (F) shows the latency of a single neuron after repeated stimulation over time of two interchanging stimulation frequencies: 1 and 20 Hz. The bottom panel (A) shows duplicates of the latency for different stimulation frequencies over a different time window: 1 - 50 Hz. *Adapted from* Fig.1 *and* Fig.2 *of* Gal et al. (2010) *under the Creative Commons licence.*

In 1994, Marom and Abbott propose that neurons have a significant memory capacity, possibly related to their *intrinsic excitability machinery*. The study focuses on the idea that a neuron's ability to change its electrical properties and generate action potentials can influence its long-term memory retention capabilities. The intrinsic excitability machinery could be related to the neuron's ability to generate complex patterns of activity, store and retrieve memories, and engage in learning and adaptation. They provide a theoretical framework for understanding the fundamental properties of neurons and their role in general. However, it is unclear how neurons actively use this capability.

Marder et al. in 1996 and Desai et al. 1999 found neuron's behaviour and function are not fixed but can be modified by its past experiences, such as the frequency and pattern of its firing. This plasticity is important for learning, memory, and adaptation to changes in the environment. Additionally, neurons adjust the level and type of ion channels and receptors in response to external signals and internal feedback, allowing them to maintain a certain level of activity or change their firing properties over time.

In 2010, Gal et al. extend the observational window on the single neuron in *ex vivo* developing cortical neurons. Specifically, they analysed the behaviour of synaptically isolated neurons in response to electrical stimulation. They found that there is a critical latency and critical spiking threshold that marks the transition to intermittency. The variability in neuronal responses observed in the experiments suggests that the response of individual cells to electrical stimulation is not deterministic and can exhibit a wide range of behaviours. This variability can have important consequences for the overall modelling of neurons and neural circuits. The studies suggest a need for a shift in experimental and stimulation paradigms that can account for the individual variability in neuronal responses. Three distinct phases of neuronal responses to stimulation were identified: a stable phase, a transient phase, and an intermittent phase Fig. 2.4. The

transition to intermittency is characterised by a critical latency and critical spiking threshold (Gal and Marom, 2013; Marom, 2010).

The current lack of data from very long experiments of neurons motivates this thesis, in which we provide an experimental framework for the study of long-term excitability in genetically-identified cell types.

2.4. Quantifying long-term intrinsic excitability

This portion emphasises the measure of sustained excitability over prolonged experiments lasting up to 12 hours. In order to address key questions about the complex adaptive mechanisms, underlying slow effects on cell excitability, Neuroscience makes several abstractions. First, it abstracts neuronal networks from the brain; then a neuronal microcircuits from a network; and finally, it abstracts a single neuron from the circuit effects, tackling their time-dependent intrinsic properties.

We adopted this sequence of abstractions and then conceived a novel experimental methodology, combining Optogenetics with substrate-integrated microelectrode arrays (MEA). This allowed for a detailed and systematic study of single-neuron excitability over long periods of time, while restricting our investigation to genetically-identified neuronal cell types. In particular, we decided to focus on putative glutamatergic (i.e. excitatory) neurons, whose selective expression of ShChR was ensured by the CaMKIIα promoter in the AAV-mediated transduction protocols of our choice.

In order to study long=term excitability, we apply brief and repeated photo stimuli able to elicit a single action potential, in those neurons that have been engineered to express light-activated ionic currents. Then, upon collection of the sequence of neuronal response

latency or response failures at varying stimulation frequencies and over extended periods (i.e. up to 12 h), we can indirectly access and analyse cell excitability.

3. Materials and Methods

The experimental design comprises of four distinct components in its methodology:

1. The first component involves devising and testing methods for targeting specific cell types and cell segments, and assessing expression levels of ShChR.

2. The second component involves extracellular recording of primary cortical neurons, followed by photostimulation.

3. The third component comprises intracellular photostimulation and recording of HEK293T cells.

4. Finally, the methodology involves employing various computational models.

3.1. Transgene delivery in cell cultures *in vitro*

Plasmid DNA is employed for the cell line, while AAV is required for primary neurons in vitro.

3.1.1. Transfecting Plasmids into Cells

The CAG promoter, a robust synthetic promoter commonly utilised to induce significant gene expression in mammalian expression vectors, was employed to transfect HEK293T mammalian cells with the plasmid pAAV-CAG-ShChR-eGFP (#99232, Addgene). This plasmid has demonstrated high levels of expression for both recombinant proteins like eGFP and transgenes such as ChannelRhodopsins.

3.1.2. Utilising Adeno-Associated Viral Vectors for Gene Delivery

Adeno-associated viral vector AAV particles were custom made using optimised procedures at the Leuven Viral Vector Core (LVC, KU Leuven, Belgium). For all requested AAV, the protocol consists of 1) cloning, 2) DNA plasmid preparation, and 3) AAV production with quality control.

First, HEK293T cells are transiently transfected with three plasmids: the first encodes the transgene cassette flanked with AAV2 ITRs, the second codes for the rep gene of AAV2 and the cap gene of the specific serotype requested, and the third provides the adenoviral helper functions. The resulting DNase-resistant AAV particles are quality-controlled using the qPCR method to assess a physical titer for each production. AAV vectors are always produced in mycoplasma-free conditions.

3.2. Extracellular electrophysiology

The experimental design for extracellular photostimulation and recording includes four distinct steps. The first involves building of the setup. It is followed by the long-

Promoter >	Transgenes		Serotype	Titer	Source
	ChR variant	Fluo. tag			
$CaMKII_{0.4}$ >	ShChR	mCherry	AAV2/7	7.34e+12	Dittgen et al. (2004)
$CaMKII_{0.4}$ >	ShChR - KA2	mCherry	AAV2/7	5.09e+12	Shemesh et al. (2017)
hDlx >	Chrimson	tdTomato	AAV2/5	3.72e+12	Dimidschstein et al. (2016)
mDlx >	Chrimson	tdTomato	AAV2/5	2.54e+12	Dimidschstein et al. (2016)
CMV >	-	eGFP	AAV 5	1.35e+12	Foecking and Hofstetter (1986)
mGAD65 >	-	mCherry	AAV2/7	3.10e+12	Hoshino et al. (2021)
mGAD65 >	ShChR	-	AAV2/7	3.10e+12	Hoshino et al. (2021)

Table 3.1. Tested AAVs for selective transgene expression.

term *in vitro* culturing of mammalian neurons, dissociated from rat neocortices and plated on MEA. The second requires the genetic targeting and manipulation of cells, by adeno-associated viral vectors AAV, so that putative glutamatergic neurons expressed ChannelRhodopsins variance ShChR or light-activated ion channels. The third and last step consisted in the pharmacological isolation of individual neurons, such that each neuron would be insensitive to synaptic transmission from nearby cells. With such an experimental layout, the electrical activity of neurons was monitored non-invasively and for very long times, while being evoked by repeated, brief pulses of blue light in wide-field (as illustrated in Fig. 4.3).

3.2.1. Design and construction of the experimental setup

The experimental setup is tested inside a mini-incubator using two different MEA system configurations. In both cases, the complete data acquisition uses 1–3000 Hz broadband and standard gain of 1200. The digitised data is stored on disk for offline post-processing.

MEA1060-Up-BC system and MicroElectrode Arrays MEA60

We establish our experiments on MEA of type 60MEA200/30iR-ITO-gr using a standard MEA1060-Up-BC amplifier (MultiChannel Systems, Reutlingen, Germany). This MEA has one internal reference and 59 flat round TiN electrodes of size 30 μm, arranged in an 8 x 8 layout grid with inter-electrode distance of 200 μm. The electrodes, which interface neurons cultured on the MEA surface, measure the localised electrical potential changes during spike generation (see extracellular field theory, Humphrey and Schmidt, 1990). These *source signals* are amplified by the 60 channels of the MEA pre- and filter amplifiers. Subsequently, the analogue *output signals* are sampled at 25 kHz/channel and digitised at a resolution of 16 bit using an A/D converter (MCCard, MultiChannel Systems, Reutlingen, Germany).

MEA120-Mini system and MicroElectrode Arrays MEA120

As in the MEA60 system, the setup is implemented using the new compact MEA120-Mini amplifier featuring a 24 bit A/D resolution. We increase the throughput of our experiments with the MEA of type 120MEA100/30iR-ITO-gr (MultiChannel Systems, Reutlingen, Germany), which has four internal reference and 120 flat round TiN electrodes in a 12 x 12 layout grid and inter-electrode distance of 100 μm.

Custom-made LED devices for photostimulation

We activate the genetically modified neurons using light flashes of 1 ms duration at frequencies of up to 50 Hz. To achieve this, we employ custom made LED devices. In all experiments, the power density of the emitted light reaching the electrodes area

is 2 mW/mm^2 (measured by a calibrated photodiode; 818-ST2-UV, Newport Spectra-Physics, Netherlands).

In addition to the MEA60 system, LED device is assembled (Pulizzi et al., 2016). A blue (470 nm) light-emitting diode (LED, Rebel, Quadica Development, Canada) is centred in a parabolic reflector lens to uniformly distribute (collimate) the emitted light in wide-field at the bottom of the MEA. The LED is powered by a low-voltage DC constant current driver (BuckPuck, LUXDrive, USA), which regulates the current to avoid damage or thermal runaway of the LED. It does so by delivering a constant forward current, while compensating for changes in forward voltage[1]. A stimulus generator with a voltage output (STG2008, MultiChannel Systems, Reutlingen, Germany) is then connected to the LED device. The STG2008 receives programmed TTL[2] pulses *via* a BNC connector to define the timing and length of the output pulses for triggering the LED with a 20 μs precision.

In addition to the MEA120-Mini system, the signal collector unit SCU is employed to control a custom made aoLED device (CyNexo, Italy) for precise monitoring as well as design of the light output. The aoLED accepts 0–5 V voltage inputs, which can be analogue or TTL compatible digital input signals, and integrates a linear and stable LED driver, able to generate a high bandwidth (<1 MHz) and high intensity light signal. The embedded light power sensor is used to monitor the generated light signal, recorded in the analogue output channel of the InterFace Board IFB connected to a dedicated computer for recording.

[1] The forward current is the amount of current flowing through the LED; the forward voltage is the amount of voltage needed to get current to flow across the LED.

[2] A TTL input signal is defined as "low" when between 0 V and 0.8 V with respect to the ground terminal, and "high" when between 2 V and VCC (5 V).

Surface coating of MicroElectrode Arrays

Prior to cell plating, the microelectrode arrays MEA surface is functionalised for favouring cell attachment. A thin mono-layer of poly-cation particles of Polyethileneimine (50 wt.% in H_2O PEI, Mw = 750 kDa, Mn = 60 kDa; SKU: 181978, Sigma-Aldrich) is formed on the MEA surface through electrostatic bonds with the negatively ionised MEA surface, which is achieved by exposing MEA to air plasma. The plasma cleaning process removes micro-contaminants, generates negatively charged surface species, and increases surface hydrophilicity (wetting). The plasma is generated at 0.1 mbar and radio frequency electromagnetic waves at a power of 10 W using a plasma cleaner (Zepto BRS, Diener electronic GmbH, Ebhausen, Germany). After plasma cleaning, sterilised MEA are suction dried and each dish is filled with 1 mL of 0.1 wt.% PEI water dispersion, prepared by bath ultrasonication for at least 40 min. Following an overnight incubation at room temperature, unbound PEI is removed by aseptic water rinse. The dishes are suction dried before seeding the prepared suspension of dissociated cells.

Primary neuronal culture preparations

Cortical and hippocampal primary cultures are prepared from *Wistar* newborn rats within 24 h from birth (i.e. post-natal day 0 - P0). Tissue from six P0 pups is dissected from the superior part of both neocortices, cutting along the axial plane at a thickness of 1 mm. Then the two hippocampi are carefully extracted. Cells are isolated through steps of chemical and mechanical dissociation, and the obtained cell suspension is seeded at a density of 6500 cells/mm^2. The cell medium is a standard Minimum Essential Medium (MEM) (21090022, Gibco^{TM}) supplemented with 5 vv.% heat-inactivated horse serum (26050088, Gibco^{TM}), 20 mM $D^{(+)}$Glucose (G7528, Sigma-Aldrich), 10 μg/mL gentamycin (15090046, Gibco^{TM}) and L-glutamine (GlutaMAX^{TM}). For cell seeding and

up to 7 *div*, we use a custom made cell medium H-MEM with relatively high L-glutamine concentration 100μM. For medium change after 8 *div*, we use the cell medium N-MEM which contains a reduced concentration of L-glutamine 50 μM to prevent overgrowth of glial cells and maintain a healthy culture in the long-term. The MEA cultures are maintained for up to 35 *div* in a conventional cel culture incubator.

AAV-mediated transduction of primary neurons

Cells are infected at 5 *div* with vectors designed for heterologous expression of ShChR labelled with the fluorescent tag mCherry under the CaMKIIα promoter (Fig. 4.3B). For this purpose, we use infectious Adeno-Aassociated Viral particles AAV, custom-produced at the Leuven Viral Vector Core LVC according to an established protocol (Van der Perren et al., 2011). We infect cells using concentrations between 4500 and 9000 gc/cell in 360 μL of medium applied in the dish by total medium replacement.

3.3. Extracellular recording protocols and data analysis

Photostimulation of synaptically-isolated neurons

All experiments are performed after 19 *div*, in accord with published data on neuronal network and cell maturation (Marom and Shahaf, 2002; Pulizzi et al., 2016) and ShChR expression (Klapoetke et al., 2014).

At the beginning of each experimental protocol, the main excitatory (AMPA, NMDA) and inhibitory ($GABA_A$) postsynaptic receptors are blocked. We use 20 μM APV, 10 μM CNQX, and 5 μM gabazine, respectively.

Experimental protocols

The photostimulation pulse is 1 ms, which is a short enough time to evoke a spike at a light power density of 2 mW/mm^2. The initial stimulation rate is set at 1 Hz. At this low rate, typically most of the microelectrodes in a MEA capture both reliable and precise responses [3] with preserved spike waveforms (Fig. 4.5). These electrodes are used further in the experiments. The stimulation rates in the remainder of the protocol range between 2 to 50 Hz, which is the upper limit for the kinetics of the ShChR (Klapoetke et al., 2014) at which photostimuli are able to faithfully evoke spikes following the same spike probability as with electrical stimulation. The stimulation time is between one and twelve hours.

[3] Reliability here means that a spike is evoked after each stimulus; precision refers to low variability in the delay between stimulus and response.

Downstream processing

We recorded the extracellular electrophysiological activity of primary cultured neurons, growing on 100 MEA. Raw voltage waveforms were sampled at 25 kHz and digitised a resolution of 16 bit. Files were stored in MultiChannel Systems' proprietary file format [4]. as well as in the open HDF5 file format [5]. Once converted into the HDF5 format, files were processed offline by custom data analysis pipe-line, entirely based on MATLAB R2022 (The MathWorks, Inc., Natick, MA, USA). Briefly, a single HDF5 file stores raw data hierarchically in *groups*. Associated meta data is also available, as attachments to each of the groups. With a syntax similar to the Unix filesystem, we access group '/Data/Recording_0/AnalogStream/' which contains two analogue output streams each having two datasets: 'ChannelData' and 'InfoChannel'. The first output stream, labelled 'Electrode', contains 'ChannelData' with 60/120 channels of electrode raw data; the second stream, termed 'Auxiliary', holds a dataset with only one channel, recording the aoLED output[6]. For both streams, the 'InfoChannel' dataset carries respective info for conversion from recorded binary values to voltage. Each channel is read in *slices* of equal size [1, 25k sample points], split along logical boundaries in the array representation of the data (Fig. 3.1). Despite we working with very large files (> 100 GB), only one *slice* is loaded into memory (RAM) at a time of processing making data handling and manipulation possible.

[4] File extensions: *·mcd* file extension of the MC Rack software (old); the *·msrs* file extension of the MC Experimenter software (new).

[5] Hierarchical Data Format version 5 (The HDF Group): an open source binary data format, explicitly designed to store and organise very large data sets, easily accessible from Matlab (HDF5 version 1.10.8) and Python.

[6] The forward voltage is the amount of voltage needed to get current to flow across the LED.

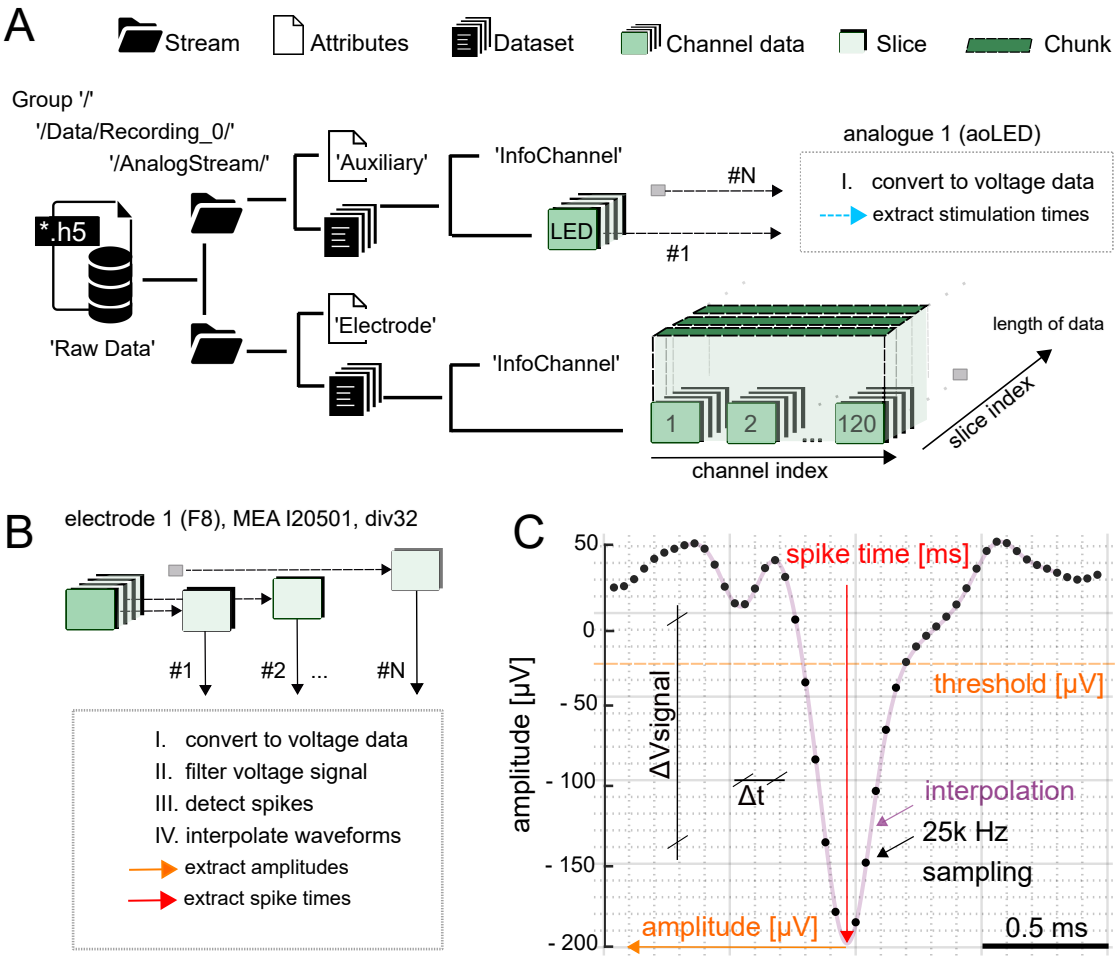

Figure 3.1. Downstream processing and analysis of analogue raw data. A: In the top panel, the relation between the raw data (hd5) and the measurement data is schematically shown. **B:** In the bottom left panel, we show the data processing algorithm as applied to slices 1 through N slices. **C:** In the bottom right panel the relevant features extracted upon interpolation of the spike waveform are shown.

Raw-voltage waveforms processing

Electrode channels are accessed serially in order of time. For a channel, each slice is processed in five stages (Fig. 3.1A). First, the loaded data of a *slice* is converted from binary to raw voltage data based on the conversion data in the dataset. Secondly, these

are filtered with an elliptic band pass between 400 and 3000 Hz (MATLAB 'filtfilt' and 'ellip') followed by a step for spikes identification (Fig. 3.1C). Typically, spike detection algorithms use automatically calculated amplitude threshold as a multiple of the standard deviation of the background noise, followed by a time window in which further detection is suppressed ("detection dead time"). In our case, however, each electrode captures spikes from multiple neurons, which are simultaneously activated. Their spikes can occur as partially overlapping, therefore falling into each others detection dead time, which leads to many spikes over the course of the experiment being left undetected. This is why we introduce a modified detection approach which uses a threshold on the voltage increments $\Delta V/\Delta t$ in addition to the amplitude threshold. At a sampling rate of 25 kHz, instantaneous voltage increments which precede the local negative amplitude peak (spike onset) are much more pronounced than within the background noise. After a sum of three consecutive ΔV crosses the threshold, we find the first local minimum and index it. We then extract the 15 sampling points prior and 20 after each index as voltage snippets. In the forth step, these are interpolated by a piece-wise cubic spline method (MATLAB 'interp1') to approximate spike waveforms, in order to accurately estimate **spike times** and the corresponding **spike amplitudes** (Fig. 3.1C). All **spike waveforms** are aligned to their negative amplitude peaks and saved for spike sorting.

Photostimulation signal processing

The aoLED digital or analogue output channel is processed as follows. Each *slice* is converted from binary to digital or raw voltage data based on the associated conversion info, respectively. In the case of the analogue LED output, voltage values 0–5 V reconstruct positive, rectangular pulses defined by an amplitude of 5 V and a duration of 1 ms. The number of pulses per second is the frequency of stimulation. The time points at the onset of each stimulation pulse are extracted as **stimulation times** (Fig. 3.1B).

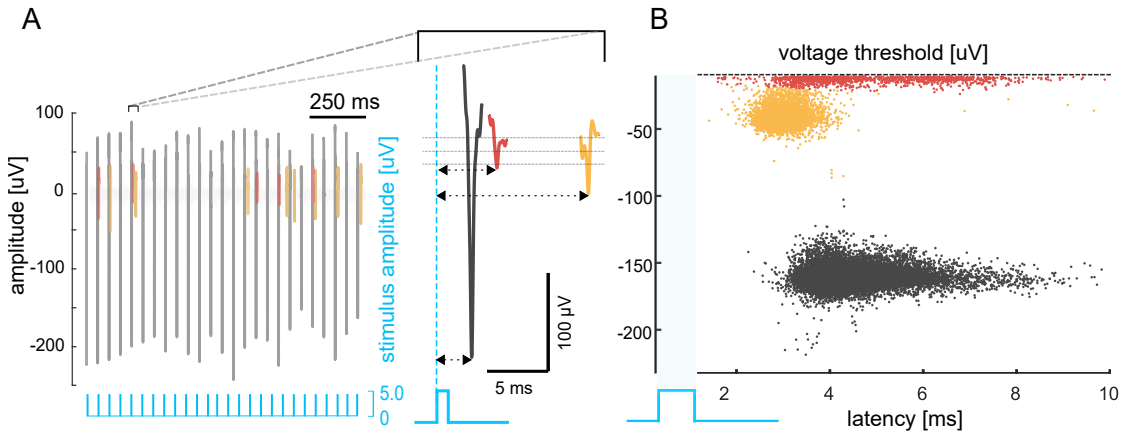

Figure 3.2. Illustration of the spike sorting and classification steps. A: In the left panel, a voltage trace is shown with spikes from multiple neurons per stimulus (black, red and orange) classified as recorded from three separate neurons. **B:** All detected spikes from a 3-hour voltage trace were subjected to spike sorting and classification based on the spike features (spike latency and amplitude), as shown in the right panel.

Finally, we calculate **spike latencies** for all the spike times as the delay from the stimulation times which evoked them which are used for spike sorting and classification (Fig. 3.2).

Spike sorting and classification

Each electrode in a MEA often captures spikes from more than one neuron (multi-unit recording, Fig. 3.2A). Therefore, all spikes need to be grouped into separate neuronal units, each corresponding to an individual neuron. This classical problem in Neuroscience is addressed by many clustering algorithms (Wang et al., 2019) which parse individual spike trains depending on the temporal structure of the waveforms. At the beginning, we employed the superparamagnetic clustering SPC method, which is motivated by the phenomenon of superparamagnetism in physics (Chaure et al., 2018). Specifically, we tested the *Wave Clus 3* algorithm. Our results, however, revealed a tendency to under-classify or over-classify spikes into an erroneous number of clusters,

likely due to the incremental changes in spike waveforms observed during prolonged stimulation. This manifests in the sorting of spikes from a single neuron into three distinct clusters, as exemplified by the application of SPC to a single neuron dataset (see Fig. 4.5). In itself though, the misclassification provides a valuable insight into the temporal evolution of the waveform (Sec. 4.1.1).

In order to tackle the challenge of sorting spikes into clusters, we have developed a new algorithm that operates along the dimension of latency. Our approach involves representing each spike as a point in a 2D feature space based on two extracellular characteristics of excitability: amplitude and latency. To estimate the maximal number of neurons spiking, we rely on the maximal number of spikes evoked by a photostimulus over the course of the experiment. in the beginning, we focus on the transient phase and create post-stimulus groups of data points sequentially, with the first group containing the first spikes and so on. We then use these groups to grow a kD-Tree. By utilising the kD-tree nearest neighbour searcher model, we can re-classify query points into the class with the highest representation among their respective nearest neighbours. If the resulting cluster classes are well separated, we save them as separate neuronal units for further statistical analysis. If the voltage threshold line cuts off the amplitude values, then the corresponding cluster class is excluded from the analysis as shown in Fig. 3.2B.

Spike train statistics

The spiking activity of a neuron is reduced to a sequence of spike times i.e., a spike train $S_N = \{t_1, t_2, ..., t_{\max}\}$ or in mathematical terms - a point process on the line (Thurner et al., 1997), N being the number of spikes. In order to characterise the structure and variability in the number of spike occurrences over different timescales, a spike train is modelled as a *point process* (Turcott and Teich, 1996). To begin with, real time is

subdivided into non-overlapping, successive bins of equal width T. Then the number of spikes occurring per bin is counted. This sequence forms a discrete-time stochastic process of non-negative integers. For small enough bin widths T, each bin will eventually contain at most one spike, thus generating a sequence with values of either 0 (no spike) or 1 (spike). For increasing bin sizes, we investigate how the occurrence of spikes fluctuates while observed over longer periods of time. For this, we define the sequence of counts $Z(T) = \{Z_1(T), Z_2(T), ...Z_N(T)\}$, where $Z_k(T)$ is the spike count in the k^{th} bin ($1 \leq k \leq N$) (see Figure4_methods for visualisation of the process).

We then apply the *normalised variance* or *Fano factor* (Fano, 1947):

$$F(Z_T) = \frac{\sigma^2_{F(T)}}{\mathbb{E}[Z(T)]},$$

where $\mathbb{E}[Z(T)]$ is the mean count:

$$\mu_{Z(T)} = \frac{1}{N} \sum_{k=1}^{N} Z_k(T),$$

and $\sigma^2_{F(T)}$ is the variance defined as:

$$\sigma^2_{F(T)} = \frac{1}{N} \sum_{k=1}^{N} (Z_k(T) - \mathbb{E}[Z(T)])^2.$$

A complementary method is the Allan factor A(T) or the *normalised Haar-wavelet variance* (Lowen and Teich, 1996).

$$A(T) = \frac{\mathbb{E}[(Z_{k+1}(T) - Z_k(T))^2]}{2\,\mathbb{E}[Z(T)]}.$$

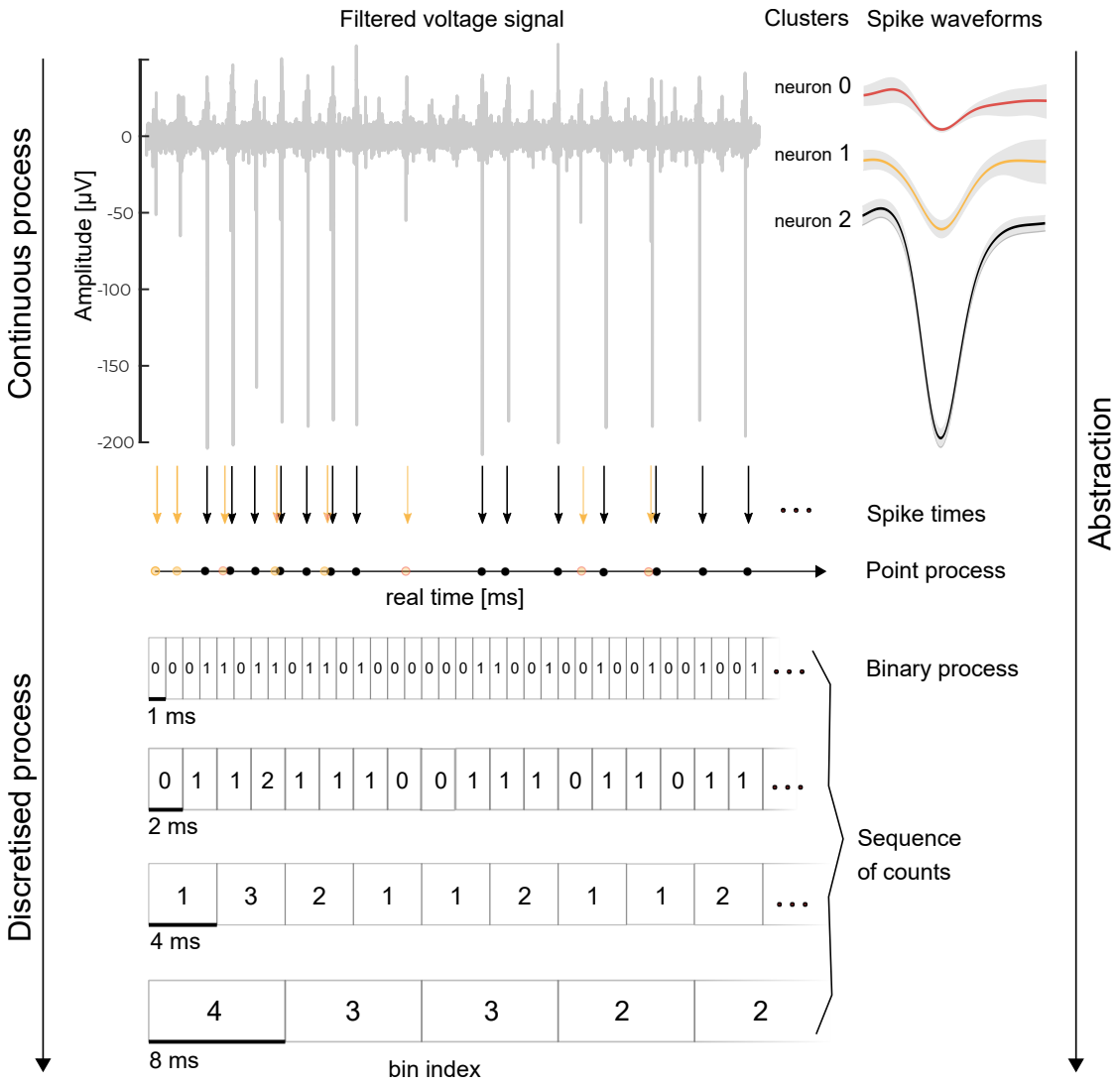

Figure 3.3. Pipeline for generating sequences of counts with varying bin size. At the top, a voltage trace with spikes is shown. The right side displays spike waveforms overlaid with differently coloured mean waveforms as in Fig. 3.2. From it, spike times are extracted for neuron '1' and '2' for further analysis (black and yellow dots). Only for neuron '1', the process of generating sequences using different sized bins is illustrated (see bin counts in bottom half).

We analyse $Z(T)$ in a range of 300 values of T ($1\,\text{ms} \leq T \leq t_{\max}/4$), where t_{max} is the last spike time. The computed values of F(T) and A(T) are plotted on a doubly logarithmic scale. The slopes of both the Fano factor and Allan factor curves in the large T regime

give the estimates α_F and α_A of the real scaling exponent α, such that $F(T) \sim T^{\alpha_F}$ and $A(T) \sim T^{\alpha_A}$. Linear regression algorithm is used to calculate the slope by automatically selecting the maximal number of data points, which can be linearly fitted at a minimal MSE (mean square error). We use α_A to classify long-term dynamics in the spiking of single CaMKIIα/ShChR neurons, with the possibility to distinguish between fG_n versus fB_m derived processes outside a theoretically derived uncertainty range (0.87–1.13) (Eke et al., 2000; Turcott and Teich, 1996).

Fano factor analysis is used to estimate the range of correlations, since the power-law in the Fano curve starts at least a decade before the onset in the Allan curve. We validate the existence of correlations among counted events in consecutive bins with increasing width T by testing ten surrogate spike trains derived from the original data as follows. We first compute the inter-spike times $ISI_{original}$, then shuffle them by random permutation (MATLAB 'randperm'). The values in the resulting array $ISI_{shuffled}$ are then cumulatively summed to obtain the new spike times *i.e.*, surrogate spike train. This procedure keeps the mean, variance, and frequency distribution identical to those of the original spike train, but eliminates any existing long-range correlations between the events of the original process. Simulated time series of a homogeneous Poisson process and a Brownian motion process with $\mu = \sigma = 1$ are as well tested for cross-validation (not shown).

3.4. Intracellular electrophysiology

This section delves into the dynamics of ShChR over realatively lengthy periods of time.

3.4.1. HEK293 cell cultures and transfection

Non-spiking HEK293 cells Acc number: 85120602 Lot:18H003 are cultured in DMEM/F12 medium supplemented with 10% FBS, 1% penicillin/streptomycin, and 1% sodium pyruvate. For recording, cells are plated on glass coverslips at 20% confluence, transfected with a kit x-treme GENE 9 DNA transfection reagent and recorded via whole-cell patch clamp, two days after transfection 1.25 μg of DNA was delivered.

3.4.2. Intracellular recording protocols and postprocessing

Whole-cell patch clamp experiments

Whole-cell patch clamp recordings are performed in isolated non-spiking HEK293 cells to avoid space clamp issues due to the constitutive expression of gap juntions on HEK cells. Visualisation of the positive trasnfected cells was done through an inverted microscope Olympus Ix70 equipped with ×20 and ×40 objectives and a typical cube for mCherry visualisation (excitation Filter 510-550, dichroic Mirror 593 and Barrier Filter 610IF). All recordings were performed using the Axopatch 200B amplifier and the Digidata 1440 digitiser (Molecular Devices, LLC, UK) at room temperature. To ensure accurate measurements, we use cells with access resistance <25 MΩ and holding current within $\pm$50 pA. Typical membrane resistance was between 500 MΩ and 2 GΩ. Patch pipettes were made of borosilicate glass (WPI, Sarasota, FL, USA) with a PP-830 puller (Narishige, Tokyo, Japan) with tested resistance between 3 and 6 MΩ. Photostimulation of patch-clamped cells was performed using a Olympus mercury burner light lamp (U-RFL-T) interposing with an Olympus U-MWIB2 fluorescence microscope reflector cube equipped with an excitation Filter 460-490, dichroic Mirror 505 and Barrier Filter 520IF. Additionally, dense optic filter (0.5 - 0.7) was added to the optical path for achieving

a light density of (2 mW/mm^2) at the bottom of the sample. The photostimulation protocol was designed then implemented by use of a TTL controlled mechanic shutter (Uniblitz VCM-D1 shutter driver).

To describe the kinetics of the channel, the extracellular *ringer* solution, adjusted with NaOH, comprised 125 mM NaCl, 2 mM KCl, 3 mM $CaCl_2$, 1 mM $MgCl_2$, 10 mM HEPES, 30 mM glucose, and had a pH of 7.3 with an osmolarity of 305 mOsm. The intracellular solution, adjusted with KOH, contained 125 mM K-gluconate, 8 mM NaCl, 0.1 mM $CaCl_2$, 0.6 mM $MgCl_2$, 1 mM EGTA, 10 mM HEPES, 4 mM Mg-ATP, 0.4 mM Na-GTP, and had a pH of 7.3 with an osmolarity of 295—300 mOsm, adjusted with sucrose. The inward current was measured using 1 ms light pulses at a rate between 1 and 50 Hz.

3.5. Mathematical models for long-term excitability dynamics

Through a step-by-step investigation (Appx. A), we arrived at the optimal Wang-Buzsáki-Güler stochastic model as the ideal foundation for executing the computational optogenetics.

3.5.1. Modelling of the stimulation input

The stimulation input is modelled as at train of stimuli. We assume a rectangular function, defined as:

$$\Pi(t) = \begin{cases} 0 & \text{if } |t| > \Delta \\ 1 & \text{if } |t| \leq \Delta \end{cases} \tag{3.1}$$

where Δ is the half duration of the input. The input is modelled as a train of stimuli. The previous rectangular equation is revised as follows:

$$\Pi_{train}(t) = I \sum_{k=1}^{n} \Pi(t - kT). \tag{3.2}$$

3.5.2. Wang-Buzsáki-Güler stochastic model

The stochastic model exploited was introduced by Güler in (Güler, 2013), and falls into the conductance noise family of models.

$$\mathrm{I} = \mathrm{C_M}\frac{d\mathrm{V}}{dt} + \underbrace{\bar{g}_{\mathrm{K}}\Psi_{\mathrm{K}}(\mathrm{V} - \mathrm{E_K})}_{\mathrm{I_K}} + \underbrace{\bar{g}_{\mathrm{Na}}\Psi_{\mathrm{Na}}(\mathrm{V} - \mathrm{E_{Na}})}_{\mathrm{I_{Na}}} + \underbrace{\bar{g}_{\mathrm{L}}(\mathrm{V} - \mathrm{E_L})}_{\mathrm{I_L}} \tag{3.3}$$

where Ψ_{K} and Ψ_{Na} are defined as:

$$\Psi_{\mathrm{K}} = n^4 + \sqrt{\frac{n^4(1-n^4)}{\mathrm{N_K}}}q_{\mathrm{K}} \tag{3.4}$$

$$\Psi_{\mathrm{Na}} = m^3 h + \sqrt{\frac{m^3(1-m^3)}{\mathrm{N_{Na}}}}h_{\mathrm{Na}}q_{\mathrm{Na}} \tag{3.5}$$

The periodic stochastic variables q_K and q_{Na} satisfy two second-order linear stochastic differential equations, which can be written as four first-order stochastic differential equations:

$$\begin{cases} \tau \dot{q}_K &= p_K \\ \tau \dot{p}_K &= -\gamma_K p_K - \omega_K^2[\alpha_n(1-n) + \beta_n n]q_K + e_K \\ \tau \dot{q}_{Na} &= p_{Na} \\ \tau \dot{p}_{Na} &= -\gamma Na p_{Na} - \omega_{Na}^2[\alpha_m(1-m) + \beta_m m]q_{Na} + e_{Na}. \end{cases} \tag{3.6}$$

where γ_K, ω_K, α_n, β_n, N_K, e_K, γ_{Na}, ω_{Na}, α_m, β_m, N_{Na}, and e_{Na} are constants.

The first equation for each variable gives the rate of change of the activation variable itself, while the second equation gives the rate of change of its corresponding momentum variable, which is related to the stochastic force acting on the variable.

The constants γ_K and γ_{Na} represent the damping coefficients, which account for the dissipation of energy due to ion movement through the channels. The constants ω_K and ω_{Na} represent the natural frequencies of the channel activation variables, while α_n, β_n, α_m, and β_m are gating variables that describe the voltage-dependent opening and closing of the potassium and sodium channels.

The constants N_K and N_{Na} represent the number of channels, while e_K and e_{Na} are the external stimulations that influence the activation variables. The time constant τ is related to the scale of the dynamics.

The gating variables n, m, and h are described by two additional stochastic differential equations (SDE) similar to those presented in the literature (Fox, 1997). These equations

follow the fundamental Wang-Buzsáki model and are given by:

$$\begin{cases} \dot{n} = \alpha_n(1-n) + \beta_n n + \eta_n \\ \dot{h} = \alpha_h(1-h) + \beta_h h + \eta_h \\ m = \dfrac{\alpha_m}{\alpha_m + \beta_m} \end{cases} \tag{3.7}$$

The numerical simulation method was modified to solve the stochastic SDE. The Gaussian noise terms have zero means, with variances given by:

$$\begin{cases} Var(\epsilon_K) = \gamma_K T_K[\alpha_n(1-n) + \beta_n n] \\ Var(\epsilon_{Na}) = \gamma_{Na} T_{Na}[\alpha_m(1-m) + \beta_m m] \\ Var(\eta_n) = \frac{\alpha_n(1-n)+\beta_n n}{4N_K} \\ Var(\eta_h) = \frac{\alpha_h(1-h)+\beta_h h}{N_{Na}} \end{cases} \tag{3.8}$$

The fixed parameters in the stochastic dynamics are retrieved from reference (Fox, 1997), and they remain constant throughout the simulation. The diffusion coefficients are carefully constructed to approximate the stochastic dynamics. The drift coefficients contain stochastic components, q_K and q_{Na}, which are designed to capture non-trivial cross-correlation persistence (NCCP) effects. These effects refer to the correlation between the fluctuations in the transmembrane voltage and the component of open channel fluctuations, which arises due to gate multiplicities. The equations that describe q_K and q_{Na} are written using the formalism of the Brownian oscillator, since they exhibit similarities to NCCP properties.

3.5.3. Single compartment morphological soma model

Neurons are not mere points, but rather complex spatial entities, composed of dendrites, soma, and axon compartments, each with its own distinct function. When a powerful stimulation pulse is applied to a compartment, the resulting signal propagates through the neuron, altering the excitability of each compartment it passes through. This excitability threshold relies on internal variables, such as ion channel properties and membrane potential, as well as the stimulation current entering the compartment. The resulting action potential, generated when the stimulation is sufficient, then travels along the axon. However, if there is conduction failure in a compartment on the propagation path, the signal will not reach its final destination, and no action potential will be detected. This can happen due to factors such as inadequate membrane depolarisation or a inactivation of ion channels in that compartment.

A single compartment morphological soma model is a simplified representation of a neuron's soma, or cell body, that is used to study the basic properties of neuronal behaviour. This type of model assumes that the soma is a single compartment. We assume, the membrane potential at a neuron's soma is evenly distributed over its entire surface. The soma is considered to be "electrotonically compact" and can be regarded as a sole "compartment". This compartment features a solitary membrane potential, membrane capacity, and membrane resistance. We present here the outcomes of a single compartment model that incorporates morphological variables, in opposition to preceding chapters. The construction of this realistic neuron model involved utilising the Neuron-python package to conduct simulations.

As a development from the point neuron model we use the Neuron-Python environment to build a *real* soma model, characterised by relevant morphological parameters:

$$\begin{cases} n_{seg} = 1, \\ L = 100, \\ R_a = 35.4, \\ diam = 500, \\ c_m = 0.5, \end{cases} \tag{3.9}$$

where n_{seg}, L and $diam$ are morphological parameters, R_{ais} is the cytoplasmic resistance and c_m is the capacitance. From the conclusions of the previous sections, the neuron's ions behaviour is simulated using is a combination of the Wang-Buzsáki and Güler stochastic model.

As in the previous models, a train current pulses, with duration dt, an amplitude and a period, is injected into the soma segment of the real neuron.

3.5.4. Computational Optogenetics and implementation of a ChR2 model

ChR2 was modelled as a non-specific ion channel with four states: two closed states (C1, C2), and two open, conducting states (O1, O2) (Foutz et al., 2012). To incorporate the ChR2 biophysical mechanism into NEURON, we had to adjust and compile the mod file that contains the NMODL code. Through this process, we developed a NEURON simulator variant of the ChR2-H134R model, which depends on voltage and light sensitivity and was derived through experimental research by (Williams et al., 2013). In 2018, Michele Giugliano released the NEURON model implementation of this ChR2 version on ModelDB.

$$\begin{cases} \frac{dO_1}{dt} & = G_{a1}C_1 - (K_{d1} + e_{12})O_1 + e_{21}O_2 \\ \frac{dO_2}{dt} & = G_{a2}C_2 - (K_{d2} + e_{21})O_2 + e_{12}O_1 \\ \frac{dC_2}{dt} & = G_{d2}O_2 - (G_{a2} + K_r)C_2 \\ 1 & = O_1 + O_2 + C_1 + C_2 \end{cases} \tag{3.10}$$

where $O1$, O_2, C_1, and C_2 are functions of time t. The first equation describes the rate of change of O_1, the concentration of an open state of a receptor or ion channel. It depends on the concentration C_1 of a ligand that activates the receptor, the dissociation constant K_{d1}, the rate constant e_{12} for interconversion between O_1 and O_2, and the rate constant e_{21} for reverse interconversion. The second equation is similar, but for O_2, which depends on C_2, K_{d2}, e_{21}, and e_{12}. The third equation describes the rate of change of C_2, the concentration of the ligand, which is produced at a rate G_{d2} and decays due to binding to C_2 or unbinding to the extracellular compartment with rate constants G_{a2} and K_r, respectively. The last equation simply states that the sum of all four concentrations is constant and equal to 1, which is a normalisation constraint.

In order to accurately describe the response of ChR2 current to a light pulse, six empirical measures are employed in the model. These measures include two amplitude measures, namely peak current (I_p) and steady-state current (I_{ss}), as well as four kinetic measures such as time constant of activation (τ_{ON}), deactivation (τ_{OFF}), inactivation (τ_{INACT}), and recovery from inactivation (τ_R). These parameters, which capture the morphology, are determined through experimental traces recorded at varying voltage and light intensity levels. To ensure that the ChR2 model can be used for simulations under physiological conditions, temperature scaling factors, or Q10 parameters, are incorporated into the model. Q10 values for the kinetic parameters, as well as for the I_{ss}/I_p ratio, were derived using experimental data and were found to be independent of voltage. Typically, higher

temperature results in faster kinetics and a larger fraction of the sustained current (I_{ss}). However, for the wavelengths (470 nm) and low light intensity levels considered, any temperature changes caused by optical stimulation are negligible. Finally, ChR2 transmembrane channel conductance is influenced by factors such as membrane voltage (V), reversal potential (E_{ChR2} set to 0 mV), and channel conductance (g_{ChR2}). During illumination, the current (i_{ChR2}) to be added to Eq. 3.9 is defined by these factors as follows:

$$i_{ChR2} = 0.001\, g_{ChR2}\, \delta_V (O1 + \gamma O2)(V - E_{ChR2}) \tag{3.11}$$

where γ is the ratio of conductances in the states O2/O1, δ_V is a voltage-specific constant.

The uniform insertion of ChR2 opsin dynamics in the soma compartment of the cell, and the neuron membrane circuit model is modified as in Fig. 3.4. As in the previous section, we consider the Wang-Buzsáki model for the membrane voltage dynamics, with the addiction of i_{ChR2}, and Güler stochastic model. The photostimulation protocols is, in congruence with previous simulations, a train of light stimuli with defined frequency, duration and intensity of the light pulse as in Eq. 3.2.

3.5.5. Markov model of long-term ShChR dynamics

A Markov model is a simplified phenomenological representation of (bio)physical process dynamics, described quantitatively as a set of discrete states and by the ease of transition through time from one state to another. Based on the experimental data, we propose to partition five distinct states at each moment in time: two "excited" E1 and E2 (open channel), two "inactive" (I1 and I2 (closed, recovering channel), and one "ready" state R (closed, ready channel).

The kinetic relationship between these states can be visualised by a five-state Markov scheme.

$$\begin{array}{ccccc} & & \text{E1} & & \\ & \swarrow & \uparrow & \nwarrow & \\ \leftarrow & & \text{R} & & \rightarrow \\ & \searrow & \uparrow & \swarrow & \\ & & \text{E2} & & \end{array}$$

$$\text{I1} \qquad \text{I2}$$

- Excited transition R $\rightarrow$ E_1 is associated with probability e_1
- Excited transition R $\rightarrow$ E_2 is associated with probability e_2.
- Recovery transition I_1 $\rightarrow$ R is associated with a rate r_1
- Recovery transition I_2 $\rightarrow$ R is associated with the rate r_2
- Inactivation E $\rightarrow$ I is associated with rate τ_i which is set to 0.01.

$$R + E_1 + E_2 + I_1 + I_2 = constant \tag{3.12}$$

$$\frac{d(R + E_1 + E_2 + I_1 + I_2)}{dt} = 0 \tag{3.13}$$

We set the constant to 1, upon appropriate normalisation of the individual state variables R, E, and I. We associate to each transition a kinetic rate, which can be equivalently expressed also as the inverse of a time constant.

We assume that the activation of ShChR occurs extremely rapidly, and it is associated to a precise time (e.g., ShChR $\tau_{on} \approx 2.3$ ms); at the time of a photostimulation pulse, a percentage of ShChR opens and R depletes with a probability $\alpha_1 + \alpha_2$:

$$\text{R} = -(\alpha_1 + \alpha_2)\text{R} \qquad \text{and} \qquad \frac{dR}{dt} = \left(\frac{\text{I}_1}{\tau_1} + \frac{\text{I}_2}{\tau_2}\right) \tag{3.14}$$

The inactivation processes are also fast (e.g. ShChR $\tau_{\text{off}} \approx 4.6$ ms). The open ShChR close with rates τ_i.

$$\frac{dE_1}{dt} = \alpha_1 R - \frac{E_1}{\tau_i} \qquad \text{and} \qquad \frac{dE_2}{dt} = \alpha_2 R - \frac{E_2}{\tau_i} \tag{3.15}$$

The recovery processes are instead much slower than the inactivation ones.

$$\frac{dI_1}{dt} = \frac{E_1}{\tau_i} - \frac{I_1}{\tau_1} \qquad \text{and} \qquad \frac{dI_2}{dt} = \frac{E_2}{\tau_i} - \frac{I_2}{\tau_2} \tag{3.16}$$

We simulate the model numerically and optimise the parameters for each of the photostimulation frequencies used in the experimental data. We make conventional choices for some of the parameters that respects our assumptions above.

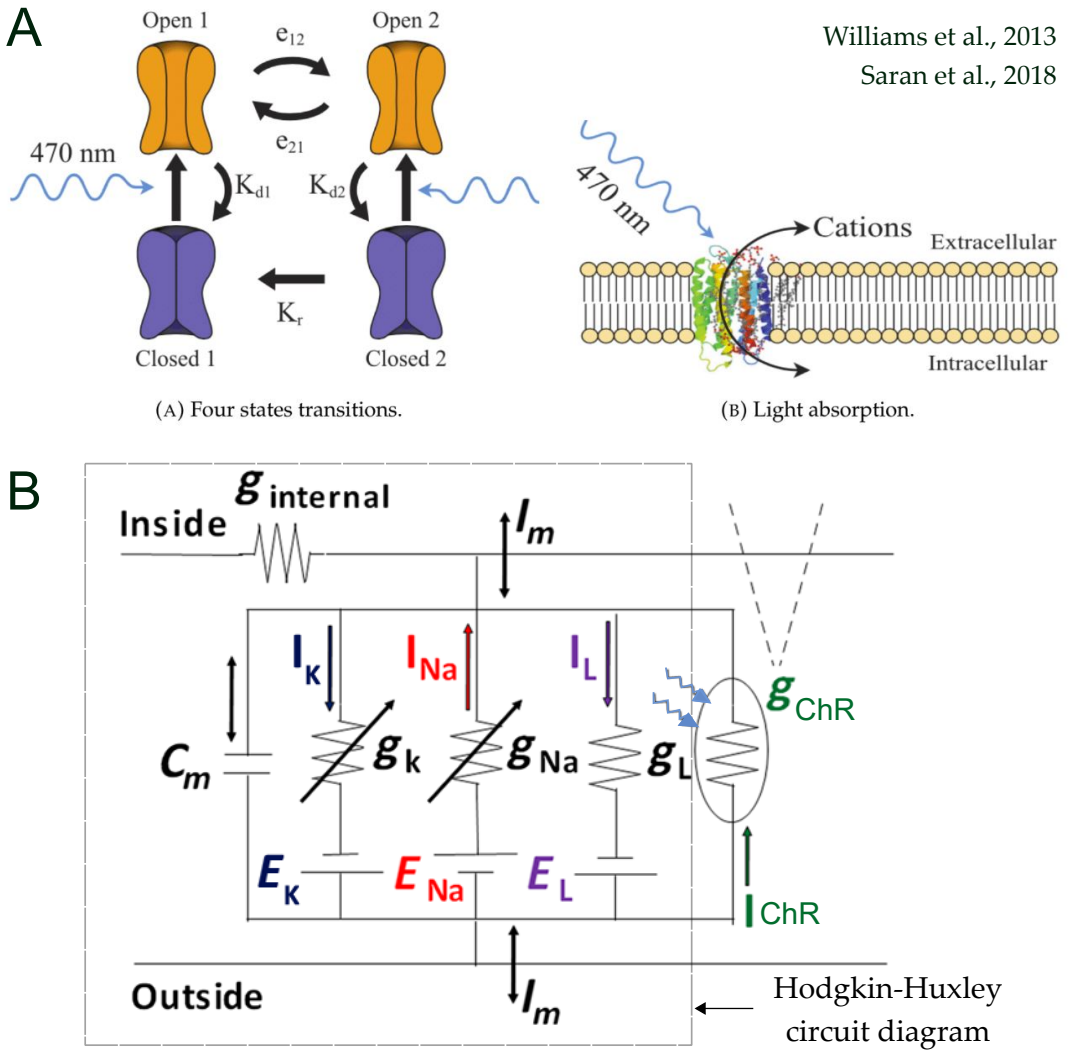

(A) Four states transitions. (B) Light absorption.

Figure 3.4. Equivalent electronic circuit of a neuron with expressed ChR channels. The electrical properties of a neuron, including its cell membranes, intracellular plasma, and channel proteins, can be compared to those of electronic circuit components. The properties presented are voltage, current, resistance, conductance and capacitance: C_m is the membrane potential, I_{K}, I_{Na}, and I_{L} are the ionic currents; g_K, g_Na, and g_{L} are the voltage-dependent conductances (as in Hodgkin and Huxley); g_{ChR} is the light-dependent conductance which is governed by the ChR photocycle. Panel A *adapted with permission from* Williams et al. (2013) showing the four-state photocycle of ChR2; Panel B is adapted from Saran et al. (2018).

4. Results

This chapter presents the experimental characterisation of the dynamics of response latency, during repeated photo-stimulation of glutamatergic cells. Such a characterisation is supported by a thorough statistical analysis and it is contrasted with the numerical simulations of neuronal models. The material presented here is currently in an advanced stage of preparation as a manuscript for submission to a peer-reviewed journal.

4.1. Implementation of the methodology

Targeting the soma of glutamatergic neurons

The promoter for CaMKIIα is specific to neurons and only expressed in excitatory neurons found in the neocortex, hippocampus, and pyramidal neurons. By utilising the CaMKIIα promoter in transgene expression, we obtain preferred ShChR expression in putative excitatory neuron populations (Fig. 4.1). An attempt was made to test the expression of somatic channelrhodopsin (CaMKIIα-KA2), but it proved ineffective.

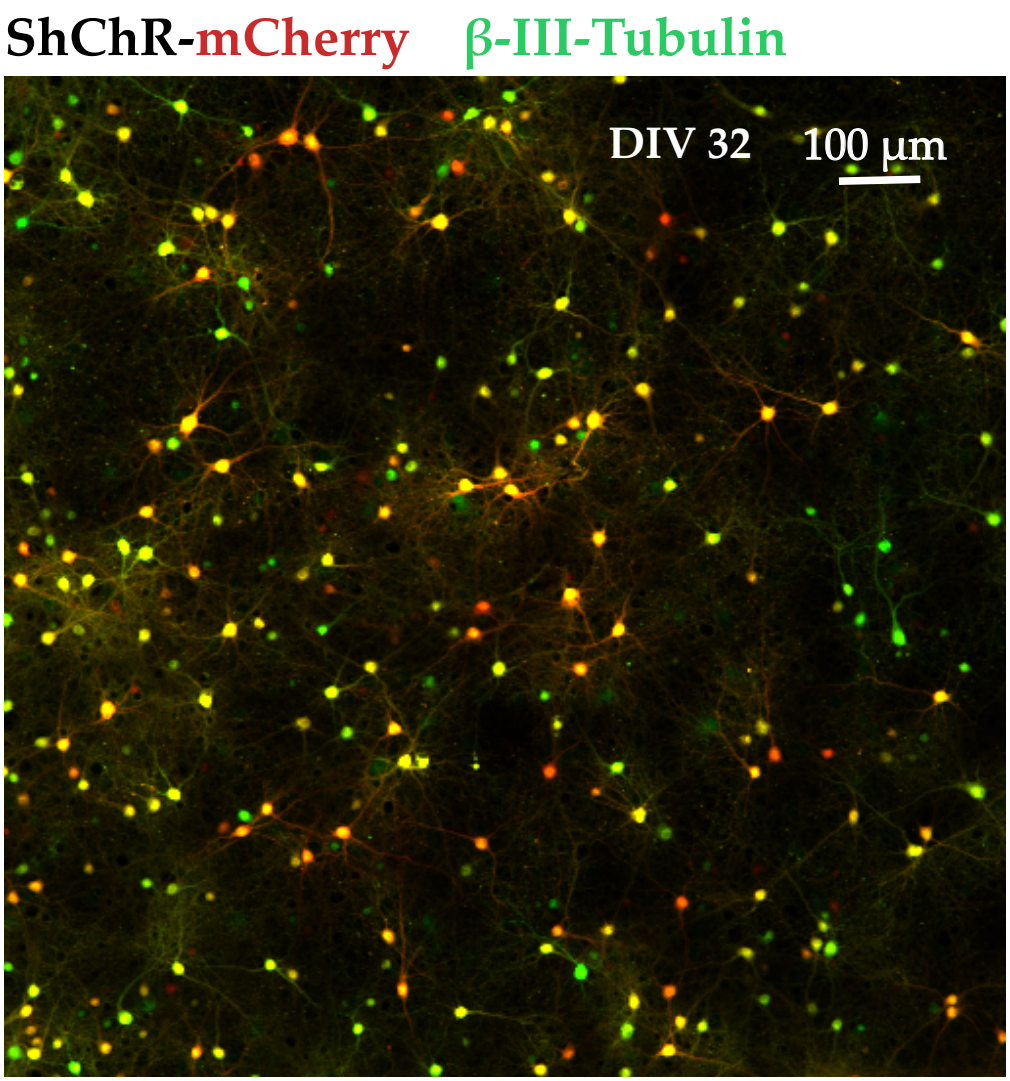

Figure 4.1. Fluorescence image of targeted putative glutamatergic neurons. The image displayed depicts fluorescence captured by a confocal microscope at 20x magnification. β-III-Tubulin staining appears in green, while putative glutamatergic neurons are visible in yellow due to the expression of ShChR-mCherry. Cell count indicates approximately 2% transfection efficiency.

Targeting GABAergic neurons

Regarding the GABAergic neuron, expression under both Dlx promoters was observed to be successful, albeit with a delay of 2 weeks post-infection, but this approach did

not prove to be optimal for our experimental requirements. Consequently, we have been working on implementing the use of mGAD65, which has shown promise for our purposes, and this work is discussed briefly in the future work section.

Targeting putative glutamatergic cells

Fig. 4.3 depicts the key features of our experimental paradigm. It enabled us to simultaneously record and stimulate multiple neurons over prolonged periods of time, probing individual neuronal responses independently. We employ the ShCh (Chronos) Channel-Rhodopsin under the CaMKII promotor (i.e. putative glutamatergic cells), which boasts rapid kinetics and reduced desensitisation periods (Klapoetke et al., 2014; Mager et al., 2018). These features enable reliable and stable performance over repeated stimuli, while minimising potential side effects and confounding factors. We show that the technique of synaptic isolation of individual neurons for continuous stimulation can be adapted to our system. Here, we utilise wide-field light pulses to activate potential glutamatergic neurons (as depicted in Fig. 4.4 and Fig. 4.5) simultaneously.

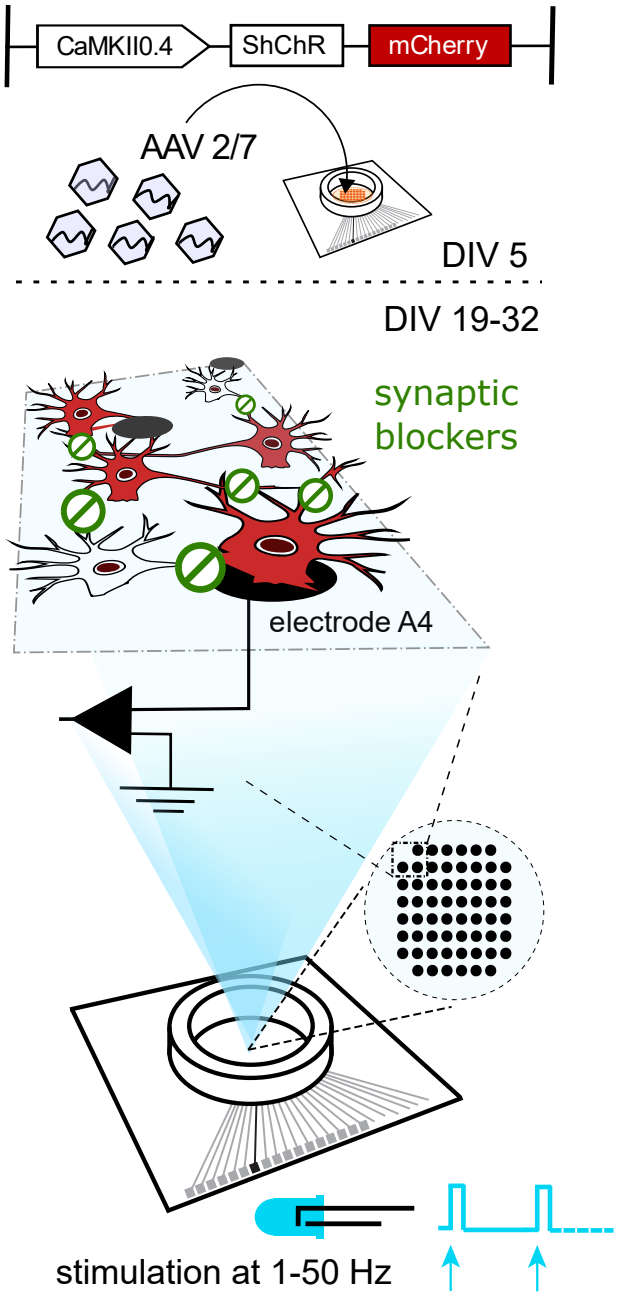

Figure 4.2. Microelectrode array recording with photostimulation. This figure shows the experimental paradigm employed of Optogenetics coupled with *ex vivo* developing neuronal networks on MEA.

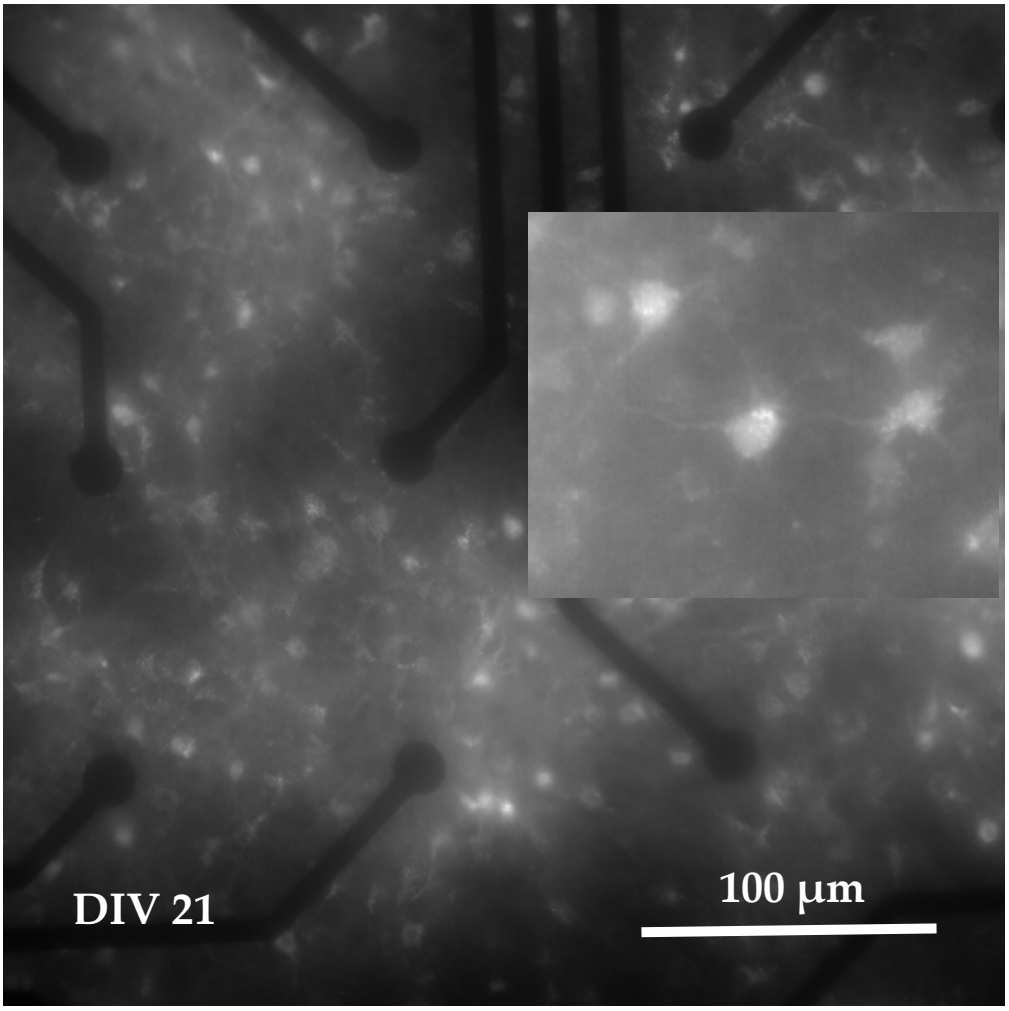

Figure 4.3. ShChR-mCherry expression. Fluorescence microscopic image of primary neuronal culture at DIV21 on a MEA120 transduced with AAV encoding ShR-ChannelRhodopsin fused to a red fluorescent protein (ShChR-mCherry). B: Image taken using a 40× objective and 488 nm excitation light to visualise ShChR-mCherry expression. The inset show an enlargement of a section for visualisation of the expression throughout the cell membrane, mainly in the soma, and less along the neurites.

4.1.1. Stable recordings of photoactivated neurons

In Fig. 4.4, we demonstrate our methodology (detailed in Chp. 3). Cells are developing *ex vivo* on a MEA into large random networks, infected by AAV2/7 viral particles at 5

div (Fig. 4.4A). The latter process results in the expression of photosensitive ion channels ShChR (Chronos) along the entire cellular membrane (dendritic, somatic and axonal) in a subpopulation which is known to exclusively code the CaMKIIα promoter i.e., putative glutamatergic cells (Fig. 4.4B). Only these cells are sensitive to the wide-field light pulses, such that the ShChR channels open upon stimulation (Saran et al., 2018). The rise of photocurrents follows extremely fast kinetics described in (Klapoetke et al., 2014).The membrane begins to depolarise due to an influx of cations *via* the light-gated passive cation conductance of ShChR, similar to the mechanism of the synaptically evoked spike (Häusser, 2000).

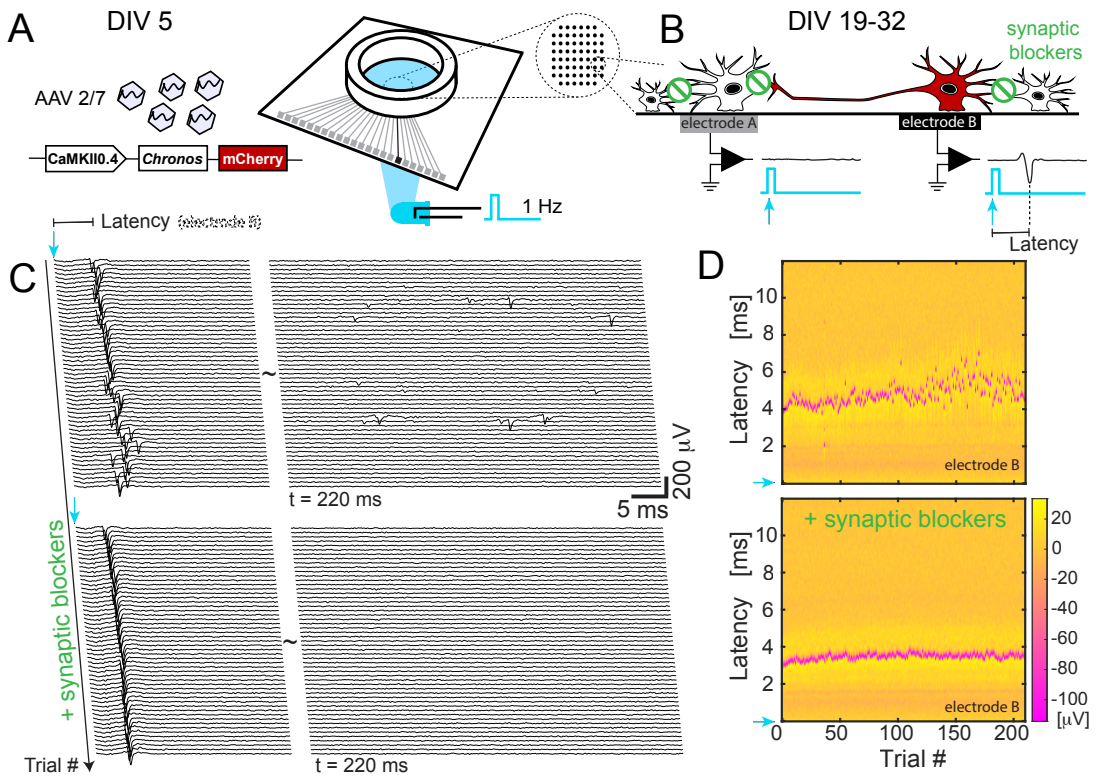

Figure 4.4. Simultaneous photostimulation and recording of single cells over lengthy timescales. **A:** The method involves the application of viral particles to the microelectrode array (MEA) using a serotype AAV2/7, which contains the CaMKIIα promoter for heterologous expression of the ShChR and mCherry transgenes. Experiments are performed between 19 and 32 div, and the initiating protocol is always a photostimulation at 1 Hz for 5 minutes. Supra-threshold pulses with a duration of 1 ms and intensity of 2 mW/mm^2 are then applied in a wide-field manner at the bottom of the MEA, uniformly reaching the electrode area. **B:** Description at the level of the extracellular space (<50μm) around a single electrode. Upon stimulation, only a subpopulation of putative glutamatergic neurons (illustrated in red) undergo direct activation. **C:** Pharmacological blocking of synaptic connections. **D-G:** Example of a single channel recording for establishing a response baseline at a stimulation rate of 1Hz for 5min. '+ SB', blocked synapses; and '- SB', without blockage of synapses. **D:** Recorded activity of all directly and synaptically activated nearby neurons. **E:** Recorded activity of only the directly activated neurons, post synaptic blockers application. F: Enlargement of the direct jittered responses from E (latency = 3.2 $\pm$ 0.83 ms). **G:** Enlargement of the direct responses from F where latency values adopt a narrow range (2.3 $\pm$ 0.05ms).

We study the contribution of intrinsic excitability to spike generation over long periods of time. In order to control cell activation independently of the extrinsic excitability component from the network, we follow the approach by (Gal et al., 2010), similarly pharmacologically blocking synaptic transmission but eliciting neuronal responses by brief photo-stimuli instead of extracellular electrical stimuli (see Fig.1, Gal et al., 2010). We represent the activity recorded at a single electrode, comparing neuronal responses to a sequence of pulses at 1 Hz before and after the application of synaptic receptors blockers (SB). In the former case (Fig. 4.4C, top section), the electrode detects an early component of post-stimulus spike responses from a glutamatergic cell, and a late component which is synaptically mediated (latency $\leq$20 ms), hence characterised by reverberating bursts with highly variable latency (Marom and Shahaf, 2002; Wagenaar et al., 2004). After SB application, the neuron's basal excitability remains quiescent for approximately 15-30 minutes after the cessation of synaptic communication between neighbouring neurons, hence, there is a complete absence of the late component (Fig. 4.4C, bottom section). Furthermore, a substantial difference is apparent in the jitters of the direct responses between the two conditions (Fig. 4.4D). Both the waveform and the latency of the directly evoked responses are precise in the presence of SB (Fig. 4.4D, bottom section), suggesting that spike initiation is influenced only negligibly by external, highly variable synaptic transmission of coupled cells that may ensue few milliseconds after stimulation (Jimbo et al., 2000; Wagenaar et al., 2004).

In Fig. 4.5 we show the subtle changes in temporal development of the spike waveform of a unitary neuronal activity and its dependence on the excitability. A glutamatergic cell isolated at an electrode is photoactivated at a constant rate of 1 Hz and 20 Hz. The resulting spike waveforms are sorted using the SPC method, where we fix the cluster density parameter i.e., the "temperature" following (Chaure et al., 2018). The temporal development of the respective latency is shown as a function of time.

4.1.2. Stability of the spike waveform over extended timescales

Spikes evoked at a stimulation rate of 1 Hz show low variability in both waveform and latency (Fig. 4.5A; grey). In response to a higher frequency of stimulation (20 Hz), SPC falsely sorts the waveforms into three clusters, here included as insets (see Methods for further details). We observe an increase in latency, together with a decrease in spike amplitude and bending of the *global-minimum-to-local-maximum* slope which is equivalent to a depolarisation slope as registered by an intracellular electrode (Henze et al., 2000). After an initial step-wise increase in the latency (dark magenta), the neuronal activity reaches a firing rate plateau (orange) where both the latency and amplitude fluctuate around their mean values. Long uninterrupted response activity may undergo abrupt joint change in latency and waveform, characterised by further flattening of the spike response (light magenta), which is restored back to the stable response activity regime (orange).

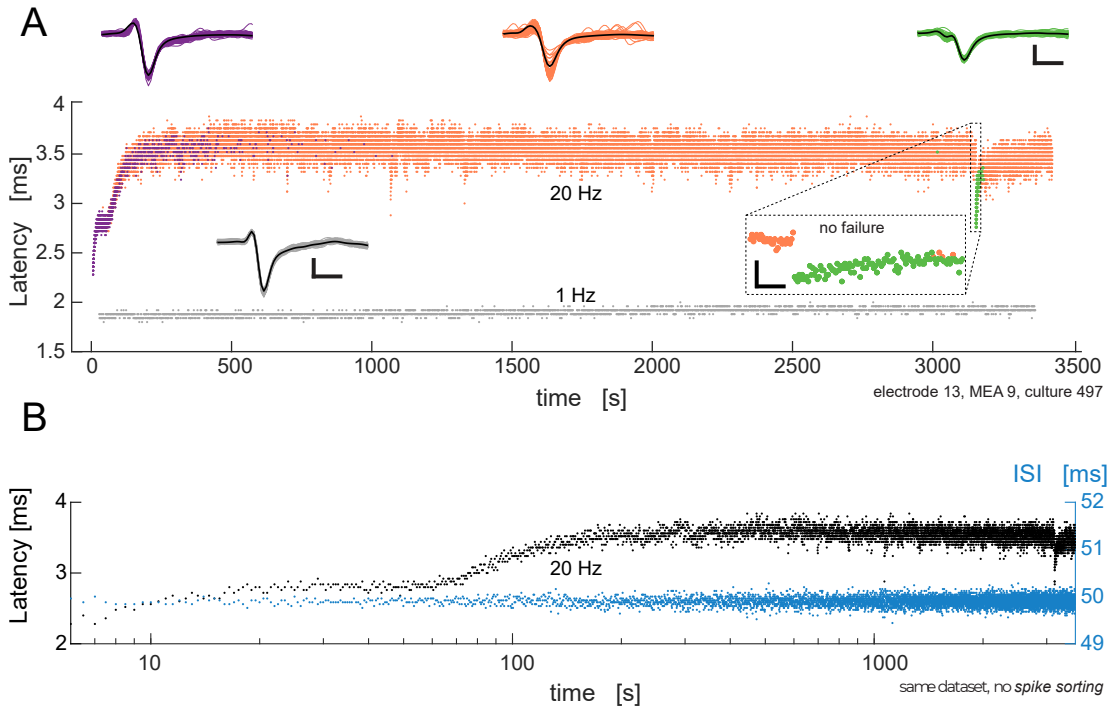

Figure 4.5. Evaluation of spike shape fidelity on a sample neuron activity under two 1 h-long uniform stimulation rates. **A**: he process of spike sorting involves analysing the entire length of each voltage trace. The resulting sorted waveforms are displayed as insets, with each waveform assigned a specific colour based on its corresponding latency as shown in the graph below. The vertical calibration for the graph is 50 μ V. All sorted waveforms are shown as insets, colour-coded as their corresponding latency in the graph bellow. Vertical calibration is 50 μ V. *Upper left*: At a low stimulation frequency (1Hz), all spikes (grey, 3346 spikes, 1 spike/s) are automatically sorted as a single neuronal unit; spike amplitude is 118$\pm$2μV, with a latency of 1.70 $\pm$ 0.08ms. *Upper middle*: When the neuron is activated at a high stimulation regime (20 Hz), spike shape fidelity is affected; spike amplitude drops to 67 $\pm$ 11μV, as the latency increases to 3.5 $\pm$ 0.5ms. Upon application of the SPC algorithm (see Chp. 3), three groups of spikes are separated, then attributed to different phases in the latency development: transient (violet, 2720 spikes), stable (orange, 69079 spikes), and shift (pink, 171 spikes) neuronal responses. *Upper right*: There is an abrupt change (orange to pink) in both waveform and latency, without a change in spike count. **B**: Latency development (black) at 20 Hz stimulation on a logarithmic horizontal timescale. Three-step transient phase with two transitional and an intermittent steady phase. A total of 62393 ISI (blue) are attributed to the *plateau* of the spike train (3113.5 s); mean ISI is equal to the mode value of 50 ms. There is a downward drift in latency with time, suggesting that a steady phase is reached and maintained for an extended period of time, instead of an expected intermittency response.

Fig. 4.5B shows the same unitary neuronal activity as Fig. 4.5A (20 Hz) but on a logarithmic scale. This specific neuron reliably responds to all delivered stimuli. A transient phase and an intermittent phase exist, as previously observed in electrically (Gal et al., 2010) and synaptically (Reinartz et al., 2014) activated neurons. In our case, intricate transients and extra complexity is revealed in the long-term photoactivated glutamatergic single cells.

4.2. Rich and heterogeneous features in glutamatergic neurons excitability

We further analyse the phases of excitability by alternating the stimulation rate between a baseline (1 Hz) and two higher repetition rates (20 Hz and 40 Hz) as shown in Fig. 4.6A. At 1 pulse per second, the evoked responses are reliable (i.e., with a probability of 1) and precise (i.e., with a low variability of the latency). Upon switching to a regime of 20 Hz, we observe a *U-shaped* transient phase. For this particular neuron, the reliable responses of the transient phase in the 20 Hz regime are followed by a chain of failures; whereas a switch in stimulation rate from 1 to 40 pulses per second pushes the excitability faster through a U-shaped transient phase and into a chaotic state, where both the latency and spike probability fluctuate around their mean values. Analogously to the 20 Hz regime, we observe continuous failures towards the end of the stimulation block. This process is reversible and a switch to baseline from both 20 Hz and 40 Hz produces the same behaviour of gradual recovery. We observe very pronounced U-shaped transient phases in about half of the analysed glutamatergic neurons. These temporal structures stretch over hundreds of seconds as a function of stimulation rate. The other half of neurons exhibit these structures less pronounced or have a more similar behaviour to the neuron observed as in Fig.3A adapted from Gal et al. (2010).

Fig. 4.6B depicts distinct patterns exhibited by a specific neuron when subjected to brief random blocks of photostimulation with rates ranging from 1 to 50 Hz, with adequate recovery periods between blocks. In is evident that the time needed for the onset of intermittency decreases with rising stimulation rates akin to the trend observed in Fig.3A of (Gal et al., 2010). Furthermore, the transients of the latency also decrease with increasing stimulation frequency (Fig. 4.6B; black to green).

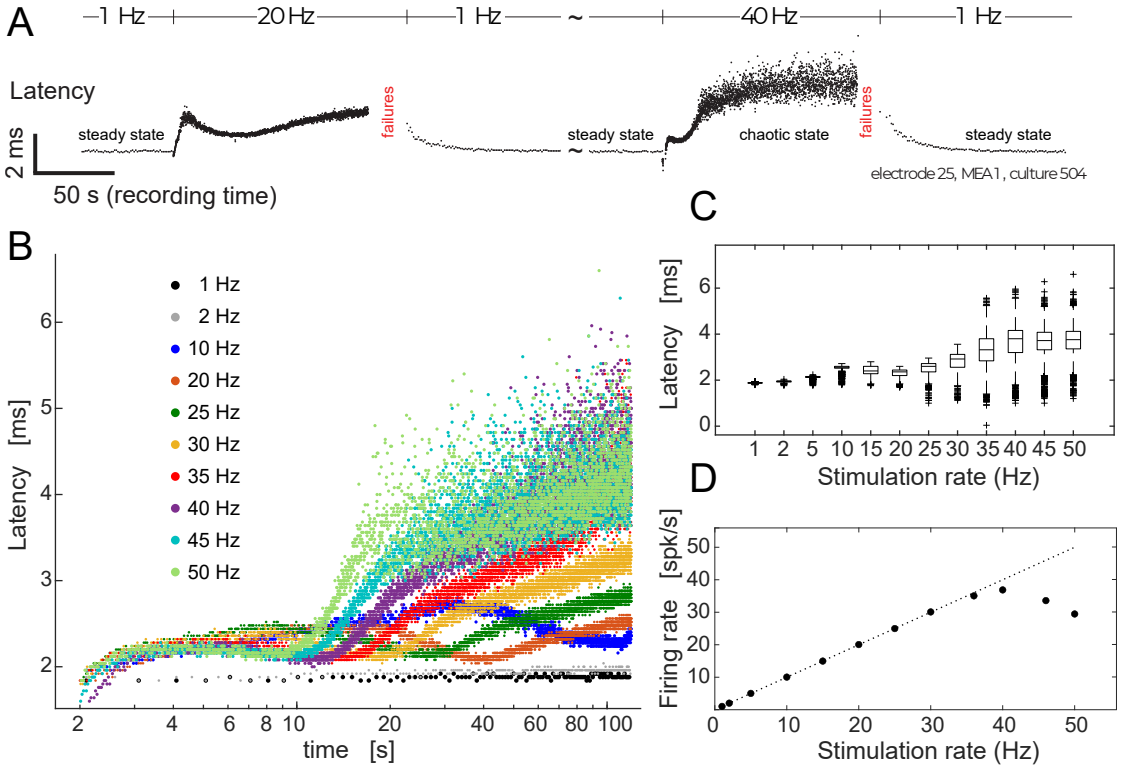

Figure 4.6. **A**: Stimulation frequencies are alternated without breaks with the following pattern: 5 minutes at 1 Hz, 2 minutes at 20 Hz, 5 minutes at 1 Hz, 2 minutes at 40 Hz, and 5 minutes at 1 Hz. **B**: A neuron is stimulated with rates of 1, 2, 10, 20, 25, 30, 35, 40, 45, and 50 Hz. Stimulation is presented randomly in 2-minute blocks with 5-minute intervals between them. The latency of the spike is plotted against the time since the block began, with each colour representing a different stimulation rate. A higher stimulation rate results in a faster onset of intermittency and as well as in the the two-step transient rise. **C**: The latency for each block is shown as a box-plot with the mean and standard deviation for each stimulation rate. **D**: The mean spike rate is estimated for each block with respect to the stimulation rate.

Likewise, the variability of latency increases (as shown in Fig. 4.6C). Fig. 4.6D illustrates a critical stimulation frequency that separates the steady and intermittent phases. In this specific neuron, there is a sharp transition in the output rate at ~35Hz. During the intermittent phase, the mean latency remains constant (Fig. 4.6C). Additionally, the linear relationship between firing rate and stimulation rate breaks down at the onset of intermittency. After analysing neuronal traces from 100 MEA, we conclude that a transient phase is followed by either a steady phase - characterised by variable latency but dependable response dynamics - or an intermittent phase that exhibits both periodic and chaotic states, features specific response patterns, transition modes between response patterns, and rate modulations.

4.2.1. "Classes" of glutamatergic responses are on a continuum

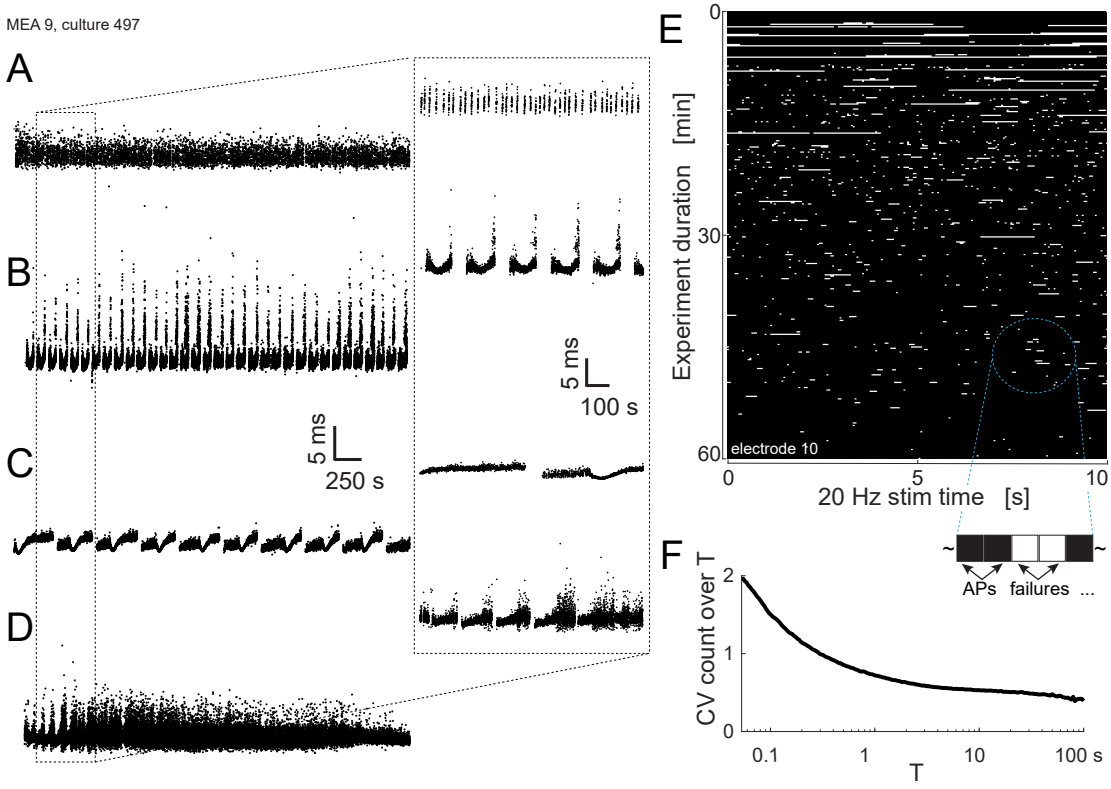

Figure 4.7. A-D: Shown is the intermittent phase of four neurons under a stimulation rate of 20 Hz. Neurons are simultaneously activated with the neuron shown in Fig. 4.1.2B-C. The left panels show the entire response to a 1-hour stimulation block, while the right panels show an enlargement of segments used to identify specific patterns. Neurons **A-C** exhibit bursting-like behaviour where spikes are clustered together in an ordered manner with typical cluster size and inter-cluster intervals. Both **B** and **C** show oscillating 'U-shaped" structures throughout, with patterns from A present at the beginning of each "U-shape" structure in **C**. Additionally, A exhibits a "vertical stripes" pattern at varying timescales, which also appears in **B** and **C**. Neuron **D** responds with irregularly sized and spaced patterns of spikes and clusters of spikes, as shown in the binary response sequence in E, with white pixels representing failures and black pixels representing spikes. The length of the horizontal sequences in **E** is 10 s, counted left to right and top to bottom of the panel. **F:** CV of the bin counts as function of bin size for the neuron in E.

We initially investigate the intermittent phase during a high-rate long-stimulation regime of 1 hour at 20 Hz, as shown in Fig. 4.7. We present four response patterns of differ-

ent neurons activated and recorded simultaneously with the regular spiking neuron mentioned in Fig. 4.5B-C. Previous studies have classified irregular spiking, bursting, and stuttering as hallmarks of interneurons, while regular spiking is characteristic of glutamatergic pyramidal cells, using standard intracellular stimulation regimes Fig. 2.1 from Markram et al. (2004). Similarly, Gal et al. have described stable, irregular, regular-clustered, and irregular-clustered response classes Fig. 2.2. Notably, they use extracellular electrical pulse stimulation paradigm over very long times. Baltz and Voigt report a 60:40 ratio of two response types, with stable responses favoured over clustered responses (Baltz and Voigt, 2015). Interestingly, we observe all of these prototypical behaviours in the evoked responses of glutamatergic neurons. Figures 4.7A-C show bursting-like neurons with oscillatory and repetitive activity patterns, with a latency that occasionally jumps between two levels, and in some cases, U-structures emerge in a repetitive manner throughout the experiment, similarly to the ones observed in transient phases Fig. 4.6A-B, which is further examined computationally (Sec. 4.3). The spikes appear to be organised into clusters with typical cluster size and inter-cluster intervals. The responses in Fig. 4.7D form complex patterns including clusters, individual spikes, and failures, with irregular cluster sizes and intervals. We observe the development of neuronal excitability through quasi-stable pattern modes on this intermediate timescale, compared to Fig. 2.2 from (Gal et al., 2010). Gradual transitions occur from periodicity to chaos or irregular spiking and finally to regular and stable spiking, with only few systemic failures, as shown in Fig. 4.7E.

Nevertheless, we find the firing rate dynamics of this neuron to indicate towards long correlations. This is demonstrated by plotting the coefficient of variation CV of the spike count as a function of a logarithmically-increasing time window T. Namely, after an initial sharper decrease, the rate practically plateaus at ~0.5 over increasingly larger values of T (Fig. 4.7F). The variance of the counted number of spikes reflects a variability

stretched on a slow timescale over seconds, minutes, and hours. We further examine the statistics in Sec. 4.2.2.

4.2.2. Statistics of the intermittent phase

Upon extraction of the excitability features, we sort spike events recorded at individual electrodes into separate neuronal units (Sec. 3.3). With regard to the type of process underlying timescale-invariant behaviour, we looked at the interval and count statistics, which are fundamentally related on theoretical grounds (Nawrot, 2010). As explained by Lowen and Teich, a dynamical process can be said to "scale" with the temporal resolution employed, if fluctuations in the number of events on a short timescale are proportional i.e., statistically self-similar to those measured on longer timescales: scale invariant in occurrence. Mathematically, this will lead to power-law dependencies in the scaled quantities and the "long tail" of the resulting power-law function can be fitted as a straight line on a doubly logarithmic graph. We constructed sequences of counts (Chp. 3, Fig. 3.2).

Above a certain critical stimulation rate, the neuron exhibits scale-free dynamics with power-law statistics, indicating consistent macroscopic properties of the evoked spike trains across various stimulation regimes. Our research builds upon prior studies on rat cortical neurons and specifically focuses on a sub-population of excitatory cells that are photoactivated. Using the Allan factor and Fano factor methods shown in Fig. 4.8, we analysed point processes generated by responses to stimulation rates ranging from 20-50 Hz during intermittent phases lasting up to 12 hours. At the outset, F(T) and A(T) values were around 1, suggesting a low probability of success in a Bernoulli process where zero spikes counted for window sizes smaller than the shortest ISI. However, both F(T) and A(T) curves subsequently dipped below 1, with a more pronounced dip observed in

the Allan factor curve, indicating synchronised cell responses to the 20 Hz rhythmic stimulation. The initial spiking activity's quasi-stable mode exhibited an oscillatory bursting component that caused the peak at ~30 s. A power-law in the Fano factor curve emerged near a window size of ~0.05 s, while the Allan factor curve shifted near 2 s. The power-law in the Fano factor curve spanned four time scales, while that in the Allan factor curve exceeded four decades, with the scaling exponent of the power-law in the Fano factor curve approaching its theoretical maximum ($\alpha = 0.98$) and the Allan α significantly higher ($\alpha = 1.45$), indicating that the spike train is fBm-based.

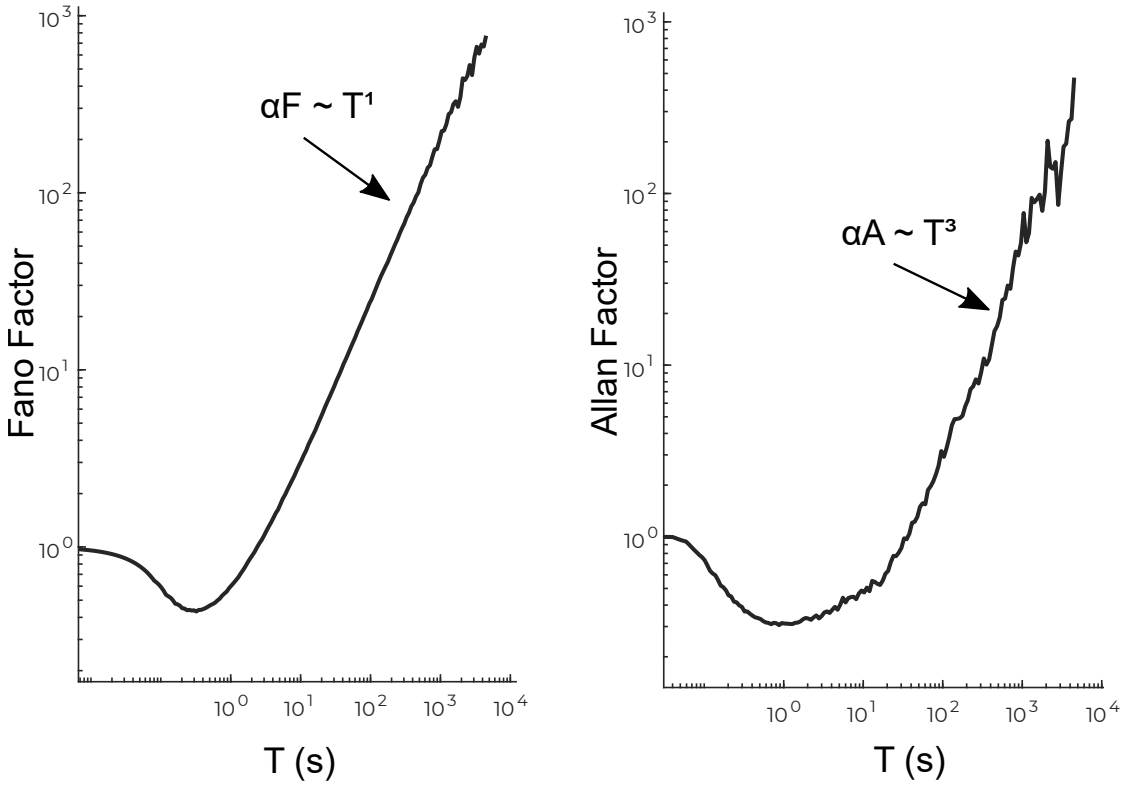

Figure 4.8. Methods for Estimating Scaling Exponent: Fano and Allan Factors. A: By scaling with T^1, the Fano factor shows a maximum possible value of $\alpha = 1$. **B:** On the other hand, scaling with T^3, the Allan factor can reach a maximum value of $\alpha = 3$.

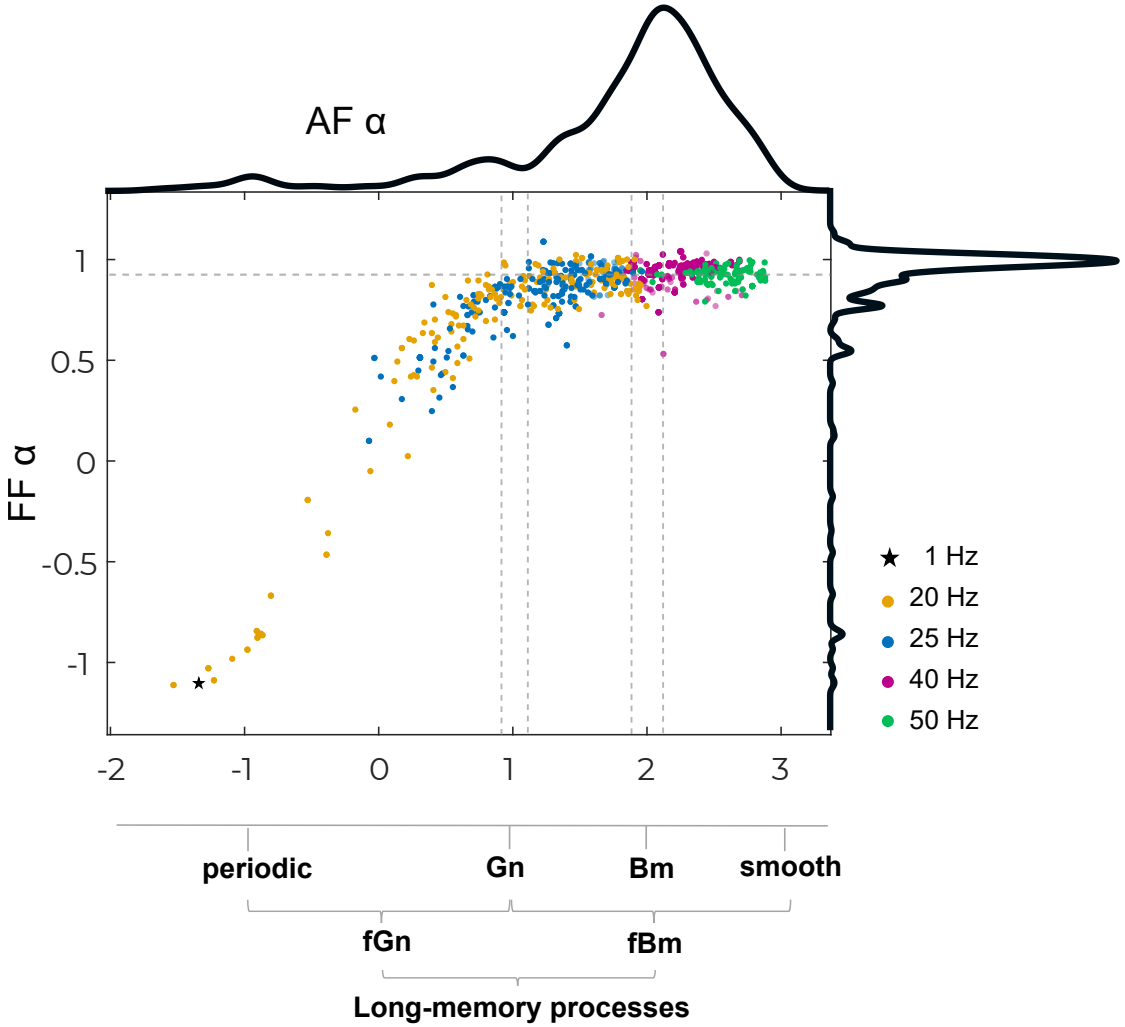

Figure 4.9. Variation of scaling exponent α values with frequency. This plot shows the variation of both α values for various stimulation frequencies (colour coded) estimated by the Fano factor and the Allan factor methods. The plot marks in the central panel indicate individual measurements of single cells. The histograms at the upper and right border show the histogram of the marginal distribution. Underneath, we provide a classification scheme of the Allan α values and the corresponding stochastic process.

Figure 4.9 illustrates the distribution of scaling exponents for various bin sizes, capturing the power-law relationship observed in Fano and Allan factor curves from 1200 individual neuronal units. The majority of processes underlying neurons responding to all frequencies are within the fractal Brownian motion (fBm) realm, with most clus-

tering between α= 2 and 2.5. Fractal-based point processes belonging to the fBm class exhibit statistically self-similar behaviours, indicating long-range correlations across the data points. Despite power-law distributed intervals being capable of producing scale-invariant behaviour as a fractal renewal process, in this instance, the fBm implies that intervals are not independently identically distributed. However, α= 2.0 represents a such a unique case of fBm, which entails Brownian motion or random walk with no long-range correlations, a "dummy" dataset was created by shuffling the ISI to compare each spike train with the same number and frequency of ISI present in the investigated neuronal spike train. The power-law in the Fano and Allan factor curves for 20 surrogates was flattened (results are not depicted in the graphs). We used the highest standard deviation documented by Thurner et al. as an approximate value for a signal with a known α = 1.5, in order to establish an interval of 1.87–2.13 around the anticipated occurrence of these unique cases. The spike number fluctuations exposed long-range correlations, indicating that there were unclassified cases within the original point process bracketed by the dashed vertical lines in Figure 4.9. A substantial fraction of spike trains could be distinguished as stochastic processes based on fBm. The Allan values calculated for varying stimulation rates were comparable and exhibited a positive correlation.

The collected data often display bias and significant deviations from theoretically derived exponents, which are estimated through various methods. This phenomenon is primarily caused by default lower and upper cutoffs in measurements that lead to information loss due to point process generation and limited experimental time. However, in our particular situation, we are able to observe a range of scaling exponent values for spike trains that are derived from different stimulation rates. This range falls within the scope of long-memory processes. In the case of Fano factor curves, the power-law extends beyond four timescales. As a result, fluctuations in spike probability and latency over

time can be confidently attributed to long-range correlated fractional Brownian motion processes.

4.3. Mathematical models of intrinsic excitability

In our quest to emulate the long-term dynamics of cell excitability, we scrutinise models of various degrees of intricacy. Initially, we opt for a validated reduced model, centred on conductances, which we subject to stochastic perturbations to accommodate the intrinsic uncertainty of ion channel kinetics. Subsequently, we advance our inquiry from a single compartment model, denoting a point neuron, to a more complex multi-compartmental model incorporating both soma and axon geometry. Our ambition is to furnish a comprehensive investigation, and hence we undertake an *in silico* experiment employing a layer five pyramidal neuron template from the Blue Brain project.

By leveraging the work from (Gal et al., 2010) alongside our own experimental observations, we endeavour to replicate the results using two stimulation techniques: classical current injection and Optogenetics. With regard to the stimulation design, following the stimulation methodology introduced by Soudry and Meir, we employ a train of stimuli to mimic the stimulation patterns employed in the aforementioned experiments. In general, this is a straightforward yet efficacious stimulation protocol enables us to deduce analytical input-output mappings of neuronal responses.

Wang-Buzsáki-Güler stochastic model

The response pattern of a neuron to the onset of a stimulation block may depend on the stimulation rate but remains consistent across repetitions with the same rate. Such behaviour was previously modelled using the Hodgkin-Huxley model with slow sodium

inactivation and potassium inactivation model with varying values of the current conductance g_M (Soudry and Meir, 2012), albeit with limited success. We implemented the Wang-Buzsáki-Güler stochastic model to investigate quasi-stable pattern modes in the intermittent phase (Fig. 2.4) and ourselves (Fig. 4.7). We followed the suggestion of applying different durations of the input rectangular pulse train at different stimulation rates. According to Güler, non-trivial cross-correlation persistence effects greatly influence excitability, spontaneous firing, and spike coherence, and the developed model accurately captures these functional correspondences.

Our findings demonstrate that with increase in stimulation frequency, as shown in the scenario in Fig. 4.10, the intermittent mode undergoes a behavioural transformation from highly reliable to somewhat erratic behaviour close to the critical point, ultimately resulting in failures and intermittency due to low excitability. These results qualitatively emulate several experimental discoveries as presented in Fig. 2.4, especially the formation of the transient phase. However, it is crucial to note that the intermittent phase statistics do not exhibit the scale-free correlations observed in the spiking behaviour of biological neurons.

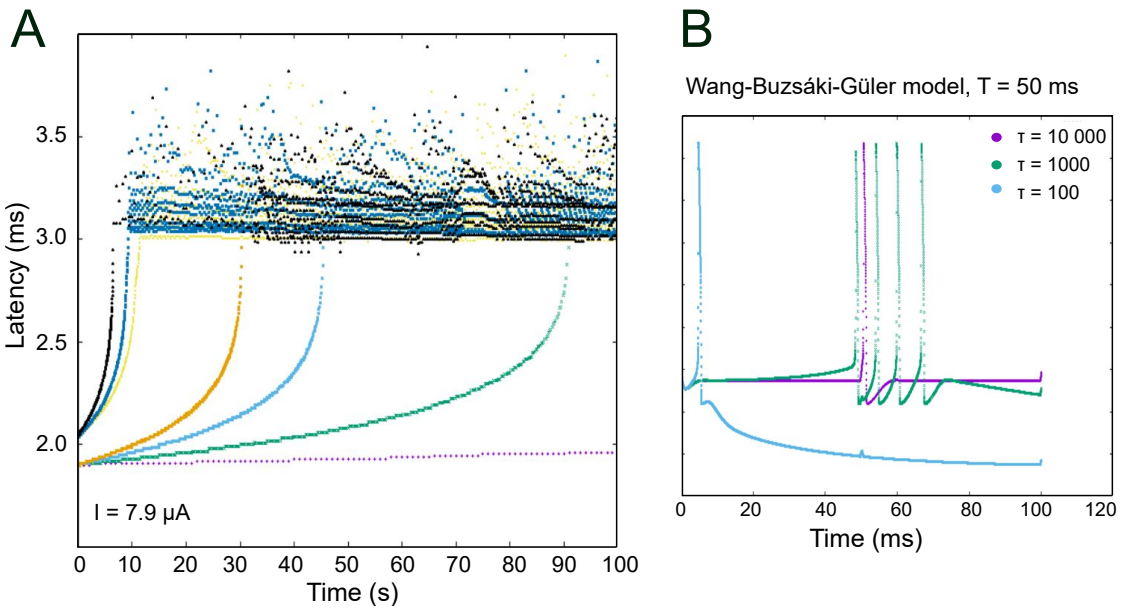

Figure 4.10. Latency versus time in the Wang-Buzsáki-Güler model. A: This figure shows the latency versus time for various stimulation frequencies as generated by the Wang-Buzsáki-Güler model and **B:** shows the tuning of the correlation time τ.

Wang-Buzsáki-Güler model realisation in soma morphology

We proceeded with implementing the stochastic model we devised by utilising the soma's morphological traits. Initially, we applied electrical stimulation to the soma and meticulously recorded the corresponding reactions.

When the input stimuli frequency is sufficiently low, the soma remains stable. Nevertheless, with an increase in stimulation rate, the neuron transitions swiftly from a temporary to an intermittent phase (Fig. 4.10). The neuron's response is reliant on its morphological features. To ensure consistent voltage dynamics, the diameter and length must double while the current input should be halved. Alterations in R_a do not seem to considerably impact the membrane potential behaviour, possibly due to a limited range of variation.

Wang-Buzsáki-Güler model realisation in soma morphology with optogenetics

We extend the investigation of the long-term dynamics of the single neuron to the case of photostimulation of an existing model of ChannelRhodopsin-2 (ChR2). Williams et al. demonstrate that the process of recovery from inactivation (τ_R) is dependent on both voltage and light power, however, we observed that more positive voltages significantly slow down the recovery, while higher light power has a mild speeding effect on the recovery from inactivation.

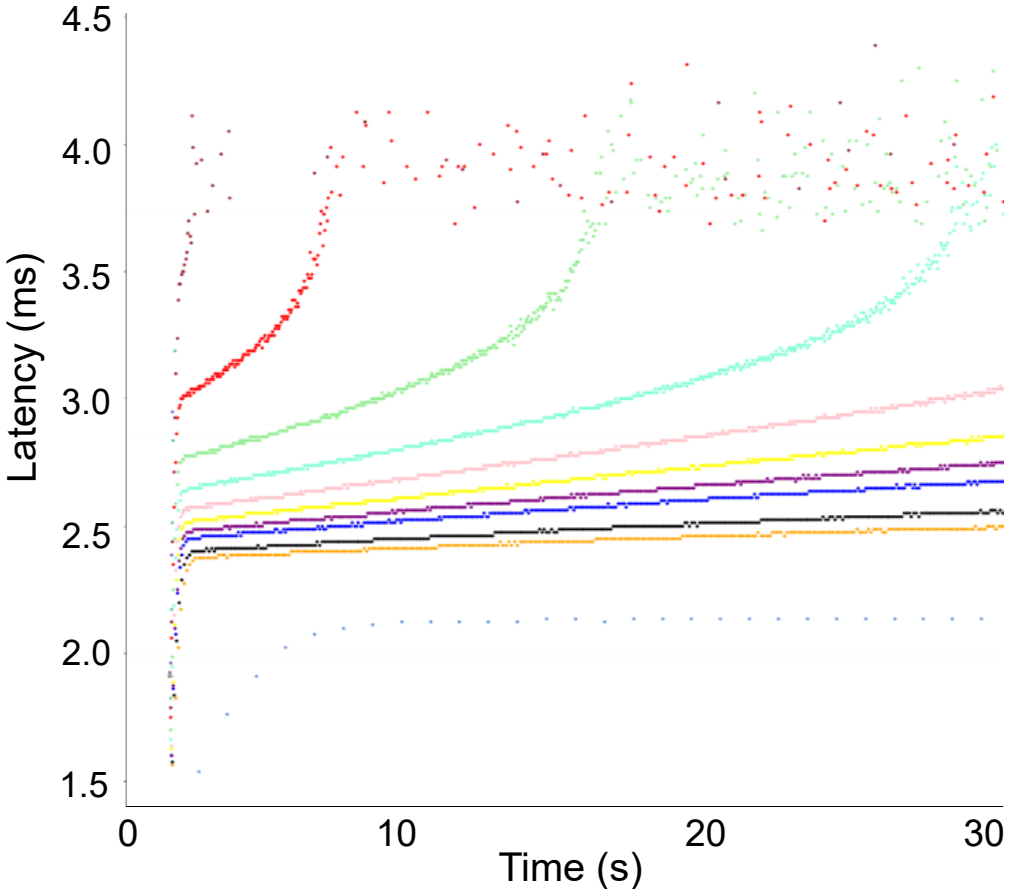

Figure 4.11. Optogenetics stimulation implemented in the Wang-Buzsáki model. This figure shows the latency versus time for various stimulation frequencies as generated by the Wang-Buzsáki model implementing Optogenetics stimulation.

Fig. 4.11 illustrates that a transient initial phase occurs when a light stimulus is used during the initial seconds of the response, which is not observed using electric stimulation (when the ChR2 channel is inactive). Although this phase was not reported by Gal et al., we have observed and described the two-step transient phase in the responses of photoactivated glutamatergic cells in Fig. 4.6. The graph demonstrates that an "initial transient" phase develops into a stable phase, and eventually, the latency stabilises at a higher steady state or exhibits intermittency.

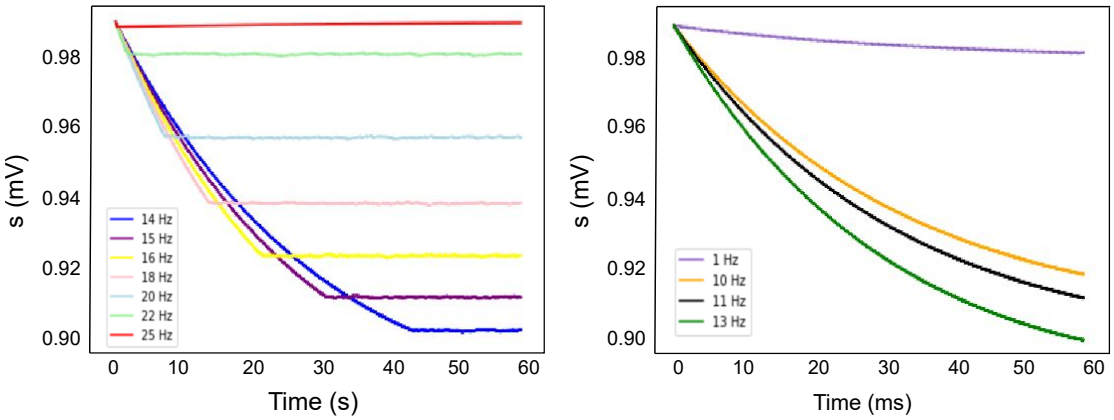

Figure 4.12. ChR2 dynamics in the slow gate. This figure shows the slow variable versus time for different stimulation frequencies. Higher stimulation frequencies are shown in the left, lower frequencies in the right panel.

Previous research on the prolonged dynamics of single-compartment electrical stimulation, as documented in studies Soudry and Meir from 2010 and 2014, has identified gates is as the cause of latency response. This is due to its manifestation of slow neuron kinetics. When studying the gate response to light stimuli, an opposing behaviour was observed in comparison to the electrical stimulation scenario at higher frequencies. The gate response reached a higher steady state value with increasing frequency, as depicted in Fig. 4.13A. However, at lower frequencies, where the initial intermittent phases slowed down and the latency behaviour aligned with the results of the Gal et al. experiment, the gate response exhibited a higher steady state value as the frequency

decreased, as shown in Fig. 4.13B. These findings are in line with those reported in Soudry and Meir (2010).

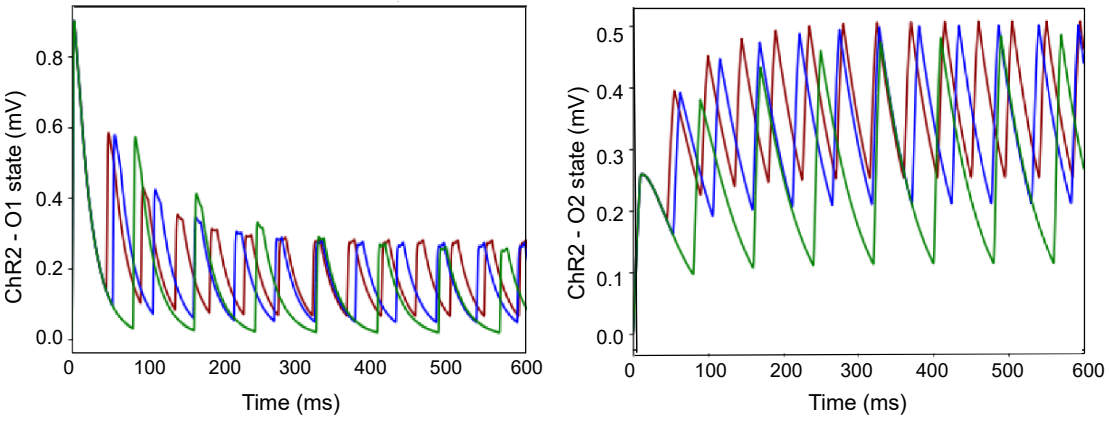

Figure 4.13. ChR2 dynamics in the open states: O1 and O2. This figure shows the dynamics of the ChR2 in the open states O1 and O2 for different stimulation frequencies with the same colour code as in Fig. 4.12.

Long-term ShChR Dynamics: experiment and model

Expanding upon the findings in biological neuronal transients and utilising insights gained from our ChR2-incorporating model, our study investigated the kinetics of the ShChR channelrhodopsin through experimentation.

The experiment involved examining the dynamics of ShChR within a frequency range of 2-40 Hz. To analyse ShChR, we patch-clamped an isolated HEK297 cell expressing ShChR-eGFP. The inward current peaks of ShChR were extracted and normalised using the initial and maximum current peak values. This was shown in a graph that plotted the number of photostimulation pulses against the normalised current peaks. Another graph displayed the same curves, but in relation to the continuous time of the experiment.

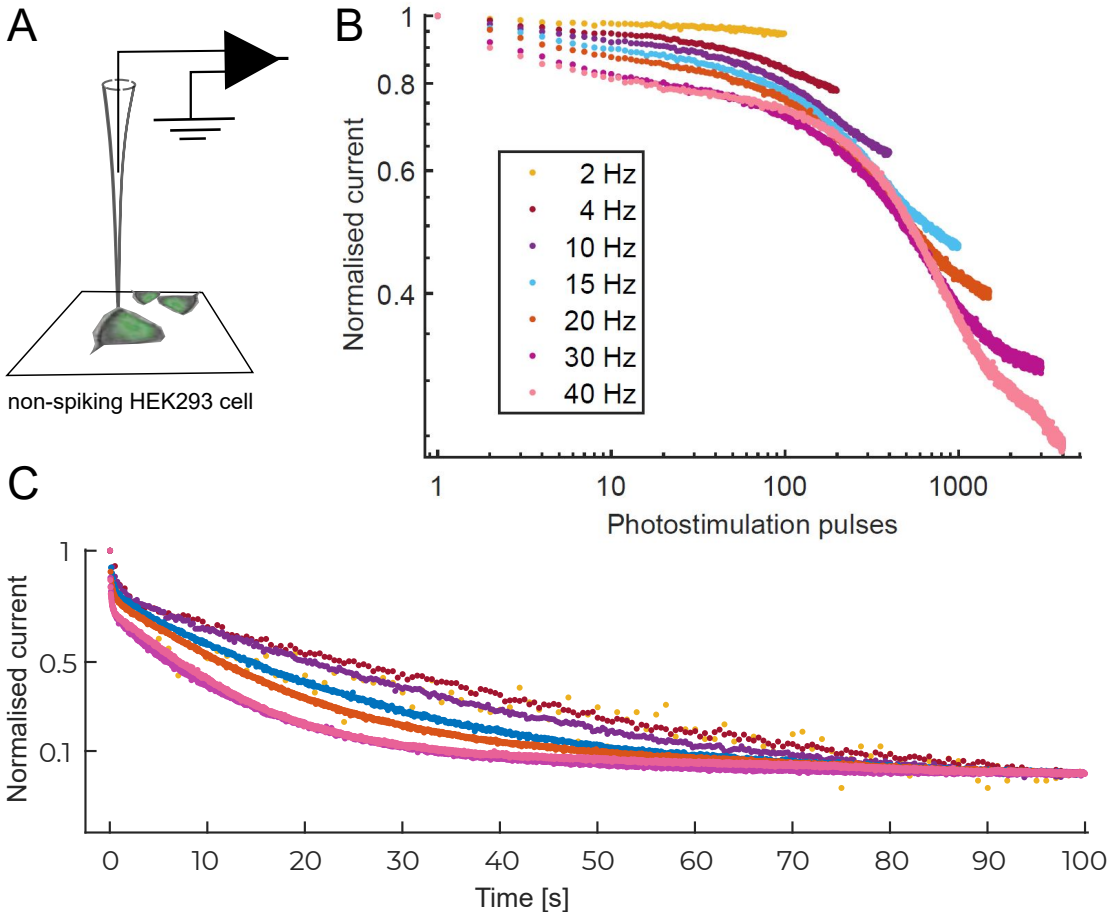

Figure 4.14. ShChR dynamics: experiment 2-40 Hz. A: Patch-clamp of an isolated HEK297 cell expressing ShChR-eGFP. **B:** The recorded ShChR inward current peaks are normalised by the first and maximal current peak. Shown are normalised current peaks versus the number of photostimulation pulses for stimulation frequencies from 2 to 40 Hz. **C:** The same curves as in B, presented versus continuous time of the experiment.

The analysis of ShChR dynamics over the long term involved extracting peak current values following each 1 ms stimulation pulse. These values were then plotted against the number of stimulation pulses in Fig. 4.14B and Fig. 4.15, and against continuous time in Fig. 4.14C. A log-log plot of the data indicates a power law relationship at the start of each stimulation, which later transforms into an exponential drop after about

100 stimulation pulses. Finally, after approximately 1000 stimulation pulses, the trend continues as a power law relationship.

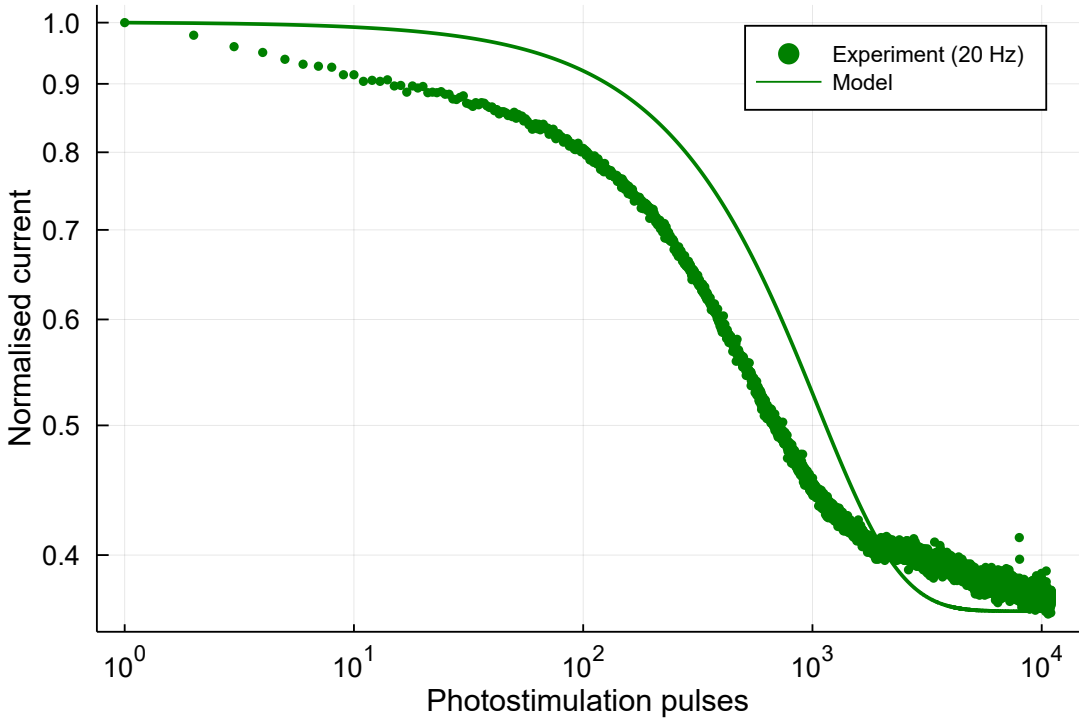

Figure 4.15. Long-term ShChR dynamics. This figure shows visual representation depicts the progression of the maximum ionic current over a long period of time and the relating optimised data points of the five-state Markov model.

5. Discussion and conclusion

In this chapter, we discuss the outcomes that have been put forth and deliberate upon the principal discoveries and their plausible meanings.

In context of the methodology, we attained dependable electrophysiological recordings of solitary neuron electrical reactions *via* non-invasive repeated photoactivation, which ensured the steadfastness of the spike waveforms at low and high stimulation rates. Additionally, we introduced a computational method to manage huge data files accumulated from every experiment and developed an algorithm to optimally classify individual neuronal units detected at each electrode.

During the neuronal data processing we encounter two critical challenges: distinguishing neuronal units, as well as detecting power-law relationships present in the data. The former entails the identification of individual neurons by analysing their extracellular imprints of excitability by use of spike sorting algorithms, while the latter involves graphical methods to identify dynamical processes with scale free correlations. In our endeavour to sort spikes from data, we initially relied on conventional algorithms in neuroscience. However, these methods fell short in accurately classifying highly variable spike waveforms, inevitably leading to significant statistical errors. To overcome this challenge, we have developed an algorithm that leverages extracellular imprints of excitability, such as spike time, latency, and amplitude, to sort the spikes. We must

analyse the spike data in a sequential manner, keeping in mind that following each stimulus a maximum of one response is expected from each neuron. Overall, our algorithm provides an effective approach for accurately and efficiently sorting spikes into clusters based on large datasets. Nonetheless, these difficulties present an opportunity for the development of novel and more efficient techniques by the machine learning community for organising spike data accumulated during ongoing stimulation protocols. Additionally, we took great care in our analysis in fitting power-laws[1] as straight lines on double logarithmic plots over at least three decades (Lowen and Teich, 2005; Lundstrom et al., 2008; Turcott and Teich, 1996). These plots necessitate vast amounts of data to deliver reliable estimates of the scaling exponents. Given that both conditions of effective neuronal units classification and the existence of power-law over three decades were satisfied in our case, we can confidently infer the nature of the underlying dynamical processes to be scale-free, indicating the absence of a characteristic timescale.

By utilising wide-field stimulation and combining it with spike sorting algorithms, we were able to detect and analyse the responses from a large number of neurons, which is a significant advancement from previous studies that only examined responses one neuron at a time, providing a novel and comprehensive set of observations. Furthermore, by utilising the genetically-specific, fast variant of ShChR, we could selectively activate only putative glutamatergic neurons, resulting in a more precise and regulated form of stimulation in comparison to conventional electrical methods. It is worth noting that glutamatergic neurons are known to demonstrate less inter-cell diversity than the GABAergic subpopulation shown in (Markram et al., 2004), which increases the uniformity of our sample and reinforces the significance of our discoveries within the broader framework of neuronal excitability. These classifications by Markram et al. are based on an experimental method designed to uncover the unique pattern-generating

[1] A power-law is inferred when the graph of a function is a straight line on a double logarithmic plot.

capabilities of a neuron, ultimately providing insights into its representative firing behaviour within a population of neurons i.e, larger neural network.

To begin with our findings, we can first contrasts them with the typical electrical activity seen on a brief timescale, as demonstrated in Fig. 2.1, using the prototypical model outlined in (Markram et al., 2004). It is clear that the firing patterns of glutamatergic neurons are not accurately characterised by the regular spiking behaviour suggested by Markram et al., as they exhibit much more complex electrical phenotypes. It was surprising to discover that glutamatergic cells have diverse and dynamic behaviours over extended periods (Fig. 4.7). The wide range of patterns exhibited by these cells has significant implications for neuroscience experiments, especially in the context of bottom-up paradigms. We thoroughly examined glutamatergic neurons for extended periods and conducted statistical assessments on over 2000 spike trains in these neurons. In this way, we confirm and expand upon previous findings, highlighting the importance of accurately characterising the responses of genetically identified neuron types. To accurately record neuron activity, longer datasets must be used, and new mathematical models are needed to explain the processing of information, learning, and memory in single neurons. Furthermore, the relationship between temporal dynamics and event frequency across intervals shows a long time dependence on past values. By assessing memory capacity compared to the realisations of fBm processes, we hypothesised the nature of the intrinsic mechanisms driving excitability at the level of action potentials i.e., single neuron level, especially over extended periods of time.

The differences in latency development in the *transient phase* (Fig. 4.6) compared to previous research by Gal et al. indicate the possibility of a connection between the kinetics of channelrhodopsin and the occurrence of spikes over extended time periods, from minutes to hours. This could suggest that the phenomenon is an artefact of the optogenetic tool or that channelrhodopsin has its own memory process that interacts

with neuronal excitability after repetitive activation. Our study started to investigate our version of ShChR (Chronos) as a tool for extended and varied activation frequencies. In addition, we created computational models for both short and long time intervals to supplement biological experiments and gain a more comprehensive understanding of ShChR excitability. However, further experimentation and collection of more data points are necessary to draw statistically conclusive hypotheses about these findings.

To delve deeper into the topic, it is crucial to modify conventional experimental models by considering the inherent excitability mechanisms (as discussed in Chp. 2), and devising stimulus patterns that mimic the synaptic inputs received by brain cells. Such adaptations have been developed and some have resulted in more accurate descriptions of the neuron's input-output dynamical properties on the action potential timescale (Sec. 2.2). In synaptically evoked action potentials, the activation of K_V channels lags behind that of Na_V channels. This is because the membrane depolarises due to cation influx through ligand-gated ion channels which activates Na_V channels, leading to a substantial influx of Na^+ ions into the cell. At the same time, K_V channels are also activated, but their slower kinetics mean that substantial outward K^+ flow typically occurs only after the Na_V channels are fully activated, causing membrane re-polarisation. In contrast, during external electrical stimulation, the change in extracellular potential is usually very brief, necessitating unphysiologically high pulse amplitudes to achieve a sufficiently large change in trans-membrane potential (Irnich, 1980).

In the case of optogenetics, it is important to consider multiple factors that can influence the membrane's response to a single supra-threshold light pulse, such as the properties of the optogenetic protein and the specifics of the light pulse. After each stimulus, the ShChR ion channels situated across the cell membrane open up simultaneously, which enables positively charged ions, especially sodium ions, to flow in. This can last for a mere millisecond (one stimulation pulse), and if the membrane potential surpasses the

activation threshold, voltage-gated ion channels quickly expose themselves, resulting in a surge of more sodium ions and swift depolarisation, eventually leading to the generation of an action potential. ShChR channels activate with fast kinetics and a robust response to variable light densities reaching the cell at different parts of the cell body, dendrites, and axon (Klapoetke et al., 2014). Nonetheless, the limited ability to control the number and localisation of expressed ShChR channels has implications that we further explore in an ongoing work. Furthermore, it is important to consider the fact that optogenetic stimulation is not a perfect mimic of natural synaptic inputs. Indeed, the activation of ShChR channels is not limited to synapses, but rather activates channels throughout the entire neuron, including the cell body, dendrites, and axon. This can lead to activation of neurons in a non-physiological manner, potentially influencing excitability in a particular way *in vivo* (**?**). In fact, the results of our study revealed the potential impact of the long-term dynamics of channelrhodopsins on the transient phase (Sec. 4.2), and the need to asses the consequences of the ubiquitous expression of channelrhodopsins along the full membrane morphology of cells.

Overall, our findings provide computational neuroscientists with a novel and large set of observations that models must capture when aiming to replicate cortical cellular excitability. As we take the first step in examining the responses from different genetically identified cell types, future developments on the special/restricted expression of opsins and photoactivation hardware may help this process. Both the study of long-term excitability at the single-cell level and the investigation of channelrhodopsin hold merit, as does modelling of both systems. We believe that scientific progress may require a comprehensive integration of empirical and theoretical approaches, with continuous refinement and testing of models based on new data. However, we currently observe a lack of effective understanding and communication between experimentalists and computational neuroscientists.

Bibliography

Blue Brain Portal. https://portal.bluebrain.epfl.ch/.

M. Abeles. *Corticonics: Neural Circuits of the Cerebral Cortex*. Cambridge University Press, February 1991. ISBN 978-0-521-37617-4.

E. D. Adrian and Yngve Zotterman. The impulses produced by sensory nerve-endings. *J. Physiol.*, 61(2):151–171, 1926. ISSN 1469-7793. doi: 10.1113/jphysiol.1926.sp002281.

Tzitzitlini Alejandre-García, Samuel Kim, Jesús Pérez-Ortega, and Rafael Yuste. Intrinsic excitability mechanisms of neuronal ensemble formation. *eLife*, 11:e77470, May 2022. ISSN 2050-084X. doi: 10.7554/eLife.77470.

Daniel L. Alkon. Calcium-Mediated Reduction of Ionic Currents: A Biophysical Memory Trace. *Science*, 226(4678):1037–1045, November 1984. doi: 10.1126/science.6093258.

Allen Brain Atlas. Overview :: Allen Brain Atlas: Cell Types. https://celltypes.brain-map.org/, 2021.

Laurent Badel, Sandrine Lefort, Thomas K. Berger, Carl C. H. Petersen, Wulfram Gerstner, and Magnus J. E. Richardson. Extracting non-linear integrate-and-fire models from experimental data using dynamic I–V curves. *Biol Cybern*, 99(4):361–370, November 2008. ISSN 1432-0770. doi: 10.1007/s00422-008-0259-4.

Thomas Baltz and Thomas Voigt. Interaction of electrically evoked activity with intrinsic dynamics of cultured cortical networks with and without functional fast GABAergic synaptic transmission. *Front. Cell. Neurosci.*, 9, 2015. ISSN 1662-5102. doi: 10.3389/fncel.2015.00272.

Bruce P. Bean. The action potential in mammalian central neurons. *Nat Rev Neurosci*, 8 (6):451–465, June 2007. ISSN 1471-0048. doi: 10.1038/nrn2148.

David Beniaguev, Idan Segev, and Michael London. Single cortical neurons as deep artificial neural networks. *Neuron*, 109(17):2727–2739.e3, September 2021. ISSN 0896-6273. doi: 10.1016/j.neuron.2021.07.002.

Michael Beyeler, Emily L. Rounds, Kristofor D. Carlson, Nikil Dutt, and Jeffrey L. Krichmar. Neural correlates of sparse coding and dimensionality reduction. *PLoS Comput Biol*, 15(6):e1006908, June 2019. ISSN 1553-734X. doi: 10.1371/journal.pcbi.1006908.

Romain Brette. Is coding a relevant metaphor for the brain? *Behav. Brain Sci.*, 42:e215, 2019/ed. ISSN 0140-525X, 1469-1825. doi: 10.1017/S0140525X19000049.

György Buzsáki. Large-scale recording of neuronal ensembles. *Nat Neurosci*, 7(5):446–451, May 2004. ISSN 1546-1726. doi: 10.1038/nn1233.

György Buzsáki. Neural Syntax: Cell Assemblies, Synapsembles, and Readers. *Neuron*, 68(3):362–385, November 2010. ISSN 0896-6273. doi: 10.1016/j.neuron.2010.09.023.

Danilo Bzdok, Thomas E. Nichols, and Stephen M. Smith. Towards algorithmic analytics for large-scale datasets. *Nat Mach Intell*, 1(7):296–306, July 2019. ISSN 2522-5839. doi: 10.1038/s42256-019-0069-5.

Luis Carrillo-Reid, Weijian Yang, Yuki Bando, Darcy S. Peterka, and Rafael Yuste. Imprinting and recalling cortical ensembles. *Science*, 353(6300):691–694, August 2016. doi: 10.1126/science.aaf7560.

Naveen Chandra and Edi Barkai. A non-synaptic mechanism of complex learning: Modulation of intrinsic neuronal excitability. *Neurobiology of Learning and Memory*, 154: 30–36, October 2018. ISSN 1074-7427. doi: 10.1016/j.nlm.2017.11.015.

Fernando J. Chaure, Hernan G. Rey, and Rodrigo Quian Quiroga. A novel and fully automatic spike-sorting implementation with variable number of features. *J. Neurophysiol.*, 120(4):1859–1871, October 2018. ISSN 0022-3077. doi: 10.1152/jn.00339.2018.

Shmuel Chen, Hailing Su, Cuiyong Yue, Stefan Remy, Michel Royeck, Dmitry Sochivko, Thoralf Opitz, Heinz Beck, and Yoel Yaari. An Increase in Persistent Sodium Current Contributes to Intrinsic Neuronal Bursting After Status Epilepticus. *J. Neurophysiol.*, 105(1):117–129, January 2011. ISSN 0022-3077. doi: 10.1152/jn.00184.2010.

Susana Andrea Contreras, Jan-Hendrik Schleimer, Allan T. Gulledge, and Susanne Schreiber. Activity-mediated accumulation of potassium induces a switch in firing pattern and neuronal excitability type. *PLOS Computational Biology*, 17(5):e1008510, May 2021. ISSN 1553-7358. doi: 10.1371/journal.pcbi.1008510.

David Dahmen, Moritz Layer, Lukas Deutz, Paulina Anna Dąbrowska, Nicole Voges, Michael von Papen, Thomas Brochier, Alexa Riehle, Markus Diesmann, Sonja Grün, and Moritz Helias. Global organization of neuronal activity only requires unstructured local connectivity. *eLife*, 11:e68422, January 2022. ISSN 2050-084X. doi: 10.7554/eLife.68422.

Gaël Daoudal and Dominique Debanne. Long-Term Plasticity of Intrinsic Excitability: Learning Rules and Mechanisms. *Learn. Mem.*, 10(6):456–465, November 2003. ISSN 1072-0502, 1549-5485. doi: 10.1101/lm.64103.

Dominique Debanne and Mu-Ming Poo. Spike-timing dependent plasticity beyond synapse - pre- and post-synaptic plasticity of intrinsic neuronal excitability. *Front. Synaptic Neurosci.*, 2, 2010. ISSN 1663-3563.

Dominique Debanne, Yanis Inglebert, and Michaël Russier. Plasticity of intrinsic neuronal excitability. *Current Opinion in Neurobiology*, 54:73–82, February 2019. ISSN 0959-4388. doi: 10.1016/j.conb.2018.09.001.

Niraj S. Desai, Lana C. Rutherford, and Gina G. Turrigiano. Plasticity in the intrinsic excitability of cortical pyramidal neurons. *Nat Neurosci*, 2(6):515–520, June 1999. ISSN 1546-1726. doi: 10.1038/9165.

A Destexhe, M Rudolph, J. M Fellous, and T. J Sejnowski. Fluctuating synaptic conductances recreate in vivo-like activity in neocortical neurons. *Neuroscience*, 107(1):13–24, November 2001. ISSN 0306-4522. doi: 10.1016/S0306-4522(01)00344-X.

Alain Destexhe, Michael Rudolph, and Denis Paré. The high-conductance state of neocortical neurons in vivo. *Nat Rev Neurosci*, 4(9):739–751, September 2003. ISSN 1471-003X, 1471-0048. doi: 10.1038/nrn1198.

Jordane Dimidschstein, Qian Chen, Robin Tremblay, Stephanie L. Rogers, Giuseppe-Antonio Saldi, Lihua Guo, Qing Xu, Runpeng Liu, Congyi Lu, Jianhua Chu, Joshua S. Grimley, Anne-Rachel Krostag, Ajamete Kaykas, Michael C. Avery, Mohammad S. Rashid, Myungin Baek, Amanda L. Jacob, Gordon B. Smith, Daniel E. Wilson, Georg Kosche, Illya Kruglikov, Tomasz Rusielewicz, Vibhakar C. Kotak, Todd M. Mowery, Stewart A. Anderson, Edward M. Callaway, Jeremy S. Dasen, David Fitzpatrick, Valentina Fossati, Michael A. Long, Scott Noggle, John H. Reynolds, Dan H. Sanes, Bernardo Rudy, Guoping Feng, and Gord Fishell. A viral strategy for targeting and manipulating interneurons across vertebrate species. *Nat Neurosci*, 19(12):1743–1749, December 2016. ISSN 1546-1726. doi: 10.1038/nn.4430.

Tanjew Dittgen, Axel Nimmerjahn, Shoji Komai, Pawel Licznerski, Jack Waters, Troy W. Margrie, Fritjof Helmchen, Winfried Denk, Michael Brecht, and Pavel Osten. Lentivirus-based genetic manipulations of cortical neurons and their optical and electrophysiological monitoring in vivo. *PNAS*, 101(52):18206–18211, December 2004. ISSN 0027-8424, 1091-6490. doi: 10.1073/pnas.0407976101.

Guillaume Drion, Timothy O'Leary, and Eve Marder. Ion channel degeneracy enables robust and tunable neuronal firing rates. *PNAS*, 112(38):E5361–E5370, September 2015.

A. Eke, P. Hermán, J. Bassingthwaighte, G. Raymond, D. Percival, M. Cannon, I. Balla, and C. Ikrényi. Physiological time series: Distinguishing fractal noises from motions. *Pflügers Arch – Eur J Physiol*, 439(4):403–415, February 2000. ISSN 1432-2013. doi: 10.1007/s004249900135.

Valentina Emiliani, Emilia Entcheva, Rainer Hedrich, Peter Hegemann, Kai R. Konrad, Christian Lüscher, Mathias Mahn, Zhuo-Hua Pan, Ruth R. Sims, Johannes Vierock, and Ofer Yizhar. Optogenetics for light control of biological systems. *Nat Rev Methods Primers*, 2(1):1–25, July 2022. ISSN 2662-8449. doi: 10.1038/s43586-022-00136-4.

A. Aldo Faisal, Luc P. J. Selen, and Daniel M. Wolpert. Noise in the nervous system. *Nat Rev Neurosci*, 9(4):292–303, April 2008. ISSN 1471-0048. doi: 10.1038/nrn2258.

U. Fano. Ionization Yield of Radiations. II. The Fluctuations of the Number of Ions. *Phys. Rev.*, 72(1):26–29, July 1947. doi: 10.1103/PhysRev.72.26.

Mary K. Foecking and Hans Hofstetter. Powerful and versatile enhancer-promoter unit for mammalian expression vectors. *Gene*, 45(1):101–105, January 1986. ISSN 0378-1119. doi: 10.1016/0378-1119(86)90137-X.

Thomas J. Foutz, Richard L. Arlow, and Cameron C. McIntyre. Theoretical principles underlying optical stimulation of a channelrhodopsin-2 positive pyramidal neuron. *J.*

Neurophysiol., 107(12):3235–3245, June 2012. ISSN 0022-3077. doi: 10.1152/jn.00501.2011.

R F Fox. Stochastic versions of the Hodgkin-Huxley equations. *Biophys. J.*, 72, 1997.

Ronald F. Fox and Yan-nan Lu. Emergent collective behavior in large numbers of globally coupled independently stochastic ion channels. *Phys. Rev. E*, 49(4):3421–3431, April 1994. doi: 10.1103/PhysRevE.49.3421.

Tian-Ming Fu, Guosong Hong, Tao Zhou, Thomas G. Schuhmann, Robert D. Viveros, and Charles M. Lieber. Stable long-term chronic brain mapping at the single-neuron level. *Nat Methods*, 13(10):875–882, October 2016. ISSN 1548-7105. doi: 10.1038/nmeth.3969.

Asaf Gal and Shimon Marom. Self-organized criticality in single-neuron excitability. *Phys. Rev. E*, 88(6):062717, December 2013. doi: 10.1103/PhysRevE.88.062717.

Asaf Gal, Danny Eytan, Avner Wallach, Maya Sandler, Jackie Schiller, and Shimon Marom. Dynamics of Excitability over Extended Timescales in Cultured Cortical Neurons. *J. Neurosci.*, 30(48):16332–16342, December 2010. ISSN 0270-6474, 1529-2401. doi: 10.1523/JNEUROSCI.4859-10.2010.

Charles R. Gallistel and Peter D Balsam. Time to rethink the neural mechanisms of learning and memory. *Neurobiology of Learning and Memory*, 108:136–144, February 2014. ISSN 1074-7427. doi: 10.1016/j.nlm.2013.11.019.

Célia Gasselin, Yanis Inglebert, Norbert Ankri, and Dominique Debanne. Plasticity of intrinsic excitability during LTD is mediated by bidirectional changes in h-channel activity. *Sci Rep*, 7(1):14418, October 2017. ISSN 2045-2322. doi: 10.1038/s41598-017-14874-z.

Chiara Gastaldi, Tilo Schwalger, Emanuela De Falco, Rodrigo Quian Quiroga, and Wulfram Gerstner. When shared concept cells support associations: Theory of overlapping

memory engrams. *PLOS Computational Biology*, 17(12):e1009691, December 2021. ISSN 1553-7358. doi: 10.1371/journal.pcbi.1009691.

Lin Ge and Xiao-dong Liu. Electrical resonance with voltage-gated ion channels: Perspectives from biophysical mechanisms and neural electrophysiology. *Acta Pharmacol Sin*, 37(1):67–74, January 2016. ISSN 1745-7254. doi: 10.1038/aps.2015.140.

Wulfram Gerstner. *Spiking Neuron Models: Single Neurons, Populations, Plasticity*. Cambridge University Press, Cambridge, U.K. ; New York, illustrated edition edition, August 2002. ISBN 978-0-521-89079-3.

Carleton P. Goold and Roger A. Nicoll. Single-cell optogenetic excitation drives homeostatic synaptic depression. *Neuron*, 68(3):512–528, November 2010. ISSN 1097-4199. doi: 10.1016/j.neuron.2010.09.020.

Michael E. Greenberg, Edward B. Ziff, and Lloyd A. Greene. Stimulation of Neuronal Acetylcholine Receptors Induces Rapid Gene Transcription. *Science*, 234(4772):80–83, October 1986. doi: 10.1126/science.3749894.

Marifi Güler. An Investigation of the Stochastic Hodgkin-Huxley Models Under Noisy Rate Functions. *Neural Computation*, 25(9):2355–2372, September 2013. ISSN 0899-7667. doi: 10.1162/NECO_a_00487.

Christian Hansel and John F. Disterhoft. Why is synaptic plasticity not enough? *Neurobiology of Learning and Memory*, 176:107336, December 2020. ISSN 1074-7427. doi: 10.1016/j.nlm.2020.107336.

Kenneth D. Harris, Darrell A. Henze, Jozsef Csicsvari, Hajime Hirase, and György Buzsáki. Accuracy of Tetrode Spike Separation as Determined by Simultaneous Intracellular and Extracellular Measurements. *J. Neurophysiol.*, 84(1):401–414, July 2000. ISSN 0022-3077. doi: 10.1152/jn.2000.84.1.401.

Michael Häusser. The Hodgkin-Huxley theory of the action potential. *Nat Neurosci*, 3 (11):1165–1165, November 2000. ISSN 1546-1726. doi: 10.1038/81426.

Darrell A. Henze, Zsolt Borhegyi, Jozsef Csicsvari, Akira Mamiya, Kenneth D. Harris, and György Buzsáki. Intracellular Features Predicted by Extracellular Recordings in the Hippocampus In Vivo. *J. Neurophysiol.*, 84(1):390–400, July 2000. ISSN 0022-3077. doi: 10.1152/jn.2000.84.1.390.

A. L. Hodgkin and A. F. Huxley. A quantitative description of membrane current and its application to conduction and excitation in nerve. *J Physiol*, 117(4):500–544, August 1952. ISSN 0022-3751.

Chiaki Hoshino, Ayumu Konno, Nobutake Hosoi, Ryosuke Kaneko, Ryo Mukai, Junichi Nakai, and Hirokazu Hirai. GABAergic neuron-specific whole-brain transduction by AAV-PHP.B incorporated with a new GAD65 promoter. *Molecular Brain*, 14(1):33, February 2021. ISSN 1756-6606. doi: 10.1186/s13041-021-00746-1.

Z. Josh Huang and Anirban Paul. The diversity of GABAergic neurons and neural communication elements. *Nat Rev Neurosci*, 20(9):563–572, September 2019. ISSN 1471-0048. doi: 10.1038/s41583-019-0195-4.

Donald R. Humphrey and Edward M. Schmidt. Extracellular Single-Unit Recording Methods. In Alan A. Boulton, Glen B. Baker, and Case H. Vanderwolf, editors, *Neurophysiological Techniques: Applications to Neural Systems*, Neuromethods, pages 1–64. Humana Press, Totowa, NJ, 1990. ISBN 978-1-59259-620-1. doi: 10.1385/0-89603-185-3:1.

David L. Hunt, Daniele Linaro, Bailu Si, Sandro Romani, and Nelson Spruston. A novel pyramidal cell type promotes sharp-wave synchronization in the hippocampus. *Nat Neurosci*, 21(7):985–995, July 2018. ISSN 1546-1726. doi: 10.1038/s41593-018-0172-7.

W. Irnich. The Chronaxie Time and Its Practical Importance. *Pacing Clin. Electrophysiol.*, 3(3):292–301, 1980. ISSN 1540-8159. doi: 10.1111/j.1540-8159.1980.tb05236.x.

Yasuhiko Jimbo, Akio Kawana, Pietro Parodi, and Vincent Torre. The dynamics of a neuronal culture of dissociated cortical neurons of neonatal rats. *Biol Cybern*, 83(1): 1–20, June 2000. ISSN 1432-0770. doi: 10.1007/PL00007970.

Nathan C. Klapoetke, Yasunobu Murata, Sung Soo Kim, Stefan R. Pulver, Amanda Birdsey-Benson, Yong Ku Cho, Tania K. Morimoto, Amy S. Chuong, Eric J. Carpenter, Zhijian Tian, Jun Wang, Yinlong Xie, Zhixiang Yan, Yong Zhang, Brian Y. Chow, Barbara Surek, Michael Melkonian, Vivek Jayaraman, Martha Constantine-Paton, Gane Ka-Shu Wong, and Edward S. Boyden. Independent optical excitation of distinct neural populations. *Nat. Methods*, 11(3):338–346, March 2014. ISSN 1548-7105. doi: 10.1038/nmeth.2836.

John W. Krakauer, Asif A. Ghazanfar, Alex Gomez-Marin, Malcolm A. MacIver, and David Poeppel. Neuroscience Needs Behavior: Correcting a Reductionist Bias. *Neuron*, 93(3):480–490, February 2017. ISSN 0896-6273. doi: 10.1016/j.neuron.2016.12.041.

Julija Krupic. Wire together, fire apart. *Science*, 357(6355):974–975, September 2017. doi: 10.1126/science.aao4159.

Gabriele Lignani, Enrico Ferrea, Francesco Difato, Jessica Amaru', Eleonora Ferroni, Eleonora Lugara', Stefano Espinoza, Raul R. Gainetdinov, Pietro Baldelli, and Fabio Benfenati. Long-term optical stimulation of channelrhodopsin-expressing neurons to study network plasticity. *Front. Mol. Neurosci.*, 6, 2013. ISSN 1662-5099. doi: 10.3389/fnmol.2013.00022.

John Lisman, Katherine Cooper, Megha Sehgal, and Alcino J. Silva. Memory formation depends on both synapse-specific modifications of synaptic strength and cell-specific increases in excitability. *Nat Neurosci*, 21(3):309–314, March 2018. ISSN 1546-1726. doi: 10.1038/s41593-018-0076-6.

Steven B. Lowen and Malvin C. Teich. The periodogram and Allan variance reveal fractal exponents greater than unity in auditory-nerve spike trains. *The Journal of the Acoustical Society of America*, 99(6):3585–3591, June 1996. ISSN 0001-4966. doi: 10.1121/1.414979.

Steven Bradley Lowen and Malvin Carl Teich. *Fractal-Based Point Processes*. John Wiley & Sons, October 2005. ISBN 978-0-471-75470-1.

Brian N. Lundstrom, Matthew H. Higgs, William J. Spain, and Adrienne L. Fairhall. Fractional differentiation by neocortical pyramidal neurons. *Nat Neurosci*, 11(11): 1335–1342, November 2008. ISSN 1546-1726. doi: 10.1038/nn.2212.

Thomas Mager, David Lopez de la Morena, Verena Senn, Johannes Schlotte, Anna D´Errico, Katrin Feldbauer, Christian Wrobel, Sangyong Jung, Kai Bodensiek, Vladan Rankovic, Lorcan Browne, Antoine Huet, Josephine Jüttner, Phillip G. Wood, Johannes J. Letzkus, Tobias Moser, and Ernst Bamberg. High frequency neural spiking and auditory signaling by ultrafast red-shifted optogenetics. *Nat Commun*, 9(1):1750, May 2018. ISSN 2041-1723. doi: 10.1038/s41467-018-04146-3.

Z. F. Mainen and T. J. Sejnowski. Reliability of spike timing in neocortical neurons. *Science*, 268(5216):1503–1506, June 1995. ISSN 0036-8075, 1095-9203. doi: 10.1126/science.7770778.

Eve Marder, L. F. Abbott, Gina G. Turrigiano, Zheng Liu, and Jorge Golowasch. Memory from the dynamics of intrinsic membrane currents. *Proc. Natl. Acad. Sci.*, 93(24):13481–13486, November 1996. doi: 10.1073/pnas.93.24.13481.

Henry Markram, Maria Toledo-Rodriguez, Yun Wang, Anirudh Gupta, Gilad Silberberg, and Caizhi Wu. Interneurons of the neocortical inhibitory system. *Nat. Rev. Neurosci.*, 5(10):793–807, October 2004. ISSN 1471-0048. doi: 10.1038/nrn1519.

Henry Markram, Eilif Muller, Srikanth Ramaswamy, Michael W. Reimann, Marwan Abdellah, Carlos Aguado Sanchez, Anastasia Ailamaki, Lidia Alonso-Nanclares, Nicolas Antille, Selim Arsever, Guy Antoine Atenekeng Kahou, Thomas K. Berger, Ahmet Bilgili, Nenad Buncic, Athanassia Chalimourda, Giuseppe Chindemi, Jean-Denis Courcol, Fabien Delalondre, Vincent Delattre, Shaul Druckmann, Raphael Dumusc, James Dynes, Stefan Eilemann, Eyal Gal, Michael Emiel Gevaert, Jean-Pierre Ghobril, Albert Gidon, Joe W. Graham, Anirudh Gupta, Valentin Haenel, Etay Hay, Thomas Heinis, Juan B. Hernando, Michael Hines, Lida Kanari, Daniel Keller, John Kenyon, Georges Khazen, Yihwa Kim, James G. King, Zoltan Kisvarday, Pramod Kumbhar, Sébastien Lasserre, Jean-Vincent Le Bé, Bruno R. C. Magalhães, Angel Merchán-Pérez, Julie Meystre, Benjamin Roy Morrice, Jeffrey Muller, Alberto Muñoz-Céspedes, Shruti Muralidhar, Keerthan Muthurasa, Daniel Nachbaur, Taylor H. Newton, Max Nolte, Aleksandr Ovcharenko, Juan Palacios, Luis Pastor, Rodrigo Perin, Rajnish Ranjan, Imad Riachi, José-Rodrigo Rodríguez, Juan Luis Riquelme, Christian Rössert, Konstantinos Sfyrakis, Ying Shi, Julian C. Shillcock, Gilad Silberberg, Ricardo Silva, Farhan Tauheed, Martin Telefont, Maria Toledo-Rodriguez, Thomas Tränkler, Werner Van Geit, Jafet Villafranca Díaz, Richard Walker, Yun Wang, Stefano M. Zaninetta, Javier DeFelipe, Sean L. Hill, Idan Segev, and Felix Schürmann. Reconstruction and Simulation of Neocortical Microcircuitry. *Cell*, 163(2):456–492, October 2015. ISSN 0092-8674, 1097-4172. doi: 10.1016/j.cell.2015.09.029.

S Marom and L F Abbott. Modeling state-dependent inactivation of membrane currents. *Biophys J*, 67(2):515–520, August 1994. ISSN 0006-3495.

Shimon Marom. Neural timescales or lack thereof. *Progress in Neurobiology*, 90(1):16–28, January 2010. ISSN 0301-0082. doi: 10.1016/j.pneurobio.2009.10.003.

Shimon Marom and Goded Shahaf. Development, learning and memory in large random networks of cortical neurons: Lessons beyond anatomy. *Quart. Rev. Biophys.*, 35(1):

63–87, February 2002. ISSN 0033-5835, 1469-8994. doi: 10.1017/S0033583501003742.

Warren S. McCulloch and Walter Pitts. A logical calculus of the ideas immanent in nervous activity. *Bulletin of Mathematical Biophysics*, 5(4):115–133, December 1943. ISSN 1522-9602. doi: 10.1007/BF02478259.

Georg Nagel, Tanjef Szellas, Wolfram Huhn, Suneel Kateriya, Nona Adeishvili, Peter Berthold, Doris Ollig, Peter Hegemann, and Ernst Bamberg. Channelrhodopsin-2, a directly light-gated cation-selective membrane channel. *Proc. Natl. Acad. Sci.*, 100(24): 13940–13945, November 2003. doi: 10.1073/pnas.1936192100.

Martin Paul Nawrot. Analysis and Interpretation of Interval and Count Variability in Neural Spike Trains. In Sonja Grün and Stefan Rotter, editors, *Analysis of Parallel Spike Trains*, Springer Series in Computational Neuroscience, pages 37–58. Springer US, Boston, MA, 2010. ISBN 978-1-4419-5675-0. doi: 10.1007/978-1-4419-5675-0_3.

Hillel Ori, Hananel Hazan, Eve Marder, and Shimon Marom. Dynamic clamp constructed phase diagram for the Hodgkin and Huxley model of excitability. *PNAS*, 117 (7):3575–3582, February 2020.

Athanasia Papoutsi, Kyriaki Sidiropoulou, and Panayiota Poirazi. Memory Beyond Synaptic Plasticity: The Role of Intrinsic Neuronal Excitability. In *Memory Mechanisms in Health and Disease*, pages 53–80. WORLD SCIENTIFIC, November 2011. ISBN 978-981-4366-69-4. doi: 10.1142/9789814366700_0003.

Rocco Pulizzi, Gabriele Musumeci, Chris Van den Haute, Sebastiaan Van De Vijver, Veerle Baekelandt, and Michele Giugliano. Brief wide-field photostimuli evoke and modulate oscillatory reverberating activity in cortical networks. *Sci. Rep.*, 6(1):24701, April 2016. ISSN 2045-2322. doi: 10.1038/srep24701.

Rodrigo Quian Quiroga. Concept cells: The building blocks of declarative memory functions. *Nat Rev Neurosci*, 13(8):587–597, August 2012. ISSN 1471-0048. doi: 10.1038/nrn3251.

Sebastian Reinartz. Long-Term Activity Dynamics of Single Neurons and Networks. In Michela Chiappalone, Valentina Pasquale, and Monica Frega, editors, *In Vitro Neuronal Networks: From Culturing Methods to Neuro-Technological Applications*, Advances in Neurobiology, pages 331–350. Springer International Publishing, Cham, 2019. ISBN 978-3-030-11135-9. doi: 10.1007/978-3-030-11135-9_14.

Sebastian Reinartz, Istvan Biro, Asaf Gal, Michele Giugliano, and Shimon Marom. Synaptic dynamics contribute to long-term single neuron response fluctuations. *Front. Neural Circuits*, 8, 2014. ISSN 1662-5110. doi: 10.3389/fncir.2014.00071.

Michiel W. H. Remme and Wytse J. Wadman. Homeostatic Scaling of Excitability in Recurrent Neural Networks. *PLOS Computational Biology*, 8(5):e1002494, May 2012. ISSN 1553-7358. doi: 10.1371/journal.pcbi.1002494.

Armando Romani, Felix Schürmann, Henry Markram, and Michele Migliore. Reconstruction of the Hippocampus. In Michele Giugliano, Mario Negrello, and Daniele Linaro, editors, *Computational Modelling of the Brain: Modelling Approaches to Cells, Circuits and Networks*, Advances in Experimental Medicine and Biology, pages 261–283. Springer International Publishing, Cham, 2022. ISBN 978-3-030-89439-9. doi: 10.1007/978-3-030-89439-9_11.

Peter F. Rowat and Priscilla E. Greenwood. The ISI distribution of the stochastic Hodgkin-Huxley neuron. *Front. Comput. Neurosci.*, 8, 2014. ISSN 1662-5188.

Emilio R. G. Sanabria, Hailing Su, and Yoel Yaari. Initiation of network bursts by Ca2+-dependent intrinsic bursting in the rat pilocarpine model of temporal lobe epilepsy. *J. Physiol.*, 532(1):205–216, 2001. ISSN 1469-7793. doi: 10.1111/j.1469-7793.2001.0205g.x.

Sant Saran, Neha Gupta, and Sukhdev Roy. Theoretical analysis of low-power fast optogenetic control of firing of Chronos-expressing neurons. *NPh*, 5(2):025009, May 2018. ISSN 2329-423X, 2329-4248. doi: 10.1117/1.NPh.5.2.025009.

Or A. Shemesh, Dimitrii Tanese, Valeria Zampini, Changyang Linghu, Kiryl Piatkevich, Emiliano Ronzitti, Eirini Papagiakoumou, Edward S. Boyden, and Valentina Emiliani. Temporally precise single-cell-resolution optogenetics. *Nat Neurosci*, 20(12):1796–1806, December 2017. ISSN 1546-1726. doi: 10.1038/s41593-017-0018-8.

Daniel Soudry and Ron Meir. History-Dependent Dynamics in a Generic Model of Ion Channels – An Analytic Study. *Front. Comput. Neurosci.*, 4, 2010. ISSN 1662-5188.

Daniel Soudry and Ron Meir. Conductance-Based Neuron Models and the Slow Dynamics of Excitability. *Front. Comput. Neurosci.*, 6, 2012. ISSN 1662-5188.

Daniel Soudry and Ron Meir. The neuronal response at extended timescales: Long-term correlations without long-term memory. *Front. Comput. Neurosci.*, 8, 2014. ISSN 1662-5188. doi: 10.3389/fncom.2014.00035.

Ian H. Stevenson and Konrad P. Kording. How advances in neural recording affect data analysis. *Nat Neurosci*, 14(2):139–142, February 2011. ISSN 1546-1726. doi: 10.1038/nn.2731.

Wondimu Teka, Toma M. Marinov, and Fidel Santamaria. Neuronal Spike Timing Adaptation Described with a Fractional Leaky Integrate-and-Fire Model. *PLOS Computational Biology*, 10(3):e1003526, March 2014. ISSN 1553-7358. doi: 10.1371/journal.pcbi.1003526.

Stefan Thurner, Steven B. Lowen, Markus C. Feurstein, Conor Heneghan, Hans G. Feichtinger, and Malvin C. Teich. Analysis, Synthesis, and Estimation of Fractal-Rate Stochastic Point Processes. *Fractals*, 05(04):565–595, December 1997. ISSN 0218-348X. doi: 10.1142/S0218348X97000462.

Heather K. Titley, Nicolas Brunel, and Christian Hansel. Toward a Neurocentric View of Learning. *Neuron*, 95(1):19–32, July 2017. ISSN 0896-6273. doi: 10.1016/j.neuron.2017.05.021.

Robert G. Turcott and Malvin C. Teich. Fractal character of the electrocardiogram: Distinguishing heart-failure and normal patients. *Ann Biomed Eng*, 24(2):269–293, March 1996. ISSN 1573-9686. doi: 10.1007/BF02667355.

A. Van der Perren, J. Toelen, M. Carlon, C. Van den Haute, F. Coun, B. Heeman, V. Reumers, L. H. Vandenberghe, J. M. Wilson, Z. Debyser, and V. Baekelandt. Efficient and stable transduction of dopaminergic neurons in rat substantia nigra by rAAV 2/1, 2/2, 2/5, 2/6.2, 2/7, 2/8 and 2/9. *Gene Ther.*, 18(5):517–527, May 2011. ISSN 1476-5462. doi: 10.1038/gt.2010.179.

Eleni Vasilaki and Michele Giugliano. Emergence of Connectivity Motifs in Networks of Model Neurons with Short- and Long-Term Plastic Synapses. *PLOS ONE*, 9(1):e84626, January 2014. ISSN 1932-6203. doi: 10.1371/journal.pone.0084626.

Christophe Verbist, Michael G. Müller, Huibert D. Mansvelder, Robert Legenstein, and Michele Giugliano. The location of the axon initial segment affects the bandwidth of spike initiation dynamics. *PLoS Comput Biol*, 16(7):e1008087, July 2020. ISSN 1553-734X. doi: 10.1371/journal.pcbi.1008087.

Daniel A. Wagenaar, Jerome Pine, and Steve M. Potter. Effective parameters for stimulation of dissociated cultures using multi-electrode arrays. *Journal of Neuroscience Methods*, 138(1):27–37, September 2004. ISSN 0165-0270. doi: 10.1016/j.jneumeth.2004.03.005.

Pan Ke Wang, Sio Hang Pun, Chang Hao Chen, Elizabeth A. McCullagh, Achim Klug, Anan Li, Mang I. Vai, Peng Un Mak, and Tim C. Lei. Low-latency single channel

real-time neural spike sorting system based on template matching. *PLOS ONE*, 14(11): e0225138, November 2019. ISSN 1932-6203. doi: 10.1371/journal.pone.0225138.

Xiao-Jing Wang and György Buzsáki. Gamma Oscillation by Synaptic Inhibition in a Hippocampal Interneuronal Network Model. *J. Neurosci.*, 16(20):6402–6413, October 1996. ISSN 0270-6474, 1529-2401. doi: 10.1523/JNEUROSCI.16-20-06402.1996.

John C. Williams, Jianjin Xu, Zhongju Lu, Aleksandra Klimas, Xuxin Chen, Christina M. Ambrosi, Ira S. Cohen, and Emilia Entcheva. Computational Optogenetics: Empirically-Derived Voltage- and Light-Sensitive Channelrhodopsin-2 Model. *PLOS Computational Biology*, 9(9):e1003220, September 2013. ISSN 1553-7358. doi: 10.1371/journal.pcbi.1003220.

Ee-Lynn Yap, Noah L. Pettit, Christopher P. Davis, M. Aurel Nagy, David A. Harmin, Emily Golden, Onur Dagliyan, Cindy Lin, Stephanie Rudolph, Nikhil Sharma, Eric C. Griffith, Christopher D. Harvey, and Michael E. Greenberg. Bidirectional perisomatic inhibitory plasticity of a Fos neuronal network. *Nature*, 590(7844):115–121, February 2021. ISSN 1476-4687. doi: 10.1038/s41586-020-3031-0.

Yosef Yarom and Jorn Hounsgaard. Voltage Fluctuations in Neurons: Signal or Noise? *Physiol. Rev.*, 91(3):917–929, July 2011. ISSN 0031-9333. doi: 10.1152/physrev.00019.2010.

Hugo Zeberg, Clas Blomberg, and Peter Århem. Ion Channel Density Regulates Switches between Regular and Fast Spiking in Soma but Not in Axons. *PLOS Computational Biology*, 6(4):e1000753, April 2010. ISSN 1553-7358. doi: 10.1371/journal.pcbi.1000753.

Roxana Zeraati, Yan-Liang Shi, Nicholas A. Steinmetz, Marc A. Gieselmann, Alexander Thiele, Tirin Moore, Anna Levina, and Tatiana A. Engel. Attentional modulation of intrinsic timescales in visual cortex and spatial networks. *bioRxiv*, page 2021.05.17.444537, May 2021. doi: 10.1101/2021.05.17.444537.

Siyuan Zhao, Xin Tang, Weiwen Tian, Sebastian Partarrieu, Ren Liu, Hao Shen, Jaeyong Lee, Shiqi Guo, Zuwan Lin, and Jia Liu. Tracking neural activity from the same cells during the entire adult life of mice. *Nat Neurosci*, pages 1–15, February 2023. ISSN 1546-1726. doi: 10.1038/s41593-023-01267-x.

A. Exploration of Conductance-based neuron models

Hodgkin-Huxley model

Hodgkin-Huxley model is based on the complex dynamics of ions through the cell membrane related to the evolution of the voltage potential based on the electrical circuit in Fig. 3.4. The elements of the circuit, arranged in parallel, are: a capacitance capacitor C_M to describe the action of the semipermeable cell membrane which separates the interior of the cell from the extracellular liquid, two nonlinear resistors R_K and R_{Na} to describe the ionic channels, respectively, of potassium and sodium and, finally, a passive resistance R_L that represents all the remaining ionic species (especially Cl^- ions). Usually the Hodgkin-Huxley model is built on the spatial and temporal dependence in order to describe the evolution of the membrane voltage, but for simplicity we considered the following ordinary differential equation for $V(t)$:

$$I = C_M \frac{dV}{dt} + \bar{g}_K n^4 (V - E_K) + \bar{g}_{Na} m^3 h (V - E_{Na}) + \bar{g}_L (V - E_L) \tag{A.1}$$

The coefficients that appear in the equation have the following meaning:

- gK: maximum value of the potassium conductance.

- g_{Na}: maximum value of the sodium conductance.
- g_L: term of constant conductance relative to all other ionic species.
- E_K: Equilibrium potential for potassium ions.
- E_{Na}: Equilibrium potential for sodium ions.
- E_L: Equilibrium potential for all other ionic species (mostly Cl^- ions).

The variables n, m, h are functions dependent on both the time and the value of the membrane potential of the cell, assuming values in $[0, 1]$ and interpreted in probabilistic terms. The evolution of the functions $n(t, V)$, $m(t, V)$, $h(t, V)$ is defined by the following differential equation structure. Let $X = X(t, V)$ be any of the three functions n, m, h then:

$$\frac{dX}{dt} = \alpha_X(V)(1 - X) - \beta_X(V)X. \tag{A.2}$$

X defines the probability of a gate being open defined for a specific ion. Looking at the macroscopic scale, X can also be the fraction of gates that are in the permissive state. The functions α_X and β_X determine the transfer rate of the activation particles which, respectively, flow from the outside in proportion to $(1 - X)$ to the inside of the membrane and from the inside in proportion to X to the outside (or vice versa for inactivation particles).

Hodgkin and Huxley derived the α_X and β_X functions from the experimental data as follows:

$$\alpha_n(V) = \frac{0.01(V+55)}{1-\exp(-0.1(V+55))}, \quad \beta_n(V) = 0.125\exp(-0.0125(V+65)) \tag{A.3}$$

$$\alpha_m(V) = \frac{0.1(V+40)}{1-\exp(-0.1(V+40))}, \quad \beta_m(V) = 4\exp(-0.0556(V+65)) \tag{A.4}$$

$$\alpha_h(V) = 0.07\exp(-0.05(V+65)), \quad \beta_h(V) = \frac{1}{1+\exp(-0.1(V+35))} \tag{A.5}$$

A.0.1. The Wang-Buzsáki model

The Wang-Buzsáki model is expressed using the Hodgkin-Huxley formalism to describe a neuron with a single compartment and conductances for sodium and potassium. The equation is given as:

$$I = C_m\frac{dV}{dt} + I_{Na} + I_K + I_L \tag{A.6}$$

where I_{Na}, I_K, and I_L represent the current contribution for each ionic species. The activation variable m for the transient sodium current is considered fast and is substituted by its steady-state function. The differential equations for the gate variables become:

$$\begin{cases} \frac{dh}{dt} & = \phi(\alpha_h(V)(1-h) - \beta_h(V)h) \\ \frac{dn}{dt} & = \phi(\alpha_n(V)(1-n) - \beta_n(V)n) \\ m_\infty & = \frac{\alpha_m(V)}{\alpha_m(V)+\beta_m(V)} \end{cases} \tag{A.7}$$

where ϕ represents the time constant of the gating variables, and α and β are the rate constants for the respective gating variables.

The Wang-Buzsáki differential equations were numerically solved using the Runge-Kutta method, which proved superior to both the Predictor-Corrector method and the

Forward Euler, initially estimated on the Hodgkin-Huxley model, affording a balance between model accuracy and computational efficiency.

Wang-Buzsáki with slow sodium inactivation

The evolution from the original Wang-Buzsáki model that we explore includes the low inactivation of sodium channels. This mechanism is incorporated into the basic model by introducing **s**, a new slow inactivation gate variable, into the sodium current:

$$I_{\mathrm{Na}} = \overline{g}_{\mathrm{Na}} m^3 h (E_{\mathrm{Na}} - \mathrm{V}) \tag{A.8}$$

$$\dot{s} = \delta(V)(1 - s) - \gamma(V)s \tag{A.9}$$

Eq. A.8 represents the current I_{Na} flowing through a sodium channel, where $\overline{g}_{\mathrm{Na}}$ is the maximum conductance of the channel, m and h are gating variables that depend on membrane potential V and control the opening and closing of the channel, and E_{Na} is the equilibrium potential for sodium ions. The equation states that the current is proportional to the maximum conductance, the cube of the opening variable (which represents the number of channels that are open), the closing variable (which represents the probability that a channel is open), and the difference between the sodium equilibrium potential and the membrane potential.

Eq. A.9 represents the dynamics of a hypothetical variable s, which could represent the activation or inactivation of some other ion channel. The function $\delta(\mathrm{V})$ represents the dependence of the rate of change of **s** on the membrane potential V, and is zero when V is below a certain threshold (i.e. the channel is closed at resting potential) and increases rapidly above that threshold (i.e. the channel opens). The function $\gamma(\mathrm{V})$ represents

the rate at which s returns to its resting value when V is below the threshold (i.e. the channel closes again). The equation states that the rate of change of s is proportional to the difference between the resting value (which is assumed to be the same as the initial value) and the current value of s, with a net rate of activation and inactivation depending on the balance between the functions $\delta(\mathrm{V})$ and $\gamma(\mathrm{V})$.

Wang-Buzsáki with slow sodium inactivation and potassium activation

We progress to augment the original Wang-Buzsáki model with an additional characteristic phenomenon in the equations, namely, slow potassium current activation. This modification, which may be either voltage or calcium dependent, has frequently been implicated in decreasing neuronal excitability after prolonged current step stimulation, commonly referred to as "spike frequency adaptation". The Wang-Buzsáki model featuring slow sodium inactivation, described in the preceding paragraph, is further modified by introducing a slowly activating potassium current exhibiting M-current kinetics, such that the total potassium current is given by:

$$\mathrm{I_K} = \overline{g}_\mathrm{K} n^4 (\mathrm{E_K} - \mathrm{V}) + \overline{g}_\mathrm{M} n^4 \mathrm{s}^2 (\mathrm{E_K} - \mathrm{V}), \tag{A.10}$$

with $\overline{g}_\mathrm{M} = 0.01 \overline{g}_\mathrm{K}$ and

$$\dot{s}_2 = \delta(\mathrm{V})(1 - s_2) - \gamma(\mathrm{V}) s_2 \tag{A.11}$$

This is a mathematical representation of the current flowing through a voltage-gated potassium (K) channel and a voltage-gated delayed rectifier potassium (M) channel in a neuron.

In Eq. A.10, the current through the K channel is given by the first term and depends on the potassium conductance ($\overline{g}_\mathrm{K}$), the activation variable for the K channel (n), the

reversal potential for potassium (E_K), and the membrane potential (V). The current through the M channel is given by the second term and depends on the M conductance ($\overline{g}_M$), n, the inactivation variable for the M channel (**s**), and E_K and V.

Eq. A.11 is the differential equation for the inactivation variable s_2, which determines the fraction of open M channels that are inactivated (i.e., cannot pass current even if the membrane potential is favourable). The rate of change of s depends on the voltage-dependent forward rate constant (δ) and the voltage-dependent backward rate constant (γ), which determine the rates at which s transitions from the non-inactivated to inactivated states and vice versa, respectively.

Wang-Buzsáki with slow sodium inactivation and potassium inactivation

The Wang-Buzsáki model is further enhanced by introducing a positive feedback mechanism through potassium inactivation. This type of behaviour is characterised by an increase in neuronal excitability following depolarisation. The slow variables, represented as **s**, directly impact future voltage responses, while the fast variables relax to a unique steady state and have no direct effect on future neuronal responses.

The **generic form of a conductance-based neuron model** includes a spike-generating mechanism modulated in time by rapid gating variables: $r := (r_1, ...r_m)^T$ and slow gating variables: $s := (s_1, ...s_m)^T$.

$$\dot{r}_j = f_j(r, s, I(t)), \quad j = 1, ..R \tag{A.12}$$

$$\dot{s}_i = \epsilon h_i(r, s), \qquad i = 1, ..S \tag{A.13}$$

where $\epsilon > 0$ is a regulatory parameter, rendering the dynamics of **s** much slower than the dynamics of **r**. For simplicity, all slow variables are normalised in the range [0, 1].

The Hodgkin-Huxley model is a special case of this model where $\mathbf{r} = (V, m, n, h)^{\mathrm{T}}$, and $\epsilon = 0$. This means that while $I(t) = 0$, $\mathbf{r}$ remains at a unique constant steady state i.e., the resting state. After each stimulation pulse, for certain values of initial conditions and I_0, we get either a "strong" response in $\mathbf{r}$ (AP generation) or a "weak" response in $\mathbf{r}$ (no AP generation). For a very small set of values of initial conditions and I_0 it is possible to generate an "intermediate" response ("weak AP-response"). Generally all responses are brief, and $\mathbf{r}$ rapidly relaxes back to the steady state within time t_r. If $\epsilon > 0$, we assume that $h_i(\mathbf{r}, \mathbf{s}) = h_i(\mathbf{r}, s_i)$ is a linear function of the kind:

$$\epsilon h_i(\mathbf{r}, \mathbf{s}) = \delta_i(\mathbf{r})(1 - s_i) - \gamma_i(\mathbf{r})s_i \tag{A.14}$$

where δ_i and γ_i are rate functions of magnitude ϵ.

The three models previously presented heavily rely on the values of $\mathbf{s}$. If a stimulation pulse with a strength of I_0 is given, the neuron will only produce an action potential if the voltage surpasses a certain threshold. To keep track of past stimulations, we use an excitability function, represented by E($\mathbf{s}$). For a neuron to produce an action potential, the value of E($\mathbf{s}$) must be greater than 0. This means that the excitability function E($\mathbf{s}$) sets the voltage threshold at which a neuron responds to a stimulation pulse with an amplitude of I_0. To determine the region where E($\mathbf{s}$) = 0, we set ϵ as zero and allow $\mathbf{r}$ to reach a stable state before applying a stimulation pulse.

As a result of the initial analysis, it has been determined that $E(\mathbf{s})$ is a monotonic function in each individual component of $\mathbf{s}$ and also increases monotonically as I_0 increases. Since the sodium current promotes depolarisation, an increase in this current will increase the probability of generating an action potential. However, an action potential will only occur if $\mathbf{s}$ exceeds a specific threshold θ. Our numerical analysis has demonstrated that

the shape of Φ is linear (though not shown) and this allows us to express the excitability function as $E(\mathbf{s}) = \mathbf{s}$ - θ, since the threshold θ varies inversely with I_0.

We adjusted the transfer rate constants for the **s** functions in the Wang-Buzsáki model, taking into account its slow inactivation of sodium channels. This resulted in the following values:

$$\gamma_1(V) = \frac{0.000511}{1 + e^{-0.3(V+17)}} \quad \text{and} \quad \delta_1(V) = 0.00005\, e^{(-V-85)/30} \tag{A.15}$$

A.0.2. Stochastic conductance-based model

In the Wang-Buzsáki model, we tried to incorporate stochasticity through three methods:

1. The introduction of subunit noise in the slow sodium inactivation based on previous works by Soudry and Meir (2010, 2012);

2. The incorporation of subunit noise in the gate function based on previous works by Fox (1997); Fox and Lu (1994); Rowat and Greenwood (2014);

3. The use of conductance noise through drift coefficients, which contain stochastic components that maintain non-trivial cross-correlation persistence.

In the following sections we will proceed introducing channel noise into the model previously validated, defining three different stochastic models. The numerical simulations are performed using stimulus train modelled as rectangular function in Eq. 3.2.

Results

Initially, the models of Wang-Buzsáki and Hodgkin-Huxley were created and contrasted.

The kinetics and maximal conductances of the neuron model are modified from the Hodgkin-Huxley model in order to display the salient properties of hippocampal and neocortical fast-spiking interneurons used in the Wang-Buzsáki experiments. The action potential in these cells is followed by a brief afterhyperpolarisation of -15 mV from the spike threshold (-55 mV). Consequently, during the spike repolarisation, the membrane potential reaches a minimum of about -70 mV instead of being close to the reversal potential of the K^+ current E_K, typically set at -90 mV. This behaviour is introduced in the model through a relatively small maximal conductance g_K and a fast gating process of I_K that quickly deactivates during spike repolarisation. Furthermore, the interneurons used in the experiments have the ability to fire repetitive spikes at high frequencies. With fast kinetics of the inactivation of I_{Na} (h gate), the activation of I_K (n gate), and the relatively high threshold of I_K, the model interneuron displays a large range of repetitive spiking frequencies in response to a constant injected current.

Hodgkin-Huxley model

Our investigation revealed that the Hodgkin-Huxley model is effective in approximating low frequencies but is inadequate for further study because it cannot accommodate high frequencies due to the rapid inactivation of sodium channels.

Wang-Buzsáki model

After careful consideration of our research objectives and the guidelines presented in (Soudry and Meir, 2012, 2014), we selected the Wang-Buzsáki model. This model is a deterministic conductance-based neuron model, which utilises the Hodgkin-Huxley formalism with N_a^+ and K^+ conductances to describe a *single compartment neuron model*.

In the framework of conductance-based neuron models, ion channels are modelled by their voltage-dependent conductances, and the excitable membrane is represented

by a capacitor. This approach provided a robust means for investigating the complex interplay of ions and voltage dynamics within a neuron.

Wang-Buzsáki model with slow sodium inactivation

Initially, we studied the original Wang-Buzsáki model, which incorporates slow inactivation of sodium channels. It may seem that the use of first-order kinetics is not suitable for accurately describing the recovery of sodium channels from slow inactivation, as it is influenced by past events and occurs over various time frames. However, recent studies have shown that the linear form of the equation remains applicable when analysing neurons subjected to pulse stimulation. For instance, previous investigations (Soudry and Meir, 2010) have demonstrated that it is a reliable approximation for the kinetics of ion channels with power-law memory. Therefore, the response of the Wang-Buzsáki model's sodium slow inactivation, as presented in (Soudry and Meir, 2010), is not substantially different from the outcome obtained using the equation for **s** Eq. A.9.

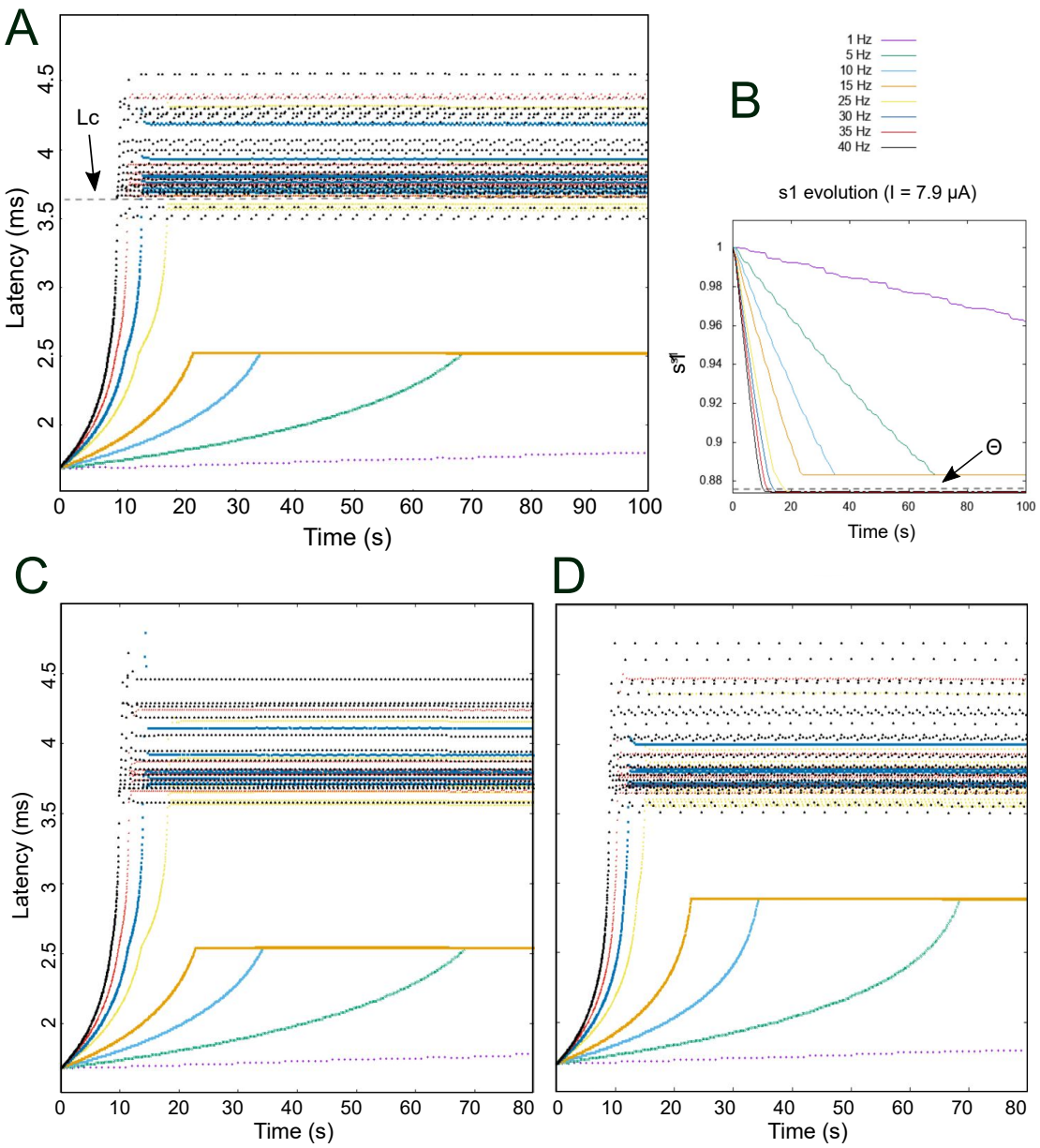

Figure A.1. Latency versus time as generated by the deterministic Wang-Buzsáki models for various stimulation frequencies. A: Wang-Buzsáki model with slow sodium inactivation. **B:** The evolution of the slow variable in the Wang-Buzsáki model with slow sodium inactivation. **C:** Wang-Buzsáki model with slow sodium inactivation and a slowly activating potassium current exhibiting M-current kinetics. **D:** Wang-Buzsáki model with slow sodium inactivation and a potassium inactivation.

Wang-Buzsáki model with slow sodium inactivation and potassium activation/inactivation

Potassium activation, which may be either voltage or calcium dependent, has frequently been implicated in decreasing neuronal excitability after prolonged current step stimulation, commonly referred to as "spike frequency adaptation". We introduced potassium activation as well as a positive feedback mechanism through potassium inactivation. This type of behaviour is characterised by an increase in neuronal excitability following depolarisation. The slow variables, represented as **s**, directly impact future voltage responses, while the fast variables relax to a unique steady state and have no direct effect on future neuronal responses (Fig. A.1).

Previous studies have shown that the availability of sodium increases with input frequency, while θ remains constant. Numerical simulations of the Wang-Buzsáki model revealed that the transient mode ends in a stable steady state when the input frequency is low or in an intermittent mode when **s(t)** reaches θ (Fig. A.1), which corresponds to the critical latency observed in experiments.

Fig. A.1 shows latency as a function of time for different stimulation rate f from 5 to 40 Hz, using stimulation at $I_0 = 7.9\ \mu$A. The transient phase speeds up when the stimulation frequency is increased, maintaining the same critical latency L_c. These results can be explained by Fig. A.1B showing that the sodium availability traces (t) accelerates its transient when the input frequency is increased, while θ does not change. The numerical simulations prove that the transient mode ends either in a stable steady state (when the input frequency is low), or in an intermittent mode, which occurs when $s(t)$ reaches θ, or equivalently, when the latency reaches $L(\theta)$, the critical latency observed in the experiment. However, there is a lack of variability in the latency patterns caused by the usage of deterministic algorithms in the model.

However, the deterministic algorithms used in the model fail to capture the variability in the latency patterns observed in experiments, as demonstrated by comparison with results from Fig. 2.4 (Gal et al., 2010) as well as our own findings Fig. 4.6.

Overall, the Wang-Buzsáki extended models provide insights into neuronal behaviour and the mechanisms behind the generation of action potentials. By incorporating fast and slow gating variables, as well as a positive feedback mechanism through potassium inactivation, the model is able to capture the complex dynamics of a neuron. The excitability function, determined by the values of $\mathbf{s}$, plays a crucial role in determining whether a neuron will generate an action potential in response to a stimulation pulse. The model provides a framework for further study and understanding of the electrical activity of neurons and their role in neural networks.

In photostimulated neurons (Fig. 4.7), similarly to findings by Gal et al., we note a fundamental observation that neural responses exhibit quasi-stable modes when observed continuously, with each mode corresponding to a typical response pattern. A neuron can display a diverse range of response patterns when observed over a sufficient length of time, such as stable responses, irregular responses, regular-clustered responses, and irregular-clustered responses. These different response dynamics are influenced by various stimulation protocols, which can make it challenging to map concepts.

B. Single cell *in silico* experiments

Methods

Maintaining stable experimental conditions for recording from a single neuron over long periods can be a daunting task. Achieving functional isolation of real neurons and resolving dynamical instabilities are fundamental in investigating the core properties of excitability in neurons. Thus, implementing paradigms that extend the duration of single-neuron electrophysiological experiments under such conditions is crucial.

The experiment involves stimulating cells over extended periods with varying frequencies and sequences of frequencies using intracellular current injection or photo-activation protocols. A Python script is used to run simulations from a cell template noa and create stimuli, and data is transferred between HOC and Python using NMODL to add new biophysical mechanisms to NEURON. The code uses the python package in NEURON to simulate the cell soma. It creates a stimulation vector using a *numpy* array and a for loop in python, and then plays the stimulation using a chosen waveform. It also records the voltage difference across the soma of the neuron. We utilised a layer 5 pyramidal template neuron from a Blue Brain project to design *in silico* experiments. We compared two protocols: the intracellular current-injection protocol and the photo-activation protocol over with varying frequencies. The photo-activation protocol uses a light intensity of 1-10 mW/mm^2, pulse duration of 1 ms, and period length of 24 ms

+ 1 ms. The intracellular current-injection protocol uses a current amplitude of 2-3 nA, pulse duration of 1-2 ms, and period length of 25 ms.

Results

By conducting an *in silico* experiment on a realistic neuron model, we anticipated that we would detect comparable actions to those found in biological neurons. This would uncover any potential consequences that manifest as a result of the model neuron's intrinsic dynamics. However, the latency development in both cases (electrical stimulation and photo-stimulation protocols) was exhibiting very poor deterministic patterns resembling the output of the simplest deterministic conductance-based models Sec. A.